Lehigh University
Lehigh Preserve

Theses and Dissertations

2013

Novel Optical Study and Application on III-NItrides

Guan Sun
Lehigh University

Follow this and additional works at: http://preserve.lehigh.edu/etd

Part of the Electrical and Computer Engineering Commons

Recommended Citation
Sun, Guan, "Novel Optical Study and Application on III-NItrides" (2013). *Theses and Dissertations.* Paper 1641.

This Dissertation is brought to you for free and open access by Lehigh Preserve. It has been accepted for inclusion in Theses and Dissertations by an authorized administrator of Lehigh Preserve. For more information, please contact preserve@lehigh.edu.

Novel Optical Study and Application on III-Nitrides

by

Guan Sun

Presented to the Graduate and Research Committee

of Lehigh University

in Candidacy for the Degree of

Doctor of Philosophy

In

Electrical Engineering

Lehigh University

Janaury 2014

Copyright by Guan Sun

January 2014

This dissertation is approved and recommended for acceptance as adissertation in partial fulfillment of the requirements for the degree of Doctor of Philosophy in Electrical Engineering

____

Date

____

Accepted Date

Committee Members:

______________________________ ____________

Dr. Yujie J. Ding (Advisor and Chair) Date

______________________________ ____________

Dr. Filbert Bartoli Date

______________________________ ____________

Dr. Nelson Tansu Date

______________________________ ____________

Dr. Sushil Kumar Date

______________________________ ____________

Dr. Dimitrios Vavylonis Date

Acknowledgements

Pursuing Ph. D study is always my dream since I was very young, which intrigued me to come to Lehigh University, Department of Electrical and Computer Engineering. This dream would not come true without endless support and generous contributions from a number of people.

First and foremost, I would thank my advisor, Prof. Yujie J. Ding for providing me the chance to study in his group. During the past five years, he continuously supported me in all aspects as a great advisor, including instructions to conduct experiment, improving the skills of technique writing, teaching me to think as a rigorous researcher, and helping me for building up my career. Among all his supports, I want to emphasize how he generously provided freedom in distributing and utilizing my own time in the way suits me best. Besides performing as wonderful advisor, he also treats me as his good friend. I really enjoy chatting with him even the topic is beyond scope of scientific research. He is not only an advisor, but also a mentor in my whole Ph. D study.

I would like to sincerely thank Prof. Nelson Tansu, for his assistance to provide samples used in various research projects during my Ph. D study. And I also appreciate all the members of my dissertation committees, Prof. Filbert J. Bartoli, Prof. Sushil Kumar and Prof. Dimitrios Vavylonis. Without their constant encouragements and fruitful discussions, my research activity and dissertation writing cannot be carried on as smoothly.

It is not possible for me to fulfill my research without the help from my group mates, who are Dr. Guibao Xu, Dr. Suvranta K. Tripathy, Dr. Yi Jiang, Dr. Pu Zhao, Ruolin Chen and Da Li. Assistance from them makes daily research much easier and more joyful. Especially, I would really express my deepest gratitude to Dr. Guibao Xu and Dr. Suvranta K. Tripathy. Dr. Guibao Xu taught me a lot of experimental skills which are extremely crucial for my thesis project. Dr. Suvranta who worked with me for first half year in my early stage of Ph. D study, helped me build correct concept of doing research.

My Lehigh experience would not complete without interaction with other students and professionals. Many thanks to Dr. Qiaoqiang Gan, Dr. Hongping Zhao, Dr. Guangyu Liu, Yongkang Gao, Tianyi Luo, Xi Chen, Wanjun Cao etc. for their invaluable assistance. I would also express my most sincere gratitude to a special person, Yuan Wang, for sharing the light and darkness of life in Lehigh.

There is no way I can get through this acknowledgement section without very special thanks to friends: Guannan Chen, Kai Teng, Cheng Cheng and Dr. Hua Zhang. Time with them has been the happiest memory during my Ph. D study. They always accompany me when I meet failures and feel stressful. Without them, this period would be completely different.

Finally, I want to say thanks to my parents, Xuelin Sun and Xiuhua Li, for their love, encouragement, and support.

Table of Content

List of Tables ix

List of Figures x

Abstract 1

Chapter 1 Introduction 3

1.1 Introduction of III-Nitrides

1.1.1 Light emitting devices based on III-Nitrides

1.1.2 GaN based high electron mobility transistor (HEMT)

1.2 Organization of this dissertation

Chapter 2 Broadband Terahertz Generation in InGaN/GaN Heterostructures 10

2.1 Introduction

2.2 THz generation in InGaN/GaN QWs

2.2.1 THz output power and spectra

2.2.2 THz output as a function of incident & polarization angle of laser and azimuth angle of sample

2.2.3 Calculation of THz output power in InGaN/GaN QWs based on dipole radiation

2.2.4 Correlated behavior between THz and PL

2.3 THz generation in InGaN/GaN dot-in-a-wire nanostructure

2.3.1 Sample description and experimental setups

2.3.2 THz output power and spectra

2.4 Summary

Chapter 3 Potential Laser Cooling on GaN 39

3.1 Introduction

3.2 Sample description and experimental setups

3.3 Results and discussion

3.4 Summary

Chapter 4 Photoluminescence Study on III-Nitrides: InGaN/GaN QWs, GaN/AlN QWs, Freestanding GaN and BN Powder 56

4.1 Introduction

4.2 Investigation of Fast and Slow Decays in InGaN/GaN QWs

4.2.1 Sample description and experimental setups

4.2.2 PL as function of laser intensity and temperature

4.2.3 Pump-probe differential PL experiment

4.3 PL emission in deep ultraviolet region from GaN/AlN asymmetric-coupled QWs

4.3.1 Sample description and experimental setups

4.3.2 Deep ultraviolet emission from GaN/AlN asymmetric QWs

4.4 PL induced by three-photon absorption in freestanding GaN

4.5 PL induced by two-photon absorption in BN powder

4.6 Summary

Chapter 5 Transverse Nonlinear Generation in GaN/AlGaN Waveguide **85**

5.1 Introduction

5.2 Design of GaN/AlGaN waveguide

5.3 Surface emitting second harmonic generation

5.4 Summary and future outlook

Chapter 5 Summary and Future Outlook **95**

Reference **99**

Vita **123**

List of Tables

Table 2-1 Structures and THz output power of various InGaN/GaN quantum wells and control samples. 14

Table 2-2 THz output and PL information of InGaN/GaN dot-in-a-wire. P_{THz} stands for THz output power. I, λ and ΔE designate integrated intensity, peak wavelength of PL, and blue shift of the peak induced by increasing pump power, respectively. 31

Table 3-1 Bandgap and Fröhlich coupling constants of several semiconductors (see Ref. 3.27) 43

Table 4-1 Sample parameters. Here, d_{AlN}, d_{GaN}, stands for the thickness of AlN and GaN layer, respectively. E_{low}, stands for the lower-transition energy peak (or the only peak) of asymmetric-coupled (or single) QWs, while E_{high} stands for higher-transition energy peak of asymmetric-coupled QWs. I_{low}, I_{high} are relatively integration intensity of lower- and higher- transition energy peak, respectively. Label R stands for the ratio between the PL intensities of the higher- and lower-energy transition peaks. 69

Table 5-1 Structures and THz output power of various InGaN/GaN quantum wells and control samples. 86

List of Figures

Figure 1.1 The bandgap of the group III-nitride alloys as a function of the a-axis lattice constant, compared to the visible colors, solar spectrum, and 1.55 m wavelength. Figure from Ref. [1]. 3

Figure 1.2 Current and expected market of LEDs. Data from Yole developpement and IC Insights. 5

Figure 1.3 Advantages of GaN based high electron mobility transistor (HEMT). Figure from Ref. [1.8]. 6

Figure 2.1 Bandgap diagram of InGaN/GaN QWs and a schematic shows how THz is generated by ultrafast laser. 11

Figure 2.2 (a) A schematic of InGaN quantum wells. (b) Experimental setups. WP, PM stands for wave plate and parabolic mirror, respectively. 12

Figure 2.3 A typical spectrum of THz wave of 8-period $In_{0.25}Ga_{0.75}N$/GaN QWs measured by homemade gratings at room temperature. 15

Figure 2.4 (a) THz output power generated by $In_{0.25}Ga_{0.75}N$/GaN multiple QWs was measured as a function of incident angle defined as the angle of surface normal being formed with the pump beam. Dots correspond to data points. Red curve corresponds to fitting by using $P_{THz} = f(\theta)\sin^2(\theta)$. (b) Polarization dependences of THz output power generated by $In_{0.25}Ga_{0.75}N$/GaN multiple QWs and THz polarization angle. Polarization angle of pump beam is defined as the angle between the pump polarization and the incident plane. Polarization angle of THz wave, defined as the angle between the THz polarization and the incident plane, was determined by wire-grid polarizer. Squares designate average output power as function of pump polarization. Dots correspond to polarization angle of THz beam measured versus pump polarization. Solid curve is a theoretical result after taking into consideration Fresnel reflection. 16

Figure 2.5 Dependences of THz output power and THz polarization on azimuth angle for $In_{0.25}Ga_{0.75}N$/GaN QWs. Squares correspond to average output powers whereas dots represent polarization angles of THz beam. 18

Figure 2.6 (a) THz output power and PL intensity at 10 different positions of 8-period $In_{0.25}Ga_{0.75}N$/GaN QWs. (b) PL intensity of conventional and staggered InGaN/GaN QWs. 22

Figure 2.7 (a) PL spectra of InGaN quantum wells with different periods measured at room temperature. (b) PL intensity and THz output power versus well period. Red triangular corresponds to PL intensity and blue cross corresponds to THz output power. The pump fluence is set as 85 μJ/cm^2. 23

Figure 2.8 (a) THz output power as a function of pump fluence. The crosses correspond to experiment data. The red curve corresponds to a quadratic fitting for first ten data points. (b) Integrated PL intensity and peak energy as a function of pump fluence. The red triangles and blue dots correspond to PL intensity and peak energy, respectively. 25

Figure 2.9 (a) THz spectra measured at pump fluencies 11, 22, 43, 91 μJ/cm^2. (b) THz energy density generated per well as function of pump fluence. 27

Figure 2.10 (a) A low magnification bright field scanning transmission electron microscopy image showing the position and vertical alignment of the ten InGaN dots in a GaN nanowire. (b) A 45° tilted scanning electron microscopy image showing the morphology of the InGaN/GaN dot-in-a-wire heterostructures grown on a Si (111) substrate. 31

Figure 2.11 (a) Typical THz spectrum emitted by InGaN/GaN dot-in-a-wire. (b) THz pump power vs. pump power or fluence. Cross corresponds to experiment result and curve is quadratic fitting. 32

Figure 2.12 (a) Typical PL spectrum of doped and intrinsic InGaN/GaN dot-in-a-wire nanostructure. (b) Energy of PL peak vs. pump power of doped and intrinsic InGaN/GaN dot-in-a-wire nanostructure. 36

Figure 2.13 (a) Illustration InGaN/GaN dot-in-a-wire LED. (b) The optical microscopy image of the fabricated dot-in-a-wire LED. (c) Picture of LED under forward bias. (d) THz output power vs. bias applied to dot-in-a-wire LED. 37

Figure 3.1 (a) Peter Pringsheim. (b) A scheme of anti-Stoke photoluminescence. (Figure reproduced from Ref. [3.4]). 40

Figure 3.2 PL spectra excited by 209 nm with an average power of 0.5 mW at different temperatures. (b) Absorption spectrum at 300K. Squares are experiment data and curve is exponential decay fitting. 47

Figure 3.3 (a) Normalized PL spectra measured at 300 K. The blue and red curves are excited by 209 nm and 385.6 nm respectively. (b) Normalized PL spectra measured at 390 K. The blue and red curves are excited by 209 nm and 392 nm respectively. 48

Figure 3.4 (a) Integrated PL intensity as a function of laser power measured at 300 K: (a) excited by 385. 6 nm. (b) excited by 532 nm. The solid red and green lines are linear and quadratic fitting respectively. 51

Figure 3.5 (a) Integrated PL intensity as a function of pump wavelength measured at 300 K. The laser power is set as 20 mW, the solid line is guide for the eye. (b) Integrated PL intensity as a function of laser power for four wavelengths measured at 300 K. The experiment data have been fitting by $I \propto P^{\alpha}$, where I is integrated PL intensity, P is laser power and α is power index. 53

Figure 3.6 (a) Normalized integrated PL intensity as a function of temperature for different laser wavelengths. The solid lines are guide for eye. The dashed line is a fitting curve assuming that intensity of ASPL is proportional to number of LO phonons which is defined by Bose-Einstein statistics. 54

Figure 4.1 An experimental setup for pump-probe differential PL. 59

Figure 4.2 Excitation power density dependent PL spectra for InGaN QWs measured at 5 K. 60

Figure 4.3 (a) The emission energy of P_L vs excitation power density measure at 5 K. (b) The emission energy of P_L vs carrier density for excitation power density higher than 16.7 W/cm^2. The solid curve is a fit based on band gap renormalization effect. 60

Figure 4.4 The emission energy of P_L vs temperature measured at 16.7 W/cm^2. The solid curve is a fit based on band tail model. 62

Figure 4.5 Normalized integrated PL intensity as s function of $1/T$ for InGaN QWs measured at 16.7 W/cm^2. The red and blue curves are single and two

channels Arrhenius fits respectively. E_a and E_b stand for the activation energy. 62

Figure 4.6 (a) Pump-probe differential PL spectra at different delay times measured at 5 K. (b) Differential ratio vs. delay time measured at different temperatures. The solid curves are single exponential fits to experiment data. 65

Figure 4.7 The experiment setup for third harmonic output from Ti: sapphire oscillator. 68

Figure 4.8 PL spectra measured at 4.2 K on different samples at pump power of 6 mW at 235 nm. The signals of sample #3 and #4 are both multiplied by a factor of 20 for clarity. 69

Figure 4.9 Typical calculated band diagram of sample #1 using NEXTNANO3 8-band-k•p Schrödinger-Poisson solver. 70

Figure 4.10 (a) PL intensities vs. temperature. The dots correspond data of P_{high} and the square correspond that of P_{low}. (b) Ratio of PL intensities determined from Fig. 4.8 vs. temperature; and (c) Transition energies of two PL peaks vs. temperature. 74

Figure 4.11 Anti-Stokes and Stokes PL spectra measured at 4.2 K and under excitation wavelength of 782 nm and 209 nm. 75

Figure 4.12 (a) Anti-Stokes PL spectra at different temperature. (b) Photon energies of each peak at different temperature. 76

Figure 4.13 Anti-Stokes PL spectra at different pump power measure at 4.2 K 77

Figure 4.14 (a) Intensity of DAP peak plotted vs. pump power in log scale at 4.2 K. Straight line corresponds to linear fit to data, resulting in a slope of 3.03. (b) Intensity of I_2 peak plotted vs. pump power in log scale at 4.2 K. Straight line corresponds to linear fit to data, resulting in a slope of 2.75. 79

Figure 4.15 PL spectra measured at room temperature. The pump power for 206.88 and 412.51 nm is 26 mW and 250 mW respectively. 81

Figure 4.16 (a) PL intensity as a function of excitation photon energy. The blue line is guide for eye. (b) PL intensity as a function of pump power. The cross corresponds to experiment data. The red curve is quadratic fit for first 12 points. 83

Figure 5.1 (a) Scheme of GaN/AlGaN waveguide. QPM stands for quasi-phase match and DBR stands for distributed Bragg reflector. (b) Scheme of momentum conservation. 88

Figure 5.2 Ordinary refractive index problems along z direction. The wavelength is chosen as 820 nm and polarization is along x direction. 88

Figure 5.3 (a) Reflection of top and bottom DBR. (b) Electric field amplitude profile of first TE mode. (c) Electric field amplitude profile of first TM mode. 89

Figure 5.4 Effective index of TE and TM mode in GaN/AlGaN waveguide from 800-840 nm. 90

Figure 5.5 Wavelength of generated photon pairs as function of pump laser angle. The angle is defined in Fig. 5.1 (a). 91

Abstract

GaN and its heterostuctures have been intensively studied for wide applications. For example, InGaN/GaN quantum wells (QWs) have been used as active materials for light emitting diodes (LEDs) and laser diodes (LDs) from blue to green region while GaN/AlGaN QWs have been used for ultraviolet region. Meanwhile, nitrides are also very important materials for power electronic devices since such materials hold various advantage over competing semiconductor materials such as Si, GaAs, etc. Due to the above reasons, we believe GaN and its heterostructures will play crucial role for optics and electronics devices as silicon does for electronics. Thus, it is worthwhile to explore possibility of achieving different kinds of newapplications on GaN.

This dissertation is focused on optical study on GaN based materials, including GaN thin film, InGaN/GaN QWs, InGaN dot-in-a-wire nanostructures, GaN/AlN QWs, etc. More specifically, in Chapter 2, we report efficient broadband terahertz (THz) generated in InGaN/GaN heterostructures due to spontaneous dipole radiation utilizing the strong internal field. Considering the normalized power, InGaN/GaN heterostructure is one of the most efficient materials for broadband THz generation. The correlated behavior between THz and photoluminescence (PL) has also been discussed. In Chapter 3, we present the study of PL upconversion from a free standing GaN and the mechanism has been attributed to phonon-assisted anti-Stokes photoluminescence (ASPL) if photon energy of pump laser is in the tail of absorption edge. The potential of laser cooling based on such phenomena has been explored. In Chapter 4, we have present detailed PL studies

on different kind of nitrides materials including InGaN/GaN QWs, GaN/AlN QWs, GaN thin film and BN powders. In Chapter 5, we explore the possibility of nonlinear generation on GaN. A GaN/AlGaN multilayer waveguide has been designed to achieve transverse parametric conversion.

The objective of this dissertation is not only to study the mechanism of optical behavior of GaN based materials, but also to explore the potential application based on these experimental results.

Chapter 1. Introduction

1. 1. Introduction of III-Nitrides

III-Nitrides especially GaN, InN, AlN and their alloys have attracted a lot of attention for at least past 20 years mainly due to various applications. In this section, we give a brief introduction about III-Nitride materials and their applications from light emitting devices to power electronics and etc.

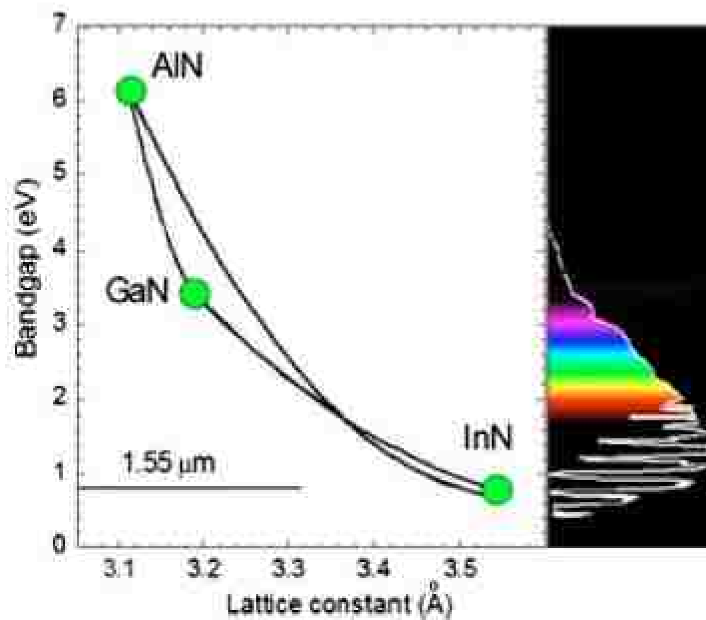

Fig. 1.1. The bandgap of the group III-nitride alloys as a function of the a-axis lattice constant, compared to the visible colors, solar spectrum, and 1.55 m wavelength. Figure from Ref. [1].

1. 1. 1. Light emitting devices based on III-Nitrides

As is shown in Fig.1.1, the bandgap of GaN, InN, AlN and their alloy ranges from 0.64 eV to 6.2 eV, which covers the whole spectrum of the sunlight. Such property ensures that III-Nitrides will have a lot of application in light emitting devices. Indeed, since Shuji Nakamura and co-workers from Nichia demonstrated the first visible blue and green InGaN double-heterostructure LED [1.2-1.4] from 1993 to 1995, and first pulsed and continuous wave (cw) InGaN/GaN current injection blue laser diodes (LDs) operating at room temperature [1.5] in 1996, researchers have intensively worked on III-Nitrides devices in order to enhance conversion efficiency and enrich the spectrum. So far, LEDs based on III-Nitrides of which the emitting wavelength ranges from 210 nm to 550 nm has been demonstrated. Due to its much higher efficiency, better color display, environmental friendliness compared to traditional incandescent and fluorescent lamps, the market of LEDs based on III-Nitrides has extremely expanded, see Fig. 1.2. It has been pointed out that if widely used, LEDs based on III-Nitrides can lead to a decrease of worldwide electricity consumption due to lighting by more than 50%. Thus it can be expected that the market of LEDs will continue to grow significantly in the next several years. Besides its demonstration from ultraviolet to green region, it is also worthwhile to mention that III-Nitrides have potential applications in infrared region owing to very low bandgap InN.

Although light emitting devices based on III-Nitrides have been well developed, some technique issues yet remain to overcome. Unlike heterostructures based on AlGaAs,

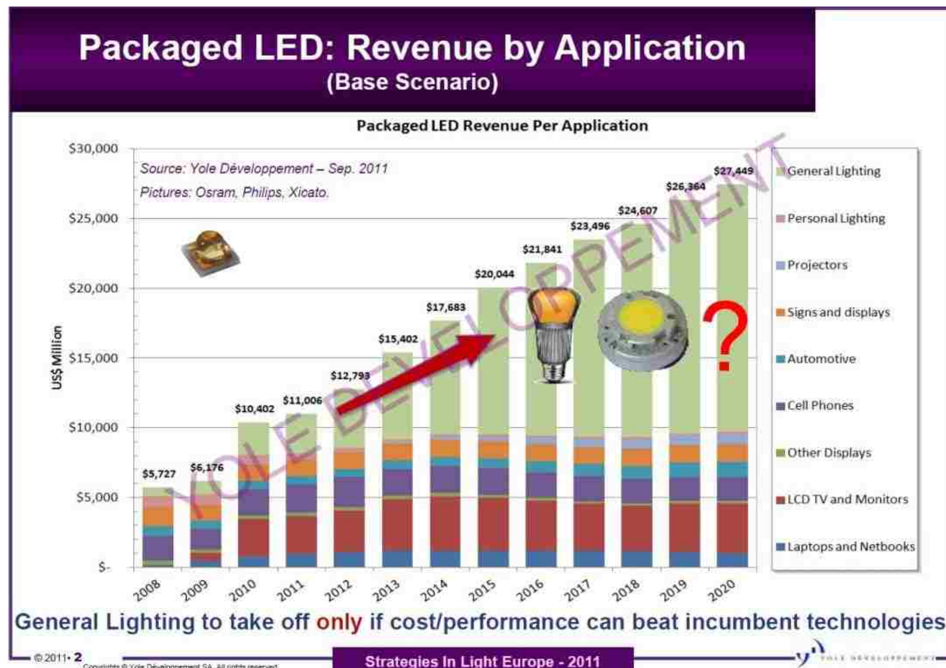

Fig. 1.2. Current and expected market of LEDs. Data from Yole developpement and IC Insights.

wurtzite III-Nitride [0001]-oriented materials exhibit non-zero spontaneous polarization due to the asymmetric semiconductor crystal structure. Because of the lack of lattice-matched substrate for nitride materials, the utilization of foreign substrate causes the lattice-mismatch between the substrate and the III-Nitride material, which induces the piezoelectric polarization in the III-Nitride materials. The total internal field inside InGaN/GaN and GaN/AlGaN heterosturctures is up to several MV/cm [1.6, 1.7].

Such large internal field causes large charge separation in InGaN QWs, which significantly reduces the spontaneous emission radiative recombination rate for LEDs application and reduces the optical gain for laser application. Obviously, for these two

applications the internal field plays a negative role which drives some researchers to utilize novel structures of quantum well to reduce the effect of carrier separation.

However, as a coin always has two sides, such large electric field will benefit some specific applications. In next chapter, we will show how we can utilize such field to generate terahertz.

1. 1. 2. GaN based high electron mobility transistor (HEMT)

Need	Enabling Feature	Performance Advantage
High Power/Unit Width	Wide Bandgap, High Field	Compact, Ease of Matching
High Voltage Operation	High Breakdown Field	Eliminate/Reduce Step Down
High Linearity High Frequency	HEMT Topology High Electron Velocity	Optimum Band Allocation Bandwidth
High Efficiency	High Operating Voltage	Power Saving, Reduced Cooling
Low Noise High Temperature Operation	High Gain, High Velocity Wide Bandgap	High Dynamic Range Receivers Rugged, Reliable, Reduced Cooling
Thermal Management	SiC Substrate	High Power Devices

Fig. 1.3. Advantages of GaN based high electron mobility transistor (HEMT). Figure from Ref. [1.8].

As the market for cellular, personal communications services, and broad-band access are expanding, radio frequency (RF) and microwave power amplifiers are beginning to be the focus of attention. A variety of power amplifier technologies are vying for market share, such as Si lateral-diffused metal–oxide–semiconductors and

bipolar transistors, GaAs metal–semiconductor field-effect transistors (MESFETs), GaAs (or GaAs/InGaP) heterojunction bipolar transistors, SiC MESFETs, and GaN high-electron mobility transistors (HEMTs). Among all these devices, GaN based HETMs holds many advantages according to Ref. [1.8], see Fig. 1.3. The first column of Fig. 1.3 states the required performance benchmarks for any technology for power devices and the second column lists the enabling feature of GaN-based devices that fulfill this need. The last column summarizes the resulting performance advantages at the system level and to the customer. For example, the high power per unit width translates into smaller devices that are not only easier to fabricate, but also offer much higher impedance. This makes it much easier to match them to the system, which is often a difficult task with conventional devices in GaAs. The high-voltage feature eliminates or at least reduces the need for voltage conversion. GaN devices can be operated at high voltage (up to 42 V). The higher voltage operation results in high efficiency and reduces power requirement, and this advantage will also simplify cooling, an important advantage, since cost and weight of cooling system is a significant fraction of the cost of a high power microwave transmitter.

In simulation saturation velocity of electron inside GaN can be up to 3×10^7 cm/s. However, experimentally, the value rarely surpasses 1.5×10^7 cm/s. Some researchers pointed out due to stronger Fröhlich interaction, longitude phonon (LO) emission time in GaN is ten times shorter than that of GaAs while the LO decay time is similar [1.9]. Thus the LO phonon can be accumulated in GaN. Such phenomena have been observed by our group [1.10]. However, the strong Fröhlich interaction could be a benefit for some

conditions. In Chapter 3, we will show it could enhance the anti-Stokes photoluminescence.

1. 2. Organization of this dissertation

In this dissertation, I selectively summarize my research on optical study and novel applications on III-Nitride materials.

In Chapter 2, efficient broadband terahertz (THz) has been generated in InGaN/GaN heterostructures due to spontaneous dipole radiation utilizing the strong internal field. Considering the normalized power, InGaN/GaN QWs is one of the most efficient materials for broadband THz generation. Especially, we have generated THz in InGaN/GaN dot-in-a-wire nanostructures. The THz output has been further increased by external field. The correlated behavior between THz and photoluminescence (PL) has also been discussed.

In Chapter 3, we have studied PL upconversion from a free standing GaN and the mechanism has been attributed to phonon-assisted anti-Stokes photoluminescence (ASPL) if photon energy of pump laser is in the tail of absorption edge. The potential of laser cooling base on such phenomena has been explored.

In Chapter 4, we have present detailed PL studies on different kind of nitrides materials including InGaN/GaN QWs, GaN/AlN QWs, GaN thin film and BN powders. For InGaN/GaN QWs, we have investigated the slow and fast decay by pump probe differential photoluminescence study. For GaN/AlN QWs, we have designed asymmetric QWs to enhance deep ultraviolet emission. In GaN thin film and BN powder, we have observed photoluminescence induced by multiphoton absorption.

In Chapter 5, we explore the possibility of nonlinear generation on GaN. A GaN/AlGaN multilayer waveguide has been designed to achieve transverse parametric conversion.

Chapter 2. Broadband Terahertz Generation in InGaN/GaN Heterostructures

2. 1. Introduction

Terahertz (THz) generation and detection have been intensively studied for past two decades for realizing promising applications of THz waves in medicine, biology and security [2.1, 2.2]. A THz wave has its frequencies typically defined in the range from 300 GHz to 3 THz, corresponding to the wavelength range from 1 mm to 100 μm. In general, THz source can be divided into two categories: narrow band and broad band THz [2.2]. Recently, both these two kinds THz source has been tried to generate on GaN based materials due to potential various benefits [2.3-2.12]. InGaN/GaN heterostructures in terms of quantum wells (QWs) has been intensively studied in past twenty years for their wide application in optoelectronics devices including light emitting diodes (LEDs) and laser diodes (LDs). One unique property for such heterostructures is, if grow along (0001) direction, an internal field up to several MV/cm is present inside in InGaN well [2.13]. Such large electric field will induce quantum confined Stark effect (QCSE), which will reduce the recombination efficiency due to separation of electron and hole wave functions [2.14-2.16], see Fig. 2.1. Obviously, for applications of laser diodes or light emitting diodes, such electric field is obstacle to achieve high efficiency or low threshold devices, which drives researchers to reduce the charge-separation effect by employing

novel QWs structure [2.17], [2.18]. Such built-in electric field in InGaN QWs can be a special advantage to achieve certain function without applying an external field. Here, in this chapter, we will show how we can utilize internal electric field inside $In_xGa_{1-x}N$/GaN heterostrctures to generate broadband THz. When the electrons are excited to conduction band, due to the separation behavior induced internal field, dipoles are generated. By using a femtosecond laser as pump source, dipole strength will change femtosecond range, resulting in efficient dipole radiation in THz range. The chapter will be organized as following: in section 2.2, we investigate the THz generation in different InGaN QWs. The THz output power, spectra, has been measured. By studying the THz output as function of pump power, polarization, azimuth and incident angle, number of QWs, and indium composition of inside QWs, the generation mechanism has been determined. In section 2.3, we investigate the THz generation from InGan/GaN dot-in-a-wire nanostructures. Although the generation mechanism is similar to that of InGaN QWs, the unique benefit of such structure has been discussed.

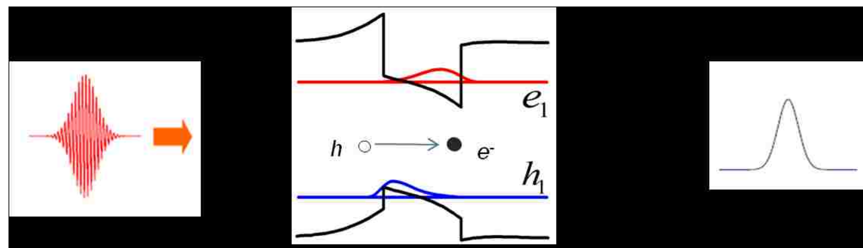

Fig. 2.1. Bandgap diagram of InGaN/GaN QWs and a schematic shows how THz is generated by ultrafast laser.

2. 2. THz generation in InGaN/GaN QWs

2. 2. 1. Sample description and experimental setups

All samples studied in section are from Dr. Nelson Tansu's group [2.19]. The growth of InGaN/GaN QWs structures was carried out on a 2.8-μm-thick unintentionally-doped GaN (background electron density of ~ 4×10^{16} cm^{-3}) template on a *c*-plane sapphire substrate by metal-organic chemical vapor deposition (MOCVD), see Fig. 2.2(a). The growth of GaN template was performed at 1080 ℃ by employing 35-nm thick low-

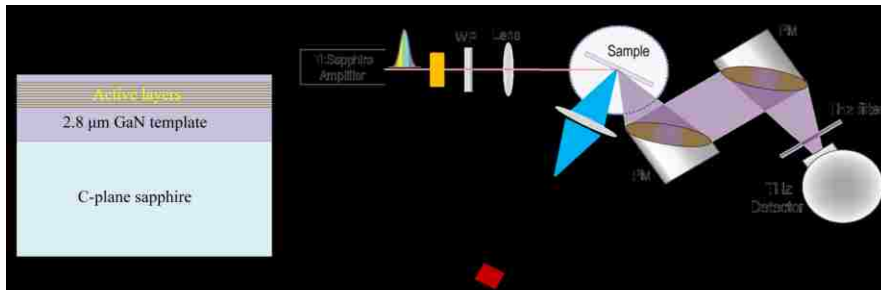

Fig. 2.2. (a) A schematic of InGaN quantum wells. (b) Experimental setups. WP, PM stands for wave plate and parabolic mirror, respectively.

temperature-grown (T_g = 525 ℃) GaN buffer layer. Subsequently, several periods of InGaN/GaN QWs were deposited on the GaN template by MOCVD at 700 ℃. Exact structures of InGaN QWs in addition to some control samples we studied in this project can be found in Table 2-1.

Broadband THz pulses were generated by a coherent radiation beam at the wavelength of 391 nm after frequency-doubling the output beam from a Ti:sapphire regenerative amplifier by a BBO crystal, see Fig. 2.2(b) for experiment setups. The

photon energy of such beam is higher than bandgap of InGaN well layer but lower than GaN barrier. The pulse duration is measured around 200 fs and repetition rate is 250 kHz. The excitation beam was then focused on top surface of InGaN/GaN QWs with the laser spot area between 2-3 mm^2. The polarization of laser was tuned as parallel polarized by a half wave plate and incident angle was set as 70° to reduce the reflection. The THz radiation was collimated, and then, focused onto a 4.2-K Si bolometer or pyroelectric detector by a pair of gold-coated parabolic mirrors in reflection geometries. Meanwhile the photoluminescence (PL) signal of InGaN QWs was excited simultaneously via same beam and then collected through a single channel high resolution spectrometer connected with a photomultiplier (PMT).

2. 2. 2. THz output power and spectra

In Table 2-1, we outline the THz output power from different samples for an average pump power of 400 mW at 391 nm. Comparing the THz output power of all InGaN QWs samples (Sample 1 to 9) with that of GaN thin film (Sample 10) or sapphire substrate (Sample 11), we can know the THz is only generated inside InGaN well. The highest THz output power is up to 0.956 μW, generated by an eight-period $In_{0.25}Ga_{0.75}N$/GaN QWs. Considering the total effective thickness of this sample is only 24 nm, we believe InGaN/GaN QWs is one of the most efficient materials for THz generation. If we normalize the THz output powers by the square of the pump power and thickness or InGaN wells, the normalized value is 10.4 $nW/(nm^2 \cdot W^2)$. We compared the

results from such InGaN QWs with InN thin film which has been considered as one of the most efficient materials for THz emission [2.20, 2.21]. Under a similar experimental setup, the highest average output power of InN was measured to be about 2.4 μW with a thickness of 220 nm and a pump power of 1.5 W [2.21]. The normalized value for such InN is only 0.022 nW/ ($nm^2 \cdot W^2$). Thus the generation efficiency in $In_{0.25}Ga_{0.75}N$/GaN QWs is nearly 500 hundred times than InN thin film which proves that InGaN/GaN QWs are one of the most efficient materials for broadband THz generation. We can also compare with the result of 180-nm $In_{0.36}Ga_{0.64}N$ (Sample 12). The normalized THZ value

Table 2-1. Structures and THz output power of various InGaN/GaN quantum wells and control samples.

Sample	Structures	THz Power (nW)
1	8-period $In_{0.25}Ga_{0.75}N$/GaN: 3/12 nm	956
2	1-period $In_{0.19}Ga_{0.81}N$/GaN: 3/10 nm	5.95
3	2-period $In_{0.19}Ga_{0.81}N$/GaN: 3/10 nm	11.6
4	4-period $In_{0.19}Ga_{0.81}N$/GaN: 3/10 nm	34.5
5	6-period $In_{0.19}Ga_{0.81}N$/GaN: 3/10 nm	62.5
6	8-period $In_{0.19}Ga_{0.81}N$/GaN: 3/10 nm	98.2
7	16-period $In_{0.19}Ga_{0.81}N$/GaN: 3/10 nm	297.6
8	4-period $In_{0.22}Ga_{0.78}N$/GaN: 4.5/15 nm	127
9	$In_{0.2}Ga_{0.8}N/In_{0.25}Ga_{0.75}N/In_{0.2}Ga_{0.8}N$/GaN: 1.8/0.9/1.8/15 nm, 4-period	98
10	350- μm GaN	1.6
11	500- μm sapphire	0.23
12	180-nm $In_{0.36}Ga_{0.64}N$ thin film	112

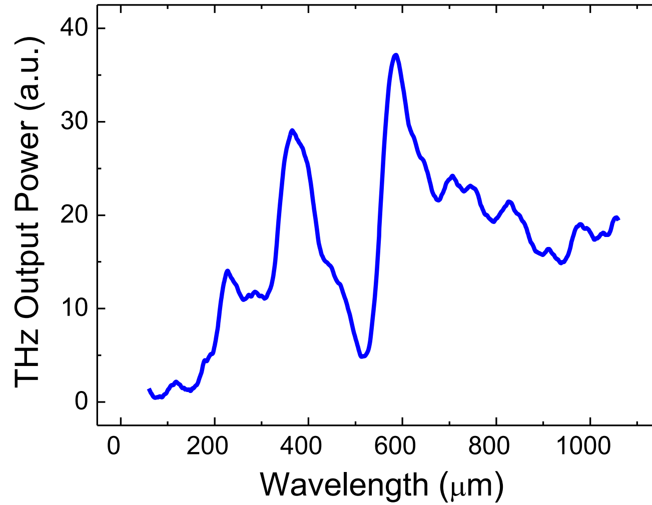

Fig. 2.3. A typical spectrum of THz wave of 8-period $In_{0.25}Ga_{0.75}N$/GaN QWs measured by homemade gratings at room temperature.

is also only 0.022 nW/ ($nm^2 \cdot W^2$). Such comparisons among the output powers generated from three samples reveal that the mechanism for the THz generation from the InGaN/GaN QWs must be fundamentally different from that for the InN and InGaN thin-film samples. Through more details analysis and discussion of mechanism in the following section, we will show the THz is generated by instantaneous dipole radiation induced by internal field.

We have measured the spectrum of the THz output beam generated by the $In_{0.25}Ga_{0.75}N$/GaN QWs by directly studying the diffraction of the THz beam by a set of the rotating gratings. Based on Fig. 1, we can see that the frequencies of the THz output roughly span the frequency range from 300 GHz to 1.5 THz. The huge dip located at 520 μm (577 GHz) is caused by water vapor absorption.

2. 2. 2. THz output as a function of incident & polarization angle of laser and azimuth angle of sample

In order to understand the mechanism for the THz generation in our InGaN/GaN QWs, we first measured the output power of the THz beam propagating in the transmission direction as a function of the incident angle for the pump beam, as shown in Fig. 2.4(a). According to Fig. 2.4(a), when the incident angle for the pump beam was zero, the THz output power was close to zero. The highest THz output power occurred at an incident angle of 72°, which is close to the Brewster angle for the pump beam. After

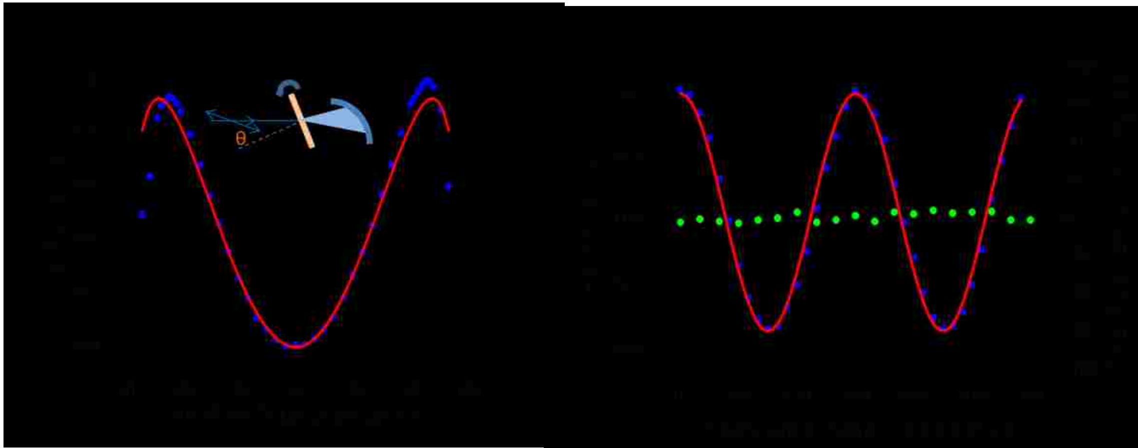

Fig. 2.4. (a) THz output power generated by $In_{0.25}Ga_{0.75}N/GaN$ multiple QWs was measured as a function of incident angle defined as the angle of surface normal being formed with the pump beam. Dots correspond to data points. Red curve corresponds to fitting by using $P_{THz} = f(\theta)\sin^2(\theta)$. (b) Polarization dependences of THz output power generated by $In_{0.25}Ga_{0.75}N/GaN$ multiple QWs and THz polarization angle. Polarization angle of pump beam is defined as the angle between the pump polarization and the incident plane. Polarization angle of THz wave, defined as the angle between the THz polarization and the incident plane, was determined by wire-grid polarizer. Squares designate average output power as function of pump polarization. Dots correspond to polarization angle of THz beam measured versus pump polarization. Solid curve is a theoretical result after taking into consideration Fresnel reflection.

taking into consideration the Fresnel reflection for the pump beam, the THz output power (P_{THz}) can be approximated by $P_{THz} = f(\theta)sin^2(\theta)$, where $f(\theta)$ describes the contribution originating from the Fresnel reflection of the pump beam and $sin^2(\theta)$ represents a typical angle distribution of the dipole radiation. The experimental data can be well fitted by using above equation, which is illustrated by Fig. 2.4(a). Thus, we can conclude that the angular distribution of the THz radiation is consistent with that of the THz generation due to the dipole radiation.

Besides the angular distribution of the THz radiation, we also measured the dependences of the THz output power and polarization on the polarization of the pump beam and azimuth angle. Fig. 2.4(b) illustrates our result following the measurement of the THz output power as a function of the pump polarization angle in the reflection geometry. In such a case, we set the incident angle to be around 72 °in order to collect the maximum amount of the THz output power. One can see from Fig. 2.4(b) that the THz output power periodically oscillates as a function of the pump polarization angle. After taking into consideration the Fresnel reflection of the pump beam, our data can be well fitted by our theoretical curve, as shown by Fig. 2.4(b). This implies that the oscillation of the THz output power as a function of the pump polarization angle is primarily caused by the dependence of the Fresnel refraction on the polarization angle of the pump beam. Therefore, the dependence of the THz output power on the pump polarization angle is consistent with that of the THz generation due to the dipole radiation. Furthermore, one can see from Fig. 2.4(b) that the THz polarization angle is always around zero, i.e. the THz output beam was *p*-polarized with its polarization lying in the incidence plane. This

is again consistent with our claim that the mechanism of THz generation is the dipole radiation.

We measured the dependences of the THz output power and polarization angle on the azimuth angle from the $In_{0.25}Ga_{0.75}N$/GaN QWs in the reflection geometry. During these measurements, we set the incident and polarization angles of the pump beam to 35° and 0°, respectively. According to Fig. 2.5, we can see that both the THz output power and the polarization angle do not change when increasing the azimuth angle. Such results

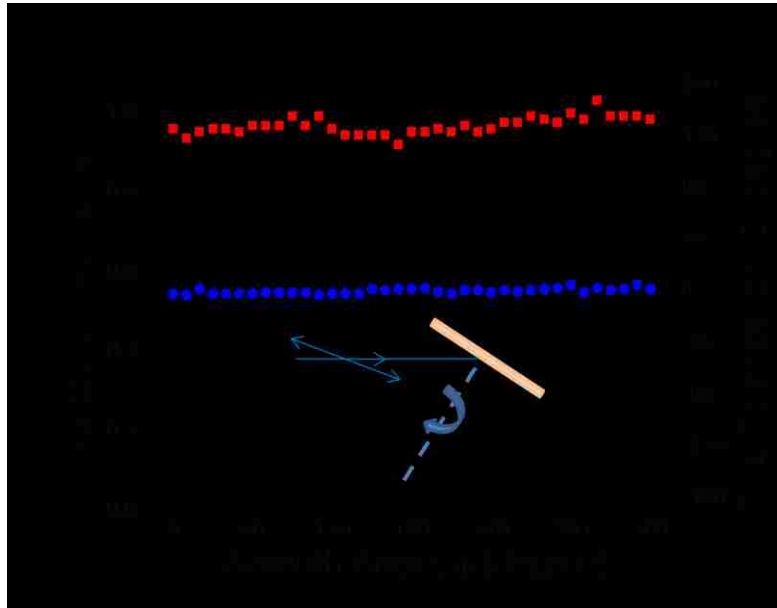

Fig. 2.5. Dependences of THz output power and THz polarization on azimuth angle for $In_{0.25}Ga_{0.75}N$/GaN QWs. Squares correspond to average output powers whereas dots represent polarization angles of THz beam.

are also consistent with the THz generation due to the dipole radiation. Indeed, different azimuth angles would not affect the densities of the photogenerated electrons and holes, and therefore, they would not affect the THz output power and polarization.

In conclusion of this part, the THz output as a function of incident and polarization angle of pump laser, and azimuth angle of sample supports dipole radiation as a generation mechanism.

2. 2. 3. Calculation of THz output power in InGaN/GaN QWs based on dipole radiation

In this subsection, we will derive an equitation based on dipole radiation to calculate absolute THz output power emitting from InGaN QWs.

According to the theory of dipole radiation, the time-dependent THz power radiated in all direction can be evaluated by:

$$P(t) = \frac{1}{6\pi\varepsilon_0 \varepsilon c^3}\left(\frac{d^2 D(t)}{dt^2}\right)^2 \tag{2-1}$$

where $\varepsilon_0\varepsilon$ is the static permittivity of the medium, c is the light velocity, and $D(t)$ is time Assuming the laser peak power is $I(t)$, we can get:

$$\frac{dD(t)}{dt} = I(t)[1-\exp(-\alpha L)]d \tag{2-2}$$

where the α is absorption coefficient, and L is the total thickness of QWs. d represents the distance between the electrons and holes. In our calculation, d is set as the initial displacement between the weighted maxima of the electron and hole wave functions. For

a 3-nm InGaN QWs the initial separation of the electron and hole wave function can be larger than 1 nm [2.22]. Assuming that the laser has a Lorentzian shape in time scale, *I(t)* can be expressed as:

$$I(t) = I_0 \frac{1}{1+\left(\frac{4t^2}{\tau^2}\right)} \qquad (2\text{-}3)$$

where τ is pulse width. I_0 can be calculated by:

$$J = \int I(t) \qquad (2\text{-}4)$$

where J is single pulse energy, which is equal to average power divided by laser repetition frequency. After solving I_0, we can substitute equation (2-2) and (2-3) into equation (2-1). Finally through equation (2-1), we can get the average THz output power is:

$$P = \frac{1}{3\varepsilon_0 \varepsilon F (c\tau)^3} \left\{ \frac{ed\left[1-\exp(-\alpha L)\right]I}{\pi h\nu} \right\}^2 \qquad (2\text{-}5)$$

where d is average separation of electron and hole wave functions, F is the repetition frequency, I is average pump power. Substitute into the all experiment value in our setup, the average THz output for our experiment setup is about 60 μW. Such power is much higher than we measured form experiment, i.e. 1 μW. Such a discrepancy is attributed to the partial collection of the THz beam by the parabolic mirrors and other loses. From equation (2-5), we can also know how to increase the THz output power. For example,

the pulse width of our laser is around 200 fs. If we reduce it to 100 fs which is typical used for broadband THz generation. In such case, the THz output power will be increased 8 times, which is 480 μW. We can also increase the number of QWs to absorb the total pump power, for our 8-period $In_{0.25}Ga_{0.75}/GaN$ QWs only half of pump laser is absorbed. So we can increase the THz output power for another 4 times which is up to 2 mW. From the same equation, we know the THz output power is also proportional to square of separation of electron and hole wave functions, i.e. d. The separation can be increased by increasing the indium composition in InGaN alloy. If we take a look at the THz output power of sample 1 and sample 6, by increasing the 6% indium, the THz output power has been increased for 10 times.

2. 2. 4. Correlated behavior between THz and PL

To further understand the behavior of THz generation, we also simultaneously measure the PL signal during the experiment. For sample 1, when we move the laser spot in the different position, the signal intensity of THz and PL will both change. The interesting part is THz output power and PL intensity has opposite behavior. As is shown in Fig. 2.6(a), the spot which has low PL intensity which always has high THz output power and vice versa. We claim such phenomenon is consistent with our THz generation mechanism.

When a transverse electric field is added on QWs, the electrons and holes are pulled up to opposite direction. Thus, the overlap of electron and hole wave functions will

reduce. As a result the recombination rate also decreases, i.e. PL intensity. Meanwhile, the peak wavelength of emission spectrum is red shifted. Such effect is named as quantum confined Stark effect (QCSE) [2.23]. Basically, PL intensity will reduce if transverse electric field is increased. However for THz generation, as we analyzed in last section, the output power should increase with the separation of electron and hole wave functions. Because sample 1 is not uniform, the indium composition may be modulated in different positions which results in different electric field. Thus the THz and PL intensity is also modulated but in opposite direction.

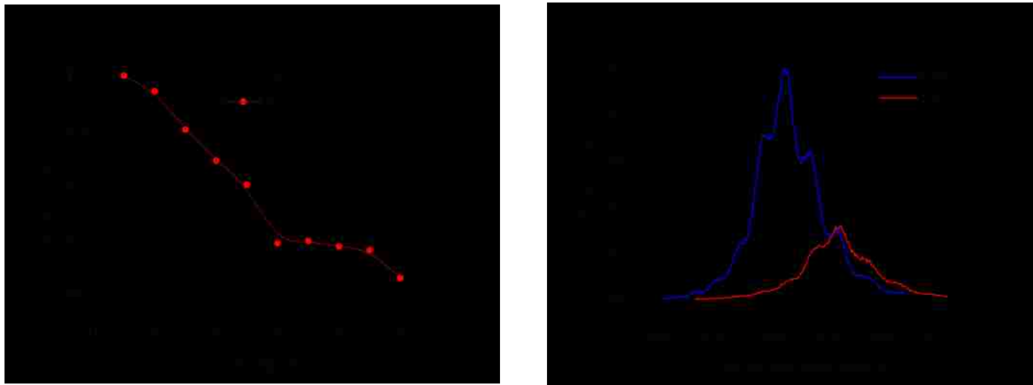

Fig. 2.6. (a) THz output power and PL intensity at 10 different position of 8-period $In_{0.25}Ga_{0.75}N$/GaN QWs. (b) PL intensity of conventional and staggered InGaN/GaN QWs.

To further confirm such tendency, we design a pair of InGaN QWs named as staggered (sample 9) and conventional QWs (sample 8) of which the structures are also listed in Table 2-1. As we just explained, a transverse field will reduce overlap of electron and hole wave functions due to QCSE, resulting in poor radiation efficiency.

Thus, in most cases, the internal field will be obstacle to fabricate a device with high efficiency and low threshold. Thus, our collaborator has designed so called staggered QWs which will enhance the PL intensity by increasing the overlap of electron and hole wave functions [2.17, 2.18]. Indeed, we do observe the PL signal is enhance in staggered QWs, see Fig. 2.6(b). While for THz, through above analysis, we know it should reduce with if you increase overlap of electron and hole wavefucntions. In experiment, the THz output power does reduce about 30% in staggered QWs compared to conventional sample.

We also designed a set of InGaN/GaN QWs with different wellnumbers to see how

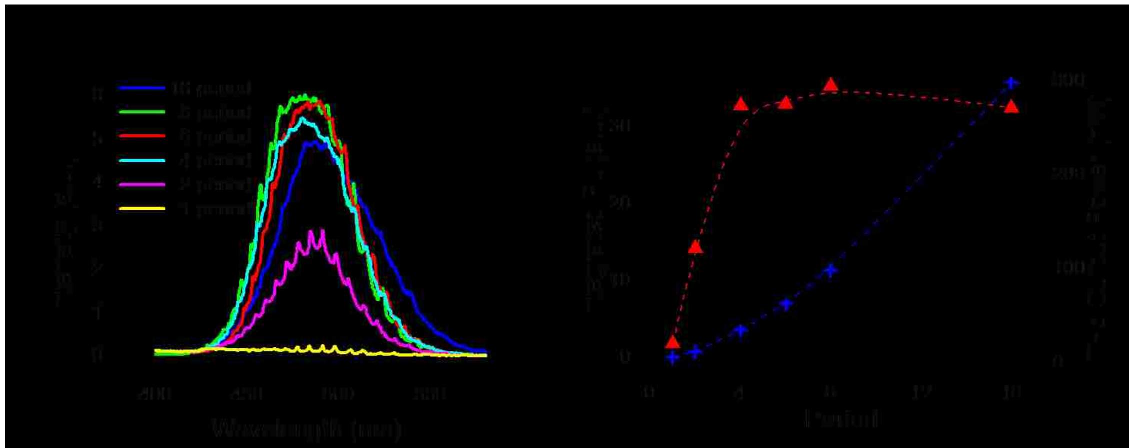

Fig. 2.7. (a) PL spectra of InGaN quantum wells with different periods measured at room temperature. (b) PL intensity and THz output power versus well period. Red triangular corresponds to PL intensity and blue cross corresponds to THz output power. The pump fluence is set as 85 μJ/cm^2.

it will change THz output power and PL intensity. The structures are listed in Table 2-1 as sample 2 to 7. The indium composition and thickness of barrier and well are exactly same. We have first investigated the PL spectrum of each sample under room temperature. As shown in Fig. 2.7(a), the emission peak of each sample is located around 472 nm. The

multiple peaks modulation is induced by Fabry–Pérot resonance. The PL intensity scales up when the well period is increased up to 4. However when we further increase the well period up to 16, the PL intensity significantly saturates, see Fig. 2.7(b). Such saturation could be caused by increased density of threaten dislocations. Namely, when the thickness of QWs scales up, the accumulated stain will be increased which leads to higher density of threaten dislocations. For terahertz generation, as we can observe from Fig. 2.7(b), the output increases more than linearly even the period of QWs is added up to 16. We have attributed the THz generation mechanism to instantaneous generation of spatially-separated electron-hole pairs resulting in efficient dipole radiation. As is well known, the output power for dipole radiation is proportion to square of dipole density. Thus, under such explanation, if we further assume that in each well the absorption is constant and there is no phase difference for generated THz wave, the THz output power should be quadratically dependent on well period. The assumption that phase difference of generated THz wave in each QW is negligible makes sense since the total thickness of QWs is much smaller than wavelength of THz. Furthermore, unlike PL, the THz is generated in absorption process not in radiation process in InGaN QWs. Since the threaten dislocations will only influence radiation process, THz output power will continuously increase even the PL already saturates. Thus, in principle, we can further increase indium composition in InGaN well to enhance the internal field without worrying about the sample quality to scales up THz generation.

The dependence of the THz output power of 16-period InGaN QWs (sample 7) on pump fluence is shown in Fig. 2.8(a). Initially for pump fluence up to 40 $\mu J/cm^2$, the THz

output power quadratically increases with pump fluence, see the red fitting curve in Fig. 2.8(a). When pump fluence is further increased up to 85 μJ/cm^2, a slight deviation to quadratic fitting is observed. Such deviation has been attributed to screening effect induced by photo-generated electron-hole pairs and been supported by blue-shift of PL peak energy [2.22]. Here we have also plotted the peak energy of PL versus pump fluence, see blue dots of Fig. 2.28(b). The peak energy for such 16-period InGaN QWs exhibits a 60 meV blue-shift which appears to support the hypothesis of screening effect. However, according to theoretical calculation [2.24], screening effect will increase the effective absorption coefficient, which in definition is proportional to ratio of integrated PL intensity with pump fluence. Thus under such calculation, we should expect the integrated PL intensity will scale up more than linearly when the pump fluence is increased. In experiment, apparently the integrated PL intensity scales up less than linear with pump fluence, see red triangle of Fig. 2.8(b), indicating that absorption coefficient is

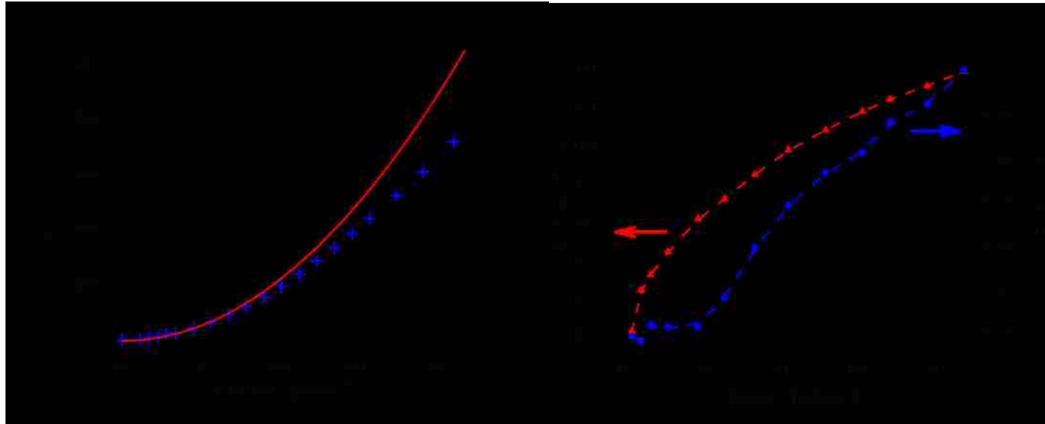

Fig. 2.8. (a) THz output power as a function of pump fluence. The crosses correspond to experiment data. The red curve corresponds to a quadratic fitting for first ten data points. (b) Integrated PL intensity and peak energy

as a function of pump fluence. The red triangles and blue dots correspond to PL intensity and peak energy, respectively.

actually reduced, which is not in consistent with screening effect. In a recent pump-probe experiment on similar InGaN QWs, the reduction of absorption has been observed for a pump fluence as low as 0.19 mJ/cm^2 and explained by increased density of hot carriers [2.25]. Thus from the dependence of integrated PL intensity on pump fluence, we may also draw a conclusion that the deviation or saturation is induced by decrease of absorption coefficient.

The conflict conclusions from PL reveal that monitoring PL signal may not be a good way to address the dynamical screening effect in THz generation process, since THz is only generated in absorption process and PL is not only influenced by absorption process but also by recombination process. Indeed, the recombination mechanism is still not fully understood in InGaN/GaN QWs. It is widely believed that the localized state plays an important role in emission process [2.26-2.28]. Such localized state will induce a band tail filling effect, resulting in blue shift when increasing pump power. Therefore the blue shift of InGaN/GaN QWs has been attributed to a combination result of screening effect and band tail filling effect [2.29]. In our detailed PL study on a similar InGaN sample, the dominant PL peak is explained by recombination of localized state [2.30]. Thus we may over emphasize the screening effect if only monitoring the blue-shift of PL peak.

An alternative method to determine screening effect is to measure the spectra of THz output of InGaN QWs at different pump fluencies. It has been pointed out in theory that, dramatic broadening and shift of THz spectra will be observed with increasing pump

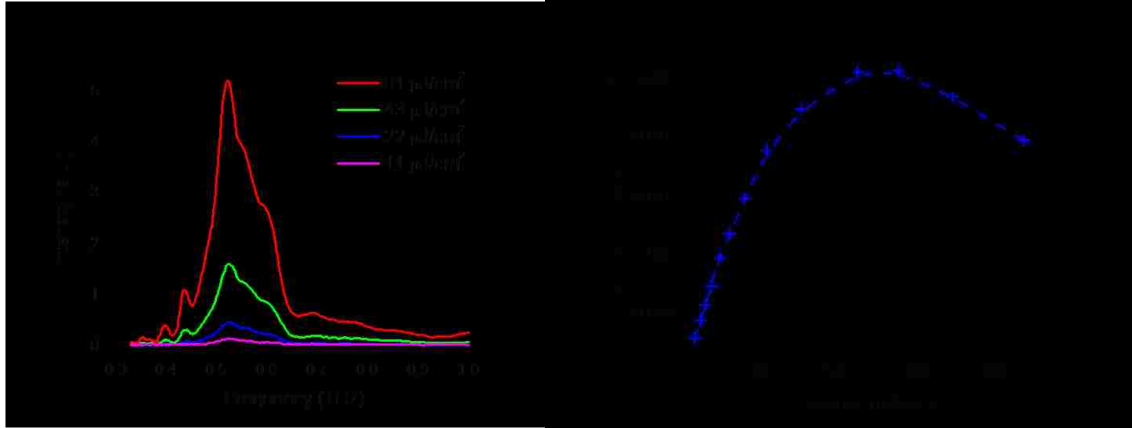

Fig. 2.9. (a) THz spectra measured at pump fluencies 11, 22, 43, 91 μJ/cm^2. (b) THz energy density generated per well as function of pump fluence.

fluence if dynamical screening is strong absorption process [2.24]. Under such predication, The THz spectral band width could far more exceed the bandwidth of excitation laser. We have measured the THz spectra under several different pump fluencies by a homemade sub-millimeter diffraction grating system. Such system allows us to detect whole THz spectra even if the bandwidth of THz is beyond the laser spectra, which is difficult to achieve in electro-optic sampling system if same laser is used to generate and sample the THz output. As is shown in Fig. 2.9(a), when the pump fluence is increased from 10 μJ/cm^2 to 90 μJ/cm^2, within the accuracy of our measurements, we do not observe a bandwidth broadening or frequency shift of THz spectra, which proves that, in our experiment, the screening effect induced by photogenerated electron-hole

pairs is negligible. Note that, our conclusion is not in conflict with Ref. [2.24], since the lowest fluence used in their calculation which only causes a small screening behavior is still about two times as large as the highest value in our experiment.

In order to see strong screening effect, we have reduced laser spot area to increase the pump fluence up to 1 mJ/cm^2. A full saturation behavior of THz output power was observed when the pump fluence is about 0.6 mJ/cm^2. This saturation pump value is agreed with Ref. [2.24]. Because of the screening effect, the highest THz energy can be generated in single pulse is limited by the total static energy originally stored in InGaN/GaN QWs. According to a simple capacitor model, the total energy stored in our InGaN QWs is estimated at least to be ~100 nJ/cm^2. Experimentally, the saturation value of THz energy density generated on each well, is only about 0.02 nJ/cm^2, see Fig. 2.9(b), which is 5000 times of magnitude lower than the theory value. Thus the screening effect is not the only mechanism to limit the THz output. One major reason is that a large amount THz output may not be collected in our experiment setup because of THz total reflection on sample surface. Indeed, since the built-in field is always perpendicular to sample surface, the most efficient radiation direction is along surface which can hardly be coupled out. In addition, we believe that free carriers inside GaN template or photogenerated carriers inside QWs will also absorb partial of THz output. Previously, the increase in the absorption of THz wave by photogenerated carriers was investigated and evidenced in GaTe [2.31] and InN materials [2.21]. Such mechanism can also explain the reduction of THz output power when the pump fluence is higher than 0.6 mJ/cm^2, as shown in Fig. 2.9(b). When the total screening is achieved, if increasing pump fluence,

more carriers will be generated but no more THz will be further generated. Since the more carriers will only increase the absorption, the THz output power will reduce.

2. 3. THz generation in InGaN/GaN dot-in-a-wire nanostructure

THz has been benefited from nanomaterials and nanofabrication for generation, field enhancement, imaging, detection and other novel applications [2.32-2.41]. Since the wavelengths of the THz wave are at least four orders of magnitude larger than the typical dimension of the nanostructures emitting the THz wave, it is very important for us to investigate THz generation from the nanostructures as the dimension is further scaled down to the atomic scale. Recently, broadband THz waves were generated by nanomaterials such as tubular $Pb(Zr,Ti)O_3$ nanostructures [2.42], plasmonic nanoparticle arrays [2.43], and an InN nanorod array [2.44]. Despite of these progresses, fundamental on THz generation from nanomaterials must be investigated in order to achieve the ultimate nanostructures in terms of normalized output power and conversion efficiency.

In this section, we report our recent experimental results following the investigation of broadband THz generation from InGaN/GaN dot-in-a-wire nanostructures.

2. 3. 1. Sample description and experimental setups

Catalyst-free InGaN/GaN dot-in-a-wire heterostructures were grown directly on Si(111) substrates under nitrogen rich conditions by radio frequency plasma-assisted molecular beam epitaxy (MBE). The InGaN quantum dots were grown at relatively low temperatures (600-640 °C) to enhance the In incorporation. Ten vertically aligned InGaN/GaN dots were incorporated in the device active region, see Fig. 2.10(a). The dot height is ~3 nm, and the thickness of the GaN barrier layer is ~3 nm. The dot widths are in the range of ~20 to 40 nm, depending on the wire diameters and also growth conditions. A 45° titled scanning electron microscopy (SEM) image of the InGaN dot-in-a-wire heterostructures grown on a Si(111) substrate is shown in Fig. 2.10(b). The areal density of the nanowires is estimated to be ~1×10^{10} cm^2. Detailed structural characterization of the InGaN dot-in-a-wire nanoscale heterostructures is described in Ref. [2.45]. For THz and PL measurement, the setup is same as what we used for InGaN/GaN QWs, see Fig. 2.2(b).

2. 3. 2. THz output power and spectra

We first measured the THz signal from three different samples. Sample 13 is GaN nanowires without InGaN dots. Sample 14 is grown under same condition with ten InGaN dots inside wire. The third sample has same structure as sample 14. However the top and bottom section of GaN nanowire of sample 15 are doped with Mg and Si, resulting in p-type and n-type regions respectively.

The THz output powers generated by these three samples are listed in Table 2-2. As we can see, the GaN nanowires without InGaN quantum dots basically have no THz output. On the other hand, the THz output powers for two InGaN/GaN dot-in-a-wire samples are about 45 nW and 330 nW under an average pump power of 400 mW. A typical spectrum measured by a grating system is illustrated in Fig. 2.11(a), covering the wavelength range from 200 μm to 1000 μm. Comparing the experiment results among

Table 2-2. THz output and PL information of InGaN/GaN dot-in-a-wire. PTHz stands for THz output power. I, λ and ΔE designate integrated intensity, peak wavelength of PL, and blue shift of the peak induced by increasing pump power, respectively.

Sample	P_{THz} (nW)	I_{PL} (a.u.)	λ (nm)	ΔE (meV)
13	0.7	N/A	N/A	N/A
14	45	2.61	547.7	71
15	350	1	558.1	91

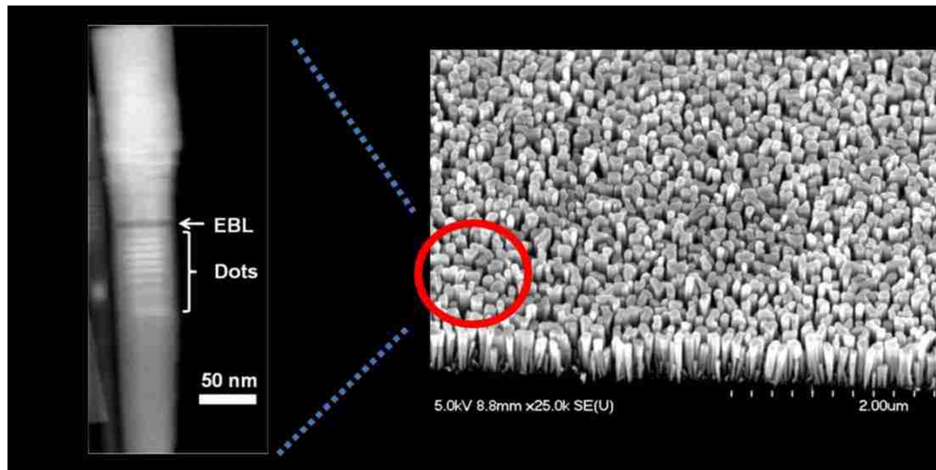

Fig. 2.10. (a) A low magnification bright field scanning transmission electron microscopy image showing the position and vertical alignment of the InGaN dots in a GaN nanowire. (b) A 45 ° tilted scanning electron microscopy image showing the morphology of the InGaN/GaN dot-in-a-wire heterostructures grown on a Si (111) substrate.

such three samples, we can first draw a conclusion that the THz wave is primarily generated by InGaN QDs. Considering the effective length of each quantum wire containing the ten vertically-aligned quantum dots to be about 30 nm, these dot-in-a-wire nanostructures are extremely efficient for the THz generation. For comparison, we have investigated the THz generation from a 180-nm $In_{0.36}Ga_{0.64}N$ thin film. According to our result, the output power is measured to be 112 nW. If we normalize the THz output

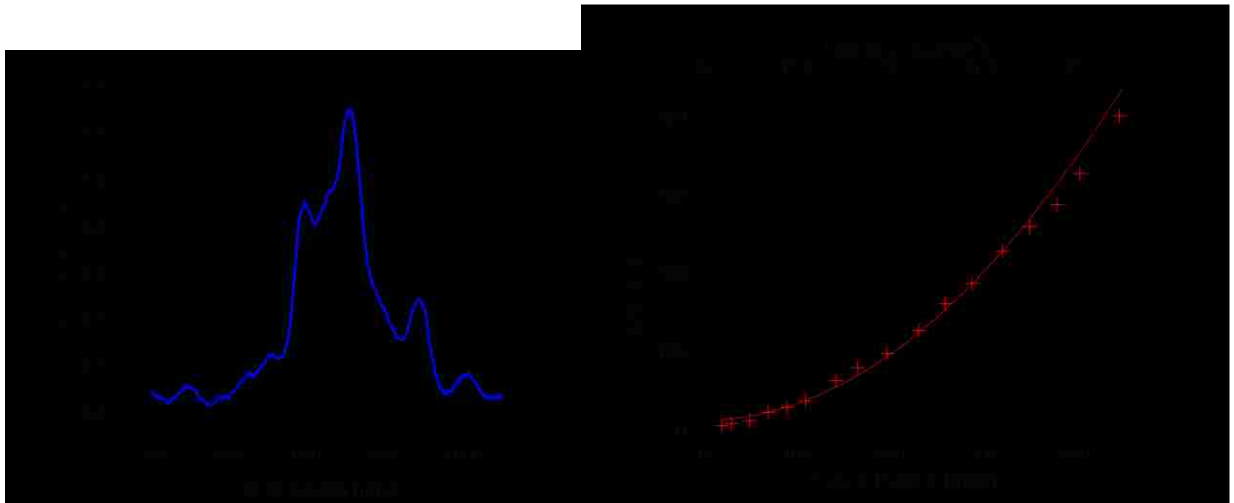

powers by the square of the pump power and length of the wires, the normalized output power generated by the InGaN dot-in-a-wire structure is more than 100 times larger than that from the $In_{0.36}Ga_{0.64}N$ thin film. We have also compared the results from the dot-in-

Fig. 2.11. (a) Typical THz spectrum emitted by InGaN/GaN dot-in-a-wire. (b) THz pump power vs. pump power or fluence. Cross corresponds to experiment result and curve is quadratic fitting.

a-wire structure and InN thin film which has been considered as one of the most efficient materials for THz emission. Under a similar experimental setup, the highest average output power of InN was measured to be about 2.4 μW with a thickness of 220 nm and a pump power of 1.5 W.The normalized output power from the dot-in-a-wire structure is at least two orders of magnitude higher. If further taking it into consideration that InGaN dots only fill around the tenth of the entire sample area, the radiation power from our InGaN/GaN dot-in-a-wirestructure is four orders of magnitude higher than that from the InGaN or InN thin film. Even compared to 8-period $In_{0.25}Ga_{0.75}N$/GaN, this normalized value is 5 times larger.

To find out the underlying reason why the THz output power from the doped sample is significantly higher than the undoped sample, we should first determine the mechanism for the THz radiation from these three samples. Broadband THz generation in semiconductor materials under excitation of ultrafast laser pulses can originates from either photocurrent surge or optical rectification [2]. However, the mechanisms for the THz generation from InGaN/GaN dot-in-a-wire structures are completely different from these two mechanisms above.

To rule out optical rectification as a possible mechanism, we simply set the pump laser wavelength to 782 nm by removing the nonlinear crystal as a frequency-doubling medium. At such a wavelength, the THz output power is close to several ten picowatts. If the THz is generated by optical rectification, we should able to observe efficient THz

conversion if the photon energy is below the effective bandgap of the InGaN quantum dots. We have ruled out photocurrent surge as a possible mechanism. Indeed, the photon energy corresponding to the laser wavelength 391 nm is higher than the bandgap of the InGaN QDs, but lower than that of the GaN barrier. The carriers generated by the laser beam are localized inside the dots which do not contribute to photocurrent inside each quantum wire. In 8-period InGaN/GaN quantum wells (QWs) having the total thickness of the wells being 24 nm studied by us previously, the THz output power is about 10 times higher than that of a 180-nm InGaN film. If the THz wave inside the InGaN well were generated by photocurrent, the thicker InGaN film would be more efficient than the InGaN QWs for the THz radiation. Such a comparison further supports our claim that photocurrent can be ruled out.

For our InGaN dot-in-a-wire structures, the width of the dots is one order of magnitude larger that its thickness, making it function as a quasi-QW structure. Thus, the internal field of such nanostructure can be as large as that inside the InGaN/GaN QWs. Obviously, for light emitting devices based on an InGaN/GaN heterostructure, the built-in electric field causes light emission efficiency to dramatically drop since such a field spatially separates electron and hole wave functions resulting in the dramatic reduction in the efficiency of electron-hole recombination. In contrast, the same large internal field in InGaN dots are exploited by us to efficiently generate THz waves. Assuming that a pair of electron and hole is generated, due to the separation of the electron and hole induced by the large internal field, a dipole is generated. the nanostructure is under the excitation of femtosecond pulses, the dipole moment changes in a femtosecond time scale, which

results in efficient dipole radiation in the THz frequency range. Thus the generation mechanism is same as THz generation inside InGaN/GaN QWs. InGaN/GaN dot-in-a-wire structure has some obvious advantages over the InGaN QWs. First, THz waves generated by the InGaN/GaN dots could be more efficiently radiated out due to the significant increase in the effective emitting area [2.44]. Second, compared to the QWs, QDs are really three-dimension nanomaterials which could be used as a quasi-point THz emitter. Indeed, the total power radiated by ten QDs may reach 10 pW, which is significantly higher than the noise level of the detector based on QDs [2.46]. Moreover, by carefully designing an array of QDs, the THz output power can be dramatically scaled up. Therefore, by nano-engineering arrays of QDs, nanoemtters and nanodetectors could be integrated into the same chip, which can be eventually used for realizing a number of unique applications. For example, two wires with uniquely-designed QDs can be placed at the two focuses of an ellipsoidal mirror. One is an emitter while the other is a detector. The THz output from the emitter can be completely collected by the receiver. Such a nanosystem can be used for sensing applications.

By p-type and n-type doping in the top bottom layers of the GaN wire, respectively, a p-n junction is formed. Such a p-n junction creates an additional electric field with its direction being the same as that of the built-in field. The net increase in the electric field results in a larger separation between the photogenerated electrons and holes. According to equation (2-5), the larger separation further increases the radiated power. Previously, broadband THz generation was observed on Si p-n junction [2.47]. In our experiment, the THz power is enhanced by the increase in the electric field inside the InGaN QDs. To

support our claim, we have measured photoluminescence (PL) from the dot-in-a-wire nanostructures. As shown in Fig. 2.12(a) and Table 2-2, we have observed the slight redshift of the peak energy of the doped sample. Meanwhile, the PL intensity is weaker than that from the undoped sample. As the electric field is increased, the transition energy is red-shifted owing to QCSE. In addition, due to the further separation between the photogenerated electrons and holes, the overlap between the wave functions of the electrons and holes is reduced, resulting in the reduction in the PL intensity.

In our experiment, both samples exhibit blue shift when the laser power is increased to 20 mW, see Fig. 2.12(b). As mentioned above, the photogenerated carriers effectively screen the internal electric field. Therefore, as the carrier density is increased, the net electric field is reduced due to the screen effect. Due to QCSE, the transition energy is blue-shifted. According to Fig. 2.12(b), the amount of the blue-shift for the doped sample is significantly larger than that for the undoped sample. This is clear evidence that the net electric field inside the QDs of the doped sample is significantly larger. To further increase the THz output power, we fabricated an InGaN/GaN light emitting diode (LED), see Fig. 2.13(a), (b)&(c). The InGaN/GaN dot-in-a-wire

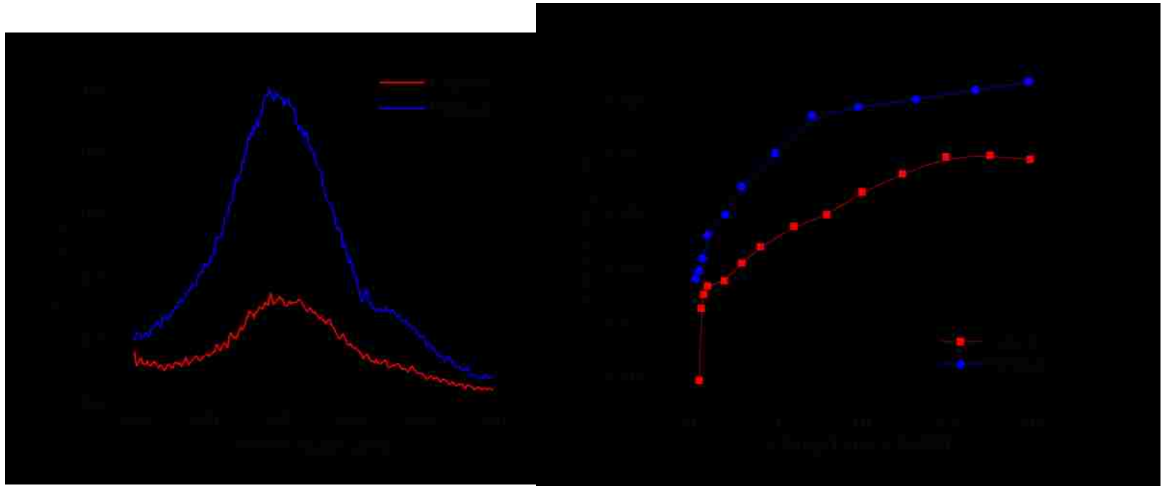

Fig. 2.12. (a) Typical PL spectrum of doped and intrinsic InGaN/GaN dot-in-a-wire nanostructure. (b) Energy of PL peak vs. pump power of doped and intrinsic InGaN/GaN dot-in-a-wire nanostructure.

arrays were first planarized using a polyimide resist layer by spin-coating, followed by an appropriate dry etching process to reveal the top GaN:Mg sections of the dot-in-a-wire heterostructures. P- and n-metal contacts, consisting of Ni/Au/indium tin oxide (ITO) and Ti/Au layers, were then deposited on the exposed wire surface and the backside of the Si substrate, respectively. The size of device is 1×1 mm^2. Detailed structural characterization and device fabrication of the dot-in-a-wire nanoscale heterostructures is described in Ref [2.45]. The performance of such a device can be evaluated by adding forward electric field, which shows clearly luminescence in the green to yellow regions. As is shown in Fig. 2.13(d), when the reverse field is increase up to 5 V, the THz output power is enhance by a factor of 4.2. Such a result indicates that under the reverse bias, the electric field produced by the external bias is in the same direction as that for the internal electric field. This is consistent with the mechanism for the THz generation. In contrast,

for the efficient light emission, a forward bias must be applied. However, in such case the THz output slightly reduces.

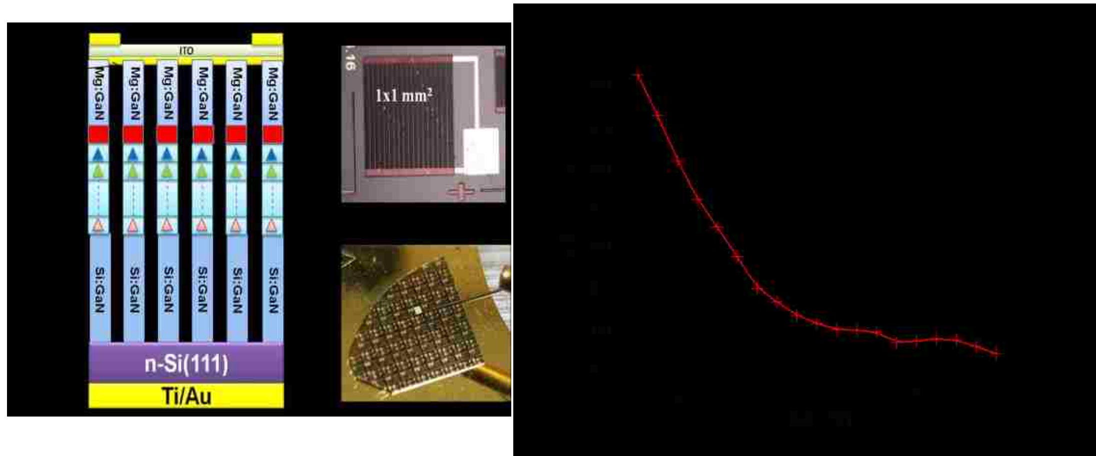

Fig. 2.13. (a) Illustration InGaN/GaN dot-in-a-wire LED. (b) The optical microscopy image of the fabricated dot-in-a-wire LED. (c) Picture of LED under forward bias. (d) THz output power vs. bias applied to dot-in-a-wire LED.

In conclusion for this part, a sub-microwatt broadband THz wave is generated from an InGaN/GaN dot-in-a-wire structure due to instantaneous dipole radiation induced by ultrafast laser pulses in the presence of the internal electric field. The high efficiency is directly correlated to the very large internal field due to piezoelectric and spontaneous polarizations. The normalized THz output power is found to be four orders magnitude higher than that from the InN or InGaN thin film. By applying an external reverse bias to the nanodevice, the THz output power is increased more than fourfold. Our result brings us a step closer to engineer a THz nanosystem for realizing various applications.

2. 4. Summary

To summarize chapter 2, we claim microwatt broadband THz has been generated in InGaN/GaN heterostructures, including QWs and dot-in-a-wire nanostructure. The generation mechanism has been attributed to dipole radiation due to internal electric field in InGaN/GaN heterostructures. THz output as function of many factors, including periods, incident and polarization angle and indium composition etc. has been studied. Specifically, PL has been used to study the carrier screening effect. If considering the total thickness of absorption layer is less than 30 nm, we believe InGaN/GaN heterostructures are one of the most efficient materials for broadband THz generation. By optimizing the experimental setups, sub miliwatt THz can be expected.

Chapter 3. Potential Laser Cooling on GaN

3. 1. Introduction

The term “laser cooling” is most often used for cooling and trapping of dilute gases of atoms and ions to extremely low temperatures. This area of science has progressed rapidly in the last two decades and has facilitated the observation of Bose-Einstein condensates and many related phenomena [3.1, 3.2]. It is surprising to mention that, before half century of achievement of Doppler cooling of atom gas and even invention of

laser, the concept of optical cooling of solids by anti-Stokes photoluminescence (ASPL) has already proposed by German physicist Peter Pringsheim in 1929 [3.3], See Fig. 1(a). The basis for this process is straightforward [3.4], see Fig. 1(b): First, using a light source of which the photon energy is same as the bandgap of solid materials. By absorption the energy of such photon source, electrons from ground states will be pumped to excited states. Since the photon energy is exactly equal to bandgap of the materials. These excited electrons will be all located at bottom of excited states. After that however, as we all know, under quasi-thermal equilibrium condition, the electrons distribution in excited states should also follow Fermi-Dirac distribution which means the electrons cannot all stay at the bottom. Thus, after electrons reach quasi-thermal equilibrium through scattering with lattices, average energy of electrons is higher than what they get from the pump source. The energy difference is actually compensated by lattice vibration energy, i.e. phonon energy. In last step, the electrons in excited states will decay to ground states. If all the electrons will lose their energy by emitting photons or in other words, the luminescence quantum efficiency is 100%, the lattice thermal vibration energy is extracted from the solid. As a result, such solid material is then cooled by removing phonons.

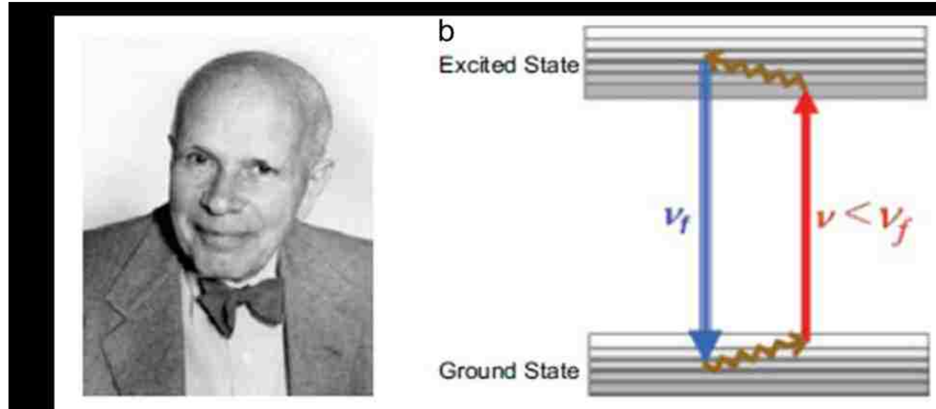

Fig. 3.1. (a) Peter Pringsheim. (b) A scheme of anti-Stoke photoluminescence. (Figure reproduced from Ref. [3.4]).

Following the above analysis, we can understand following three things. First, accompanying with optical cooling process, we should observe anti-Stoke photoluminescence, i. e. $v_f > v_p$, where v_f and v_p are fluorescence and pump frequency respectively. Secondly, to achieve net cooling, the quantum efficiency for fluorescence should be very high. Simple calculation shows that the quantum efficiency, i. e. η_{QE} should be at least higher than v_p/v_f. Typically the quantum efficiency of solid in optical cooling experiment is higher than 97%. Thirdly, assuming the quantum efficiency is 1, the cooling efficiency or fractional cooling energy for each electron, i. e. η_C is equal to $(v_f - v_p)/v_p$. In thermal equilibrium condition, $h\,(v_f - v_p)/hv_p = k_B T/hv_p$. Assuming hv_p is around 1 eV, typical cooling efficiency is less than 5%.

Although such concept of optical cooling on solids is proposed more than eighty years ago, due to lack of narrow linewidth light source, i. e. laser, the early research is only focused on whether in principle it is possible. Initially, it was believed that optical

cooling by the anti-Stokes fluorescence contradicted the second law of thermodynamics. Predictions suggested that the cycle of excitation and fluorescence was reversible, and hence the optical cooling would be equivalent to the complete transformation of heat to work [3.5, 3.6]. Such issue was cleared by Landau by assigning entropy to radiation [3.7]. It was shown in his paper that the entropy of a radiation field increases with its frequency bandwidth and also the solid angle through which it propagates. Following by such analysis, if the incident light source has a very small bandwidth and propagates in a well-defined direction, it has almost zero entropy. Obviously, laser perfect meets such requirement. On the other hand, the fluorescence is relatively broadband and is emitted in all directions and, therefore, it has comparatively larger entropy. In this way, the second law of thermodynamics is satisfied.

After invention of laser, the requirement of very high fluorescence quantum efficiency prevents the observation of laser cooling of solids for decades. In 1968, Kushida and Geusic [3.8] attempted to cool a Nd^{3+}:YAG crystal with 1064 nm laser radiation. They reported a reduction of heating. However no net cooling has been observed. Only until 1995, Epstein *et al.* first experimentally demonstrated with the ytterbium-doped fluorozirconate glass ZBLANP:Yb^{3+} [3.9]. Nowadays, laser cooling using rare-earth doped materials approaches cryogenic temperatures, and, efficiency-wise, already bests the performance of a typical thermoelectric cooler [3.10]. Optical refrigeration will be useful in applications such as satellite instrumentation and small sensors, where compactness ruggedness, and the lack of vibrations are important. Optical

refrigeration is well suited for space-borne applications since it has no moving parts and can be designed for long operational lifetimes.

Although, optical refrigerator is based on cooling of some rare-earth doped insulating crystal is well developed, it would be practical laser cooling could be implemented directly inside semiconductor material as it is the active semiconductor device that needs to be cooled in the end, and most of the rare earth host materials have low thermal conductivity and also make poor thermal contact with semiconductors. Furthermore, optical refrigerators based on semiconductors have a potential for cooling devices down to ~ 10 K [3.11, 3.12]. Such a low temperature may not be reachable using rare-earth doped solids, since the top of the ground state at such a low temperature is significantly de-populated during the light emission. In comparison, semiconductors do not suffer from such an obstacle since valence band is always populated by electrons.

With all the advantages offered by semiconductors for laser cooling, this field has been intensively investigated both theoretically and experimentally [3.11-3.19]. In the past, most efforts have been devoted to the exploitation of GaAs since GaAs technology is the most mature among the direct gap semiconductors and the external radiative recombination efficiencies, exceeding 96% have been observed in GaAs/GaInP heterostructure [3.20]. Radiative recombination efficiency plays the key role in laser cooling, since in each act of Anti-stokes photon emission only about $k_B T$ of energy is being carried away, i.e. a small, about 1% fraction of the incident pump photon energy, hence nonradiative loss of just 1% may be fatal for the cooling. And yet, despite all the

aforementioned attractive features of GaAs, no net cooling has been attained in this material, notwithstanding all the persistent efforts that came tantalizingly close to it. Instead, rather unexpectedly, first observation of optical cooling in semiconductor has been recently made in CdS nanobelts rather than in GaAs [3.21]. It was suggested in such a paper that the strong exciton-longitude optical (LO) phonon coupling through Fröhlich interaction played an important role in achieving optical cooling in semiconductors. In polar semiconductors such as GaAs and CdS, the dominating mechanism for ASPL is through exciton- LO phonon coupling [3.16]. Thus, compared with III-V materials such

Table 3-1. Bandgap and Fröhlich coupling constants of several semiconductors (see Ref. 3.27)

System	Materials	α_F	Eg (eV)
IV	Si	0	1.12
III-V	GaN	0.48	3.4
	GaP	0.201	2.26
	GaAs	0.068	1.424
	InP	0.15	1.344
II-VI	CdSe	0.16	1.49
	CdS	0.51	2.5

as GaAs, more polar II-VI materials such as CdS are expected to produce more efficient ASPL since the corresponding Fröhlich interaction is stronger. Indeed, phonon-assisted ASPL has been widely observed in II-VI quantum dots, including CdSe [3.22], PbS [3.23], PbSe [3.24], and CdTe [3.22, 3.25], which motivates the discussion of laser

cooling on these materials [3.26]. Besides its strong Fröhlich interaction, the bandgap of CdS is significantly larger than GaAs (2.4 eV vs 1.51 eV). The idea that wider bandgap materials may hold an advantage when it comes to laser cooling due to their large joint density of states, lower refractive index, and, most crucially, very weak Auger recombination, was first explored in Ref. [3.17]. In Table 3-1, we have listed the data of bandgap and Fröhlich coupling constant of several semiconductor materials. The Fröhlich coupling constant, i.e. α_F, represents the strength of electron and LO phonon coupling. As is shown from this table, we can first recognize that the Fröhlich coupling constants of II-VI are indeed overall larger than those of III-V materials. For example, the Fröhlich coupling constant is 0.51 and 0.068 for CdS and GaAs respectively [3.27]. However, among listed III-V semiconductors, GaN has nearly same Fröhlich coupling constant compared with CdS. It appears that wide gap polar III-V semiconductors, such as GaN and its alloys with AlN and InN which have been widely used in both electronics (high speed and high power transistors [3.28]) and optics (LEDs and lasers [3.29]) combine many attractive properties for laser cooling: strong electron-phonon interaction, large phonon energy, high joint density of states (less saturation), wide bandgap (less Auger recombination) and small refractive index (less light trapping). Compared to II-VI semiconductors, GaN has reached a mature technology where the many technical issues associated with growth, fabrication and also getting the light out had been already successfully resolved. Hence, it is only natural to start commence experimental effort that one day should read to efficient optically-driven semiconductor refrigerators monolithically integrated with the electronic and optical devices.

In this chapter, we report the first step on the road to the laser refrigeration using GaN – experimental demonstration of strong anti-Stokes light emission in a free-standing GaN sample. These results, with necessary caution, allow us to make prediction that laser cooling may be achieved in GaN in the relatively near future.

3. 2. Sample description and experimental setups

The sample used in our experiments is 350-μm free-standing GaN wafer grown by metal organic chemical vapor deposition (MOCVD). The concentration of Si donors is measured to be 2×10^{18} cm^{-3}. Such a sample was mounted on a cold finger of a continuous-flow cryostat with its temperature being set anywhere from 4.2 K to 300 K. The pump source was a Ti:sapphire laser with a 3 ps pulse length, repetition frequency of 76 MHz and wavelength tunable from 730 nm to 850 nm, These pulses were subsequently frequency doubled and then quadrupled by using two BBO crystals which allowed us to excite GaN both across and above the bandgap. A typical focal spot area of the pump beam on the GaN sample is 0.02 mm^2. The photoluminescence (PL) signal generated by the GaN material was analyzed with a double-grating spectrometer with and a photomultiplier tube.

3. 3. Results and discussions

We first measured PL spectra when the pump photon energy was well above the bandgap of GaN, corresponding to the pump wavelength of 209 nm with an average power of 500 μW. The PL spectrum of GaN obtained at 6 K is shown in Fig. 3.2(a). The dominant peak located at 357.3 nm corresponds to the recombination of the excitons bound to neutral donors (D-X or I_2) whereas a small peak around 368.13 nm is caused by recombination of electrons bound to the donors with free holes (D-h). The three peaks at 380.08 nm, 390.96 nm, and 402.49 nm correspond to the recombination of the donor-acceptor pairs (DAP) and its 1LO-phonon and 2LO-phonon replicas, respectively. The strong intensities of LO-phonon replica of DAP indicate the strong coupling between electrons (or holes) bound to donors (or acceptors) and LO phonons. When the sample temperature is increased, the peak of DAP progressively evolves towards the exciton peek, as also shown in Fig. 3.2(a), and eventually, above 200 K all the sharp features in the spectrum disappear. As can be seen from the absorption spectrum at room temperature in Fig.

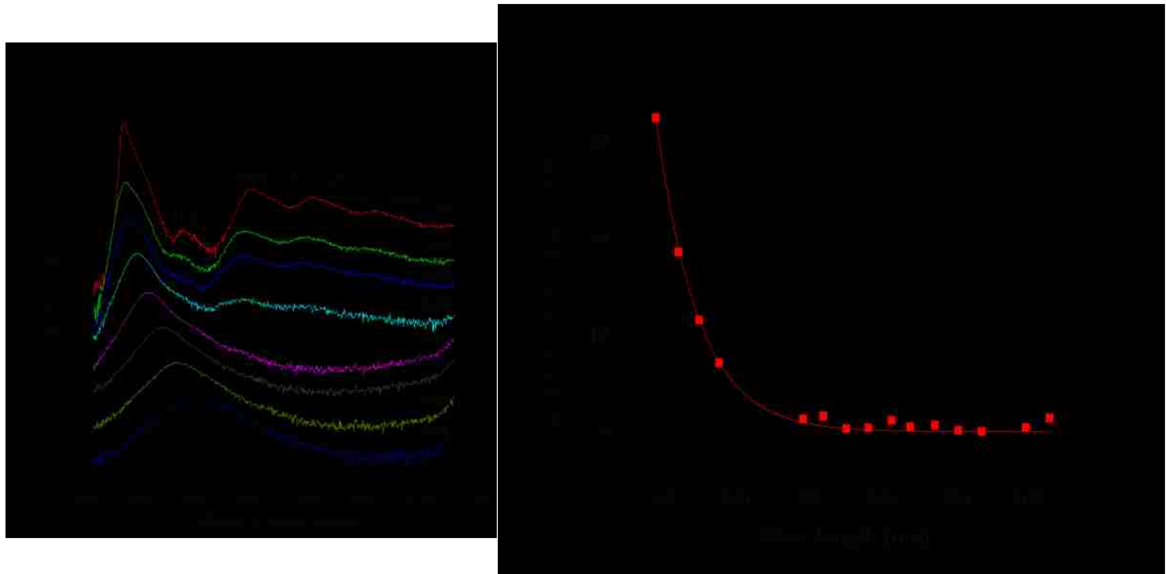

Fig. 3.2. (a) PL spectra excited by 209 nm with an average power of 0.5 mW at different temperatures. (b) Absorption spectrum at 300K. Squares are experiment data and curve is exponential decay fitting.

3.2(b) at an elevated temperature one can only observe exponential bandtail, devoid of any features, from which the luminescence emerges. The center of PL peak shifts rather substantially towards longer wavelength as temperature increases, in a general agreement with the temperature dependence of the bandgap described by the Varshni equation [3.30]. Note, that this sensitivity of the emission wavelength to the temperature can be exploited to determine the temperature of the optical refrigerator indirectly [3.4].

Next, after following the evolution of emission peaks with temperature using above-the-gap excitation, we have moved closer to the study of laser refrigeration by setting the pump photon energy below the bandgap. The ASPL spectra have been shown in Fig. 3.3. The red curve of Fig. 3.3(a) shows a typical ASPL spectrum measured at the pump wavelength of 385.6 nm at room temperature. Fig. 3.3(b) shows the ASPL spectrum

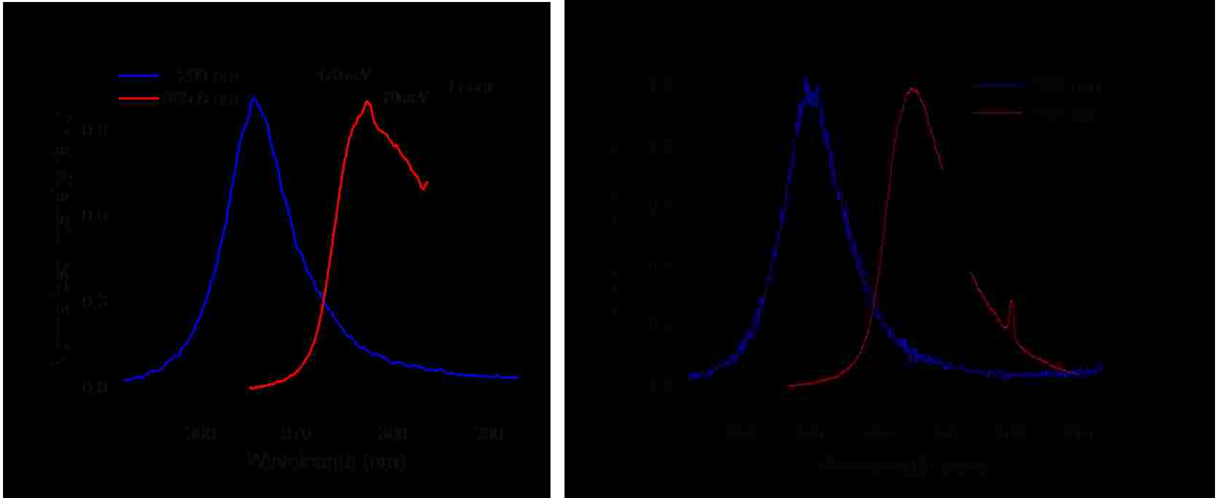

Fig. 3.3. (a) Normalized PL spectra measured at 300 K. The blue and red curves are excited by 209 nm and 385.6 nm respectively. (b) Normalized PL spectra measured at 390 K. The blue and red curves are excited by 209 nm and 392 nm respectively.

measured at 390 K which contains clearer signal. It is worth noting that the corresponding photon energy of such pump is below the center energy for the dominant ASPL peak by 71 meV which is only slightly less than LO phonon energy of 92 meV and substantially larger than $k_B T$ – in a full agreement with the results showed in Ref. 10. Obviously, the ASPL occurs as a three step process – the LO-phonon-assisted absorption of the pump photon, followed by the thermalization in the band accompanied with releasing acoustic phonons that carry away about 21 meV of energy to the lattice, and the final step of direct radiative recombination that does not involve the phonons. It is also clear that what is observed is ASPL and not AS Raman scattering in which the Anti-stokes shift is always equal to the phonon energy.

Compared with the PL obtained by pumping well above bandgap shown by the blue curve in Fig. 3.3(a) the ASPL excited below the gap (red curve) is about 106 meV lower, indicating that the absorption below the gap is relatively weak and it cannot easily fill up the states above the gap. In fact, by comparing with the absorption spectrum of Fig. 3.2(b) one can see that not only the absorption of laser light but also the ASPL itself originate in the states below the nominal bandgap in the so-called Urbach tail [3.31] with an exponential density of states. As shown in Ref. [3.17] the exponential density of states is advantageous for laser cooling and the semiconductor should be excited below the nominal bandgap into the Urbach tail whose origin is either of extrinsic (i.e. due to defects/impurities), or intrinsic (phonon-assisted absorption) nature. The extrinsic Urbach tail is less suitable for the laser cooling since it is often accompanied by the background absorption. This background absorption, whose nature is not certain, is very weak, but presents a serious obstacle to laser cooling of semiconductors. Furthermore, conceptually using impurity-related Urbach tail for refrigeration is not significantly different from that using the donor-acceptor transition below the gap for the same purpose. The latter concept had been explored in Ref. [3.16]. While it was found to have an advantage in terms of cooling threshold, the cooling power was found to be very limited due to saturation of the donor-acceptor transition.

At the same time, the Urbach tail originating from the phonon-assisted absorption seems to be a natural match for laser refrigeration – it is almost always guaranteed to produce strong Anti-stokes shift in PL as the joint density of electronic states in the band, i.e. above the photon energy is always larger than the density of states below the gap. The

potential of using the phonon-assisted Urbach tail absorption for laser cooling had been investigated in Ref. 10 where it had been shown that while this absorption does get saturated, it usually occurs at relatively high powers. In the same work it was shown that there also exists a Stokes-shifted luminescence due to phonon-assisted electron-hole recombination (the process reverse to phonon-assisted absorption) but with a proper selection of excitation wavelength one can always assure that it is the anti-Stokes luminescence that dominates, as was indeed observed in our experiments. What makes phonon-assisted Urbach tail particularly attractive for laser cooling is that exists in high-purity materials and thus is not inherently accompanied by the bane of optical refrigeration – background absorption.

It is rather evident that the prospective for laser cooling improves when the Urbach tail gets enhanced in both depth and strength. The strength of phonon-assisted absorption is proportional to the strength of electron-phonon interaction in solids – Fröhlich interaction that is particularly effective for LO phonons in polar semiconductors. The depth of the tail, i.e. how far below the bandgap it extends in the energy space, is commensurate then with the energy of LO phonons Under such an analysis, GaN is a good candidate for laser cooling, not only it has strong Fröhlich interaction (Fröhlich coupling constant is 0.48, 0.51, 0.07 for GaN, CdS and GaAs respectively [3.27]) but also has very large LO phonon energy (92 meV, 37 meV, 36 meV for GaN, CdS and GaAs respectively).

Of course, in the end it is the ASPL efficiency that matters for laser cooling, and in our experiments we have measured only an ASPL output power of 300 nW with the pump power of 30 mW at 385.6nm, mostly due to the fact that only 5% of the pump beam is absorbed by the GaN wafer and also since most of the photoluminescence can be not directly coupled out due to total internal reflection. The ASPL efficiency can be improved by using nanostructures or an index-match dome [3.4] and also introducing an optical cavity for the pump wavelength.To confirm that the ASPL of GaN is indeed a phonon-assisted phenomenon, we have measured the intensity of ASPL as a function of the pump power. Besides phonon-assisted ASPL, luminescence upconversion in semiconductors can also be induced by two-photon absorption [3.32]. The intensity of ASPL induced by two-photon absorption is expected to be proportional to the square of the pump power. For the phonon-assisted ASPL, however, the power dependence should be linear since only one photon is required for each transition. As we can see from Fig. 3.

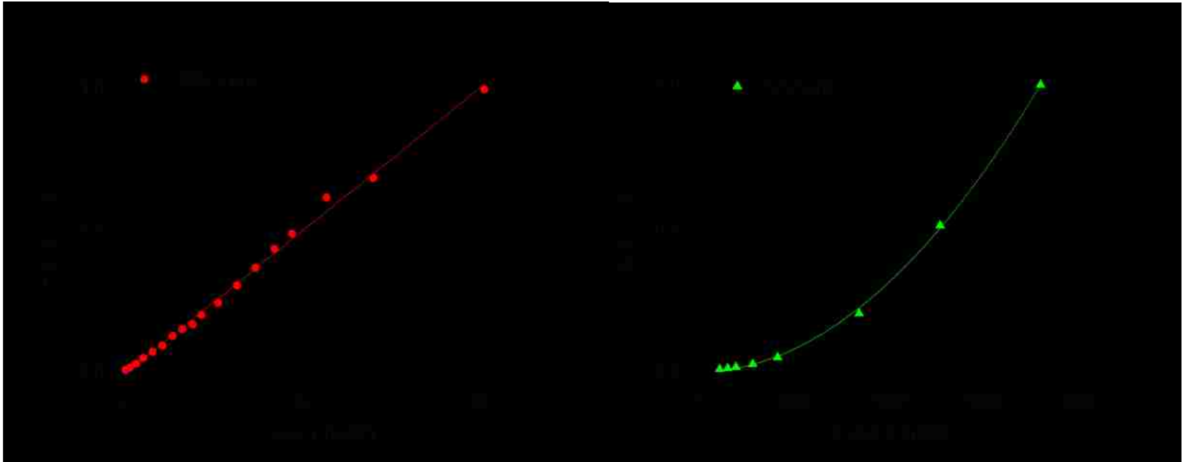

Fig. 3.4. Integrated PL intensity as a function of laser power measured at 300 K: (a) excited by 385. 6 nm. (b) excited by 532 nm. The solid red and green lines are linear and quadratic fitting respectively.

4(a), the integrated intensity of ASPL is proportional to the pump power for the powers of up to 40 mW. In comparison, Fig. 3.4(b) shows that when a CW laser beam at 532 nm, i.e., well below the bandgap is used to generate a PL signal from GaN, the dependence of the luminescence intensity on the pump power shows a clearly quadratic behavior. It should also be pointed out that the intensity of PL induced by two-photon absorption is at least four orders of magnitude lower than that for the phonon-assisted ASPL pumped at 385.6 nm.

One can see the transition between the phonon-assisted and two-photon ASPL in Fig. 3.5(a), where the pump wavelength had been tuned in the range of 383-410 nm. As the pump wavelength is increased, the ASPL intensity is decreasing rapidly following nearly-exponential decrease predicted Ref. 10. This behavior persists when the photon energy is below the bandgap by more than 1 LO phonon energy indicating the gradual switch to the absorption involving two phonons and a phonon. Note that a similar behavior was observed on the ASPL experiment of GaAs quantum wells [3.18] and CdSe quantum dots [3.26]. However, as the pump wavelength is increased to beyond 400 nm, the PL signal ceases to decrease and more or less stays constant, indicating that in this range two-photon absorption, earlier reported in GaN [3.34] is stronger than weak phonon-assisted absorption involving three or more LO phonons. To confirm this assumption of graduate change from phonon-assisted to two-photon absorption, we have measured the ASPL intensity as a function of the pump power at several different pump wavelengths. As is shown by Fig. 3.5(b), with increasing the pump wavelength from 382.1 nm to 409.1 nm, the power dependence gradually evolves from linear (phonon-assisted absorption) to the

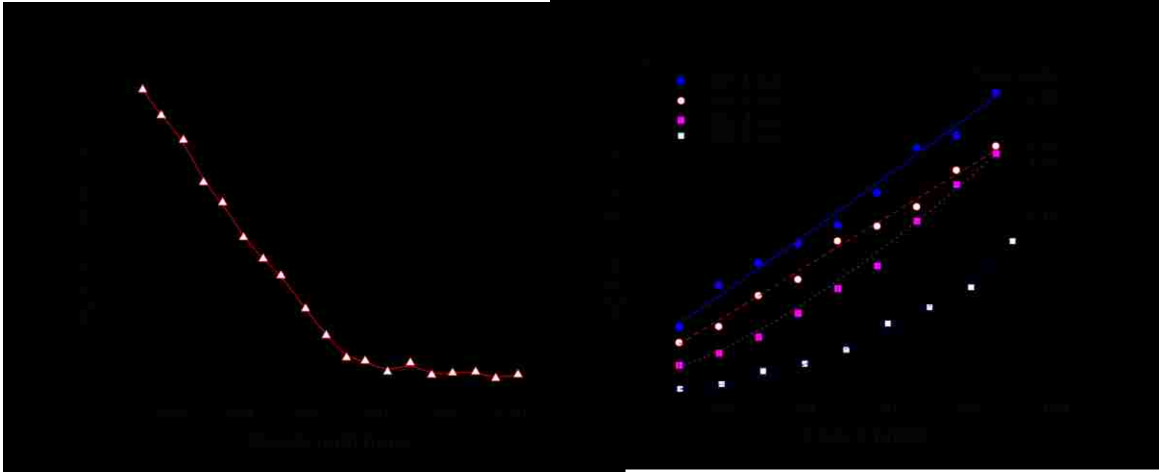

Fig. 3.5. (a) Integrated PL intensity as a function of pump wavelength measured at 300 K. The laser power is set as 20 mW, the solid line is guide for the eye. (b) Integrated PL intensity as a function of laser power for four wavelengths measured at 300 K. The experiment data have been fitting by $I \propto P^{\alpha}$, where I is integrated PL intensity, P is laser power and α is power index.

quadratic (two-photon absorption). Obviously, two-photon absorption leads to heating rather than cooling of sample and it is desirable to reduce it which suggests using CW rather than pulsed pump.

Perhaps, the clearest signature of the phonon-assisted ASPL is the increase of the intensity with the temperature rises [3.26]**.** As shown in Fig. 3.6, the intensity of ASPL scales up quickly with the temperature from 150 K to 390 K. It is worth noting that since the intensity of phonon-assisted ASPL is very sensitive to the separation between the pump and emission photon energies, see Fig. 3.5(a), during such a measurement the pump laser is tuned to set its photon energy always about 1LO phonon energy lower than the emission peak of ASPL. Below 150 K, since the ASPL signal is significantly reduced

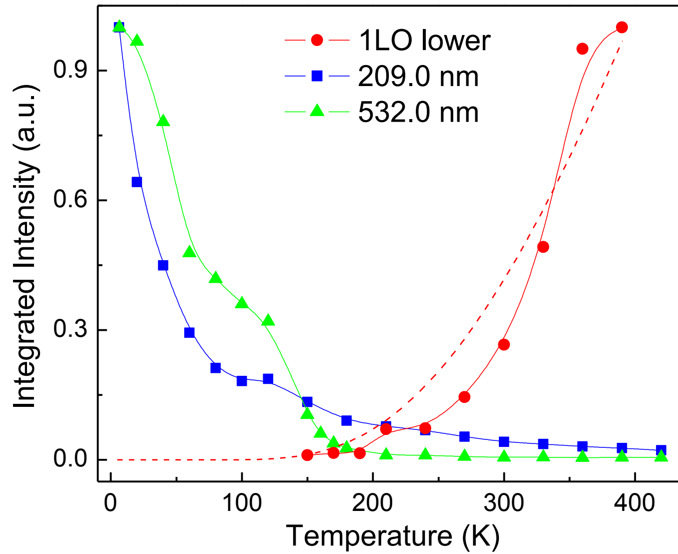

Fig. 3.6. Normalized integrated PL intensity as a function of temperature for different laser wavelengths. The solid lines are guide for eye. The dashed line is a fitting curve assuming that intensity of ASPL is proportional to number of LO phonons which is defined by Bose-Einstein statistics.

in power and strongly overlaps with the laser emission tail, hence given limitations of our experimental setup, the peak cannot be clearly distinguished from the laser spectrum. The observed temperature dependence of course follows from the Bose-Einstein distribution of optical phonons as shown by the dashed curve in Fig. 6. We have also measured the PL intensity as a function of the temperature when the laser wavelength is set to 209 nm and 532 nm, and the carriers are excited directly well above the bandgap rather than into the phonon-assisted bandtail by either one or two photon absorption. The results shown in Fig. 6 indicate that the PL intensities generated by these two pump wavelengths are reduced with increasing the temperature, in all probability due to increase in the

nonradiative recombination. Thus, the temperature behavior of ASPL of GaN strongly supports the fact that upconversion process is assisted by LO phonons.

3. 3. Summary

In conclusion of this chapter, we have observed ASPL of GaN. By measuring the power and temperature dependences of ASPL intensities, the mechanism has been attributed to phonon-assisted upconversion, which can be utilized to achieve laser cooling in GaN. Although observing phonon-assisted ASPL is only the first step on the way laser cooling, we believe that our results give us the reason to be optimistic about prospects for laser cooling using GaN.

Chapter 4. Photoluminescence Study on III-Nitrides: InGaN/GaN QWs, GaN/AlN QWs, Freestanding GaN and BN Powder

4. 1. Introduction

As we already introduced already in first chapter, III-Nitride based heterostructures, in term of quantum wells (QWs), quantum lines (QLs) and quantum dots (QDs) have been attracted a lot of attention for its wide application from deep ultraviolet (UV) to green region. For example, since Nakamura published first paper about bright luminescence from InGaN/GaN QWs [4.1], such material system has been intensively studied and yet, commercialized light emitting device such as light emitting diodes (LED) or laser diodes (LD) from blue to green region is available on market. One the other hand, GaN/AlGaN heterostructures due to its larger bandgap and larger band offser, not only can be used to fabricate deep UV light emitting device from 220 nm to 350 nm [4.2], but also have a lot of applications based on intersubband transitions [4.3]. Photoluminescence is a very effect experiment method to study the optical properties of these materials systems. In this chapter, we will present our experiment results about photoluminescence study on InGaN/GaN QWs and GaN/AlN QWs.

4. 2. Investigation of Fast and Slow Decays in InGaN/GaN QWs

Understanding the emission mechanism in InGaN/GaN quantum wells (QWs) is the key for the applications in light-emitting devices from ultraviolet to green region [4.4]. Previously, recombination from localized states was proposed as the primary mechanism for spontaneous emission in InGaN/GaN QWs [4.5]. Such an effect of carrier localization has been attributed to nanometer-scale indium rich clusters based on transmission electron microscopy until these indium clusters were attributed to the electron-beam-induced damages [4.6]. Besides indium rich clustering effect, v-shaped pits can induce carrier localization [4.7]. Recently, it was demonstrated that InGaN QWs can be grown with no indium clustering and abrupt interfaces [4.8]. In addition, polarization fields cause charge separation, and therefore, affect the carrier lifetime due to different recombination mechanisms [4.9-4.12].

Time-resolved photoluminescence (PL) was widely used to investigate the dynamic recombination processes in InGaN/GaN QWs. Carrier lifetimes in the range from sub-nanosecond to microsecond have been measured, which suggests that the carrier lifetime can be greatly influenced by width of QWs and indium concentration [4.9, 4.10, 4.13, 4.14]. Specifically, two-step PL decay was observed with the early fast and later slow decay processes being attributed to carrier transfer from weakly to strongly localized states and recombination of carriers in strong localized states, respectively [4.15].

In this subsection, using time-resolved pump-probe differential PL, we have directly measured the fast decay time constants of the photogenerated carriers in the range of

1.41-2.22 ns, which is attributed to the lifetime of carriers in QWs. Moreover, the time constant of extremely slow decay of dominant PL peak is identified as long as 570 ns, corresponding to the recombination of the carriers at localized states.

4. 2. 1. Sample description and experimental setups

In our studies, the sample, grown by metal-organic chemical vapor deposition, consists of four periods of InGaN/GaN QWs with 3 nm $In_{0.2}Ga_{0.8}N$ QWs sandwiched by 12-nm thick GaN barriers, respectively. The growth conditions of this sample are essentially the same as those outlined in Ref. [4.16]. A laser beam generated by Ti:sapphire regeneration amplifier with a pulse width of 180 fs and a repetition frequency of 250 kHz was frequency-doubled by a BBO nonlinear crystal, see Fig. 4.1. As a result, such an amplifier system produced a train of the pulses at 393 nm. The radiation beam was split into two parts labeled by us as pump and probe, having relatively high and low powers, respectively. The probe beam passed through a chopper whereas the pump beam was sent through a delay line to vary the temporal delay for probe pulses relative to pump pulses. Since the probe beam was modulated, one can measure the PL intensity generated by the probe beam through locking into the modulated frequency via a lock-in amplifier. The PL signal is focused into a spectrometer and then detected by a photomultiplier tube. The sample is mounted in a cryostat cavity of which the temperature can be varied from 4.2 K to 300 K.

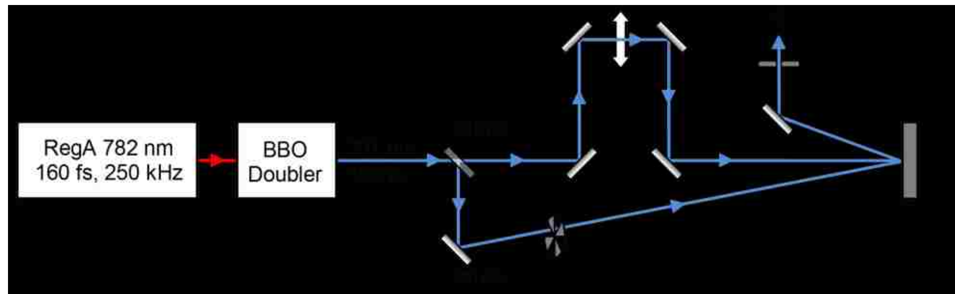

Fig. 4.1. An experimental setup for pump-probe differential PL.

4. 2. 2. PL as function of laser intensity and temperature

Fig. 4.2 illustrates PL spectra measured at 5 K under different excitation power densities. The main peak (P_L) is located at 2.575 eV at an excitation power density of 0.5 W/cm^2. The multiple peaks on the low energy side are LO-phonon replica [4.17]. When the excitation intensity is increased, a shoulder (P_H) on the high energy side appears, which suggests the presence of one peak or multiple ones. Multiple peaks in InGaN/GaN were widely observed and attributed to splitting of valence band [4.18], different quantum states [4.19], and weak-strong localized states [4.20]. Using one-dimensional Schrödinger-Poisson solver, the energy of the lowest QW transition (i.e. e1-hh1) is calculated to be 2.741 eV at 5 K when the pump intensity is set as 30 W/cm^2. The calculated transition energy is higher than that of the dominant peak in Fig. 4.2 by about 140 meV but only lower than that of the broad shoulder on the high-energy side by about 10 meV. As analyzed below, the main peak and shoulder are caused by the recombination of the carriers at localized states and extended states, respectively [4.21].

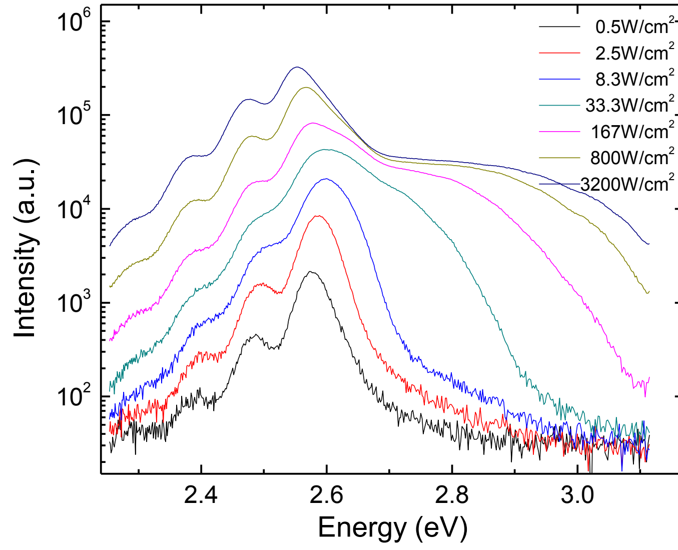

Fig. 4.2. Excitation power density dependent PL spectra for InGaN QWs measured at 5 K.

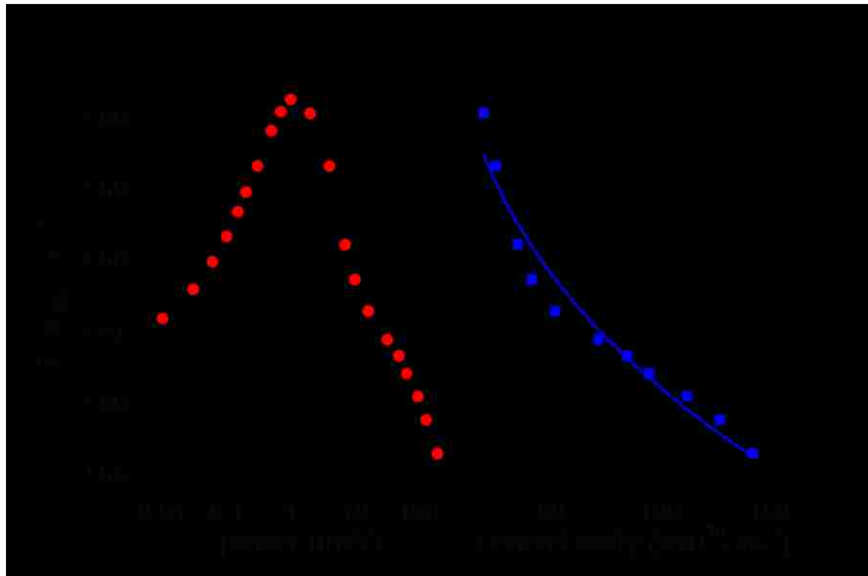

Fig. 4.3. (a) The emission energy of PL vs excitation power density measure at 5 K. (b) The emission energy of PL vs carrier density for excitation power density higher than 16.7 W/cm^2. The solid curve is a fit based on band gap renormalization effect.

Fig. 4.3(a) shows the behavior of emission energy of P_L versus excitation density. A blue shift in the amount of 30 meV is observed when the excitation density is increased from 170 mW/cm^2 to 16.7 W/cm^2. As excitation density is further increased up to 3200 W/cm^2, the P_L exhibits a red shift in the amount as large as 49 meV. Previously, the blue shift was frequently observed and explained by the combination of band-tail filling effect and reverse quantum confine Stark effect (QCSE) as the carrier density in QWs is increased [4.22-4.24]. However, the anomalously large red shift has not been observed yet in InGaN/GaN QWs. To understand the origin for such red shift, we plot the peak energy of P_L (only red shift part) versus carrier density, as shown in Fig. 4.3(b). Since the thickness of QWs is much less than a typical absorption depth of the excitation, we can assume spatially homogeneous excitation of well layers. In such case, the photogenerated carrier density can be determined as $n = \alpha J/(h\nu S)$, where α is absorption coefficient, J is energy per pulse, $h\nu$ is the incident photon energy, and S is the focus area of incident laser. Under very high laser intensities, the absorption efficient could be reduced due to band-filling effect. Thus we calculate the carrier intensity at high excitation powers by $n = n_0 I/I_0$, where I and I_0 are integrated PL signals at high and low excitation powers, respectively. The peak energy as a function of carrier density can be well fit via an expression of band-renormalization effect, $E = E_0 - cn^{1/3}$, see Fig. 4.3(b). The fitting value of C is obtained as 1.66×10^{-8} eV cm, which is very close to that in Ref. [4.25]. Therefore, such a red shift is likely the manifestation of band-gap renormalization.

The peak energy of P_L is plotted as a function of temperature measured at 16.7 W/cm^2, see Fig. 4.4. A blue shift as large as 32.4 meV from 5 K to 120 K was observed.

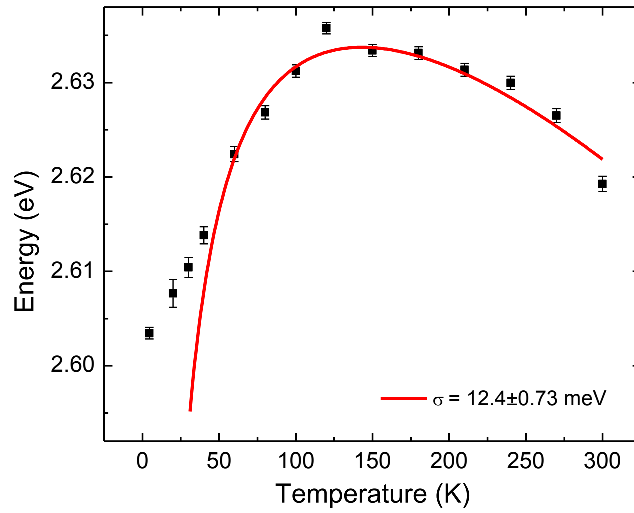

Fig. 4.4. The emission energy of PL vs temperature measured at 16.7 W/cm^2. The solid curve is a fit based on band tail model.

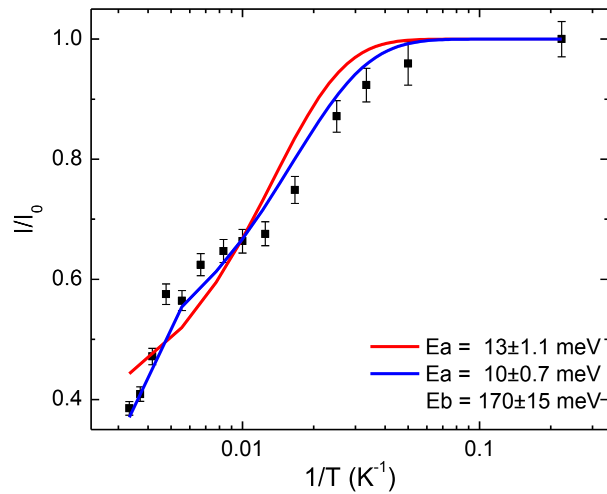

Fig. 4.5. Normalized integrated PL intensity as s function of 1/T for InGaN QWs measured at 16.7 W/cm^2. The red and blue curves are single and two channels Arrhenius fits respectively. Ea and Eb stand for the activation energy.

The increase of the peak energy with temperature in InGaN QWs is considered as an indication of emission from localized states [4.26]. Such temperature-dependent emission energy at localized states can be described as

$$E(T) = E(0) - \frac{\alpha T^2}{T + \beta} - \frac{\sigma^2}{k_B T} \tag{4-1}$$

Where, *E(0)* is the energy gap at zero temperature, α and β are Varshini's parameters, σ indicates the degree of the localization effect, and k_B is Boltzmann constant. Using this formula to fit the data, see Fig. 4.4, we obtained σ to be 12.4 meV, which is consistent with that in Ref. [4.27]. Therefore, we have attributed the main peak in PL spectra to the recombination of carriers occupying localized states. To further verify the carrier localization, both single and two-channel Arrhenius equations [4.28] were used to fit temperature-dependent PL intensities, see red and blue curves of Fig. 4.5, respectively. The activation energy is determined to be 13 meV in the single-channel fit which is quite close to the value of σ. Since this activation energy is much less than the QW band offsets, the thermal quenching originates from thermionic emission of carriers out of potential minima caused by localized states rather than the thermal activation of electrons and holes out of InGaN QWs. The two-channel Arrhenius equation provides a better fit, especially at high temperature, which could be caused by the increase in the intensity of P_H relative to that of P_L with increasing temperature. The activation energies obtained from such a fit are 11 meV and 169 meV, respectively. We tentatively attribute these energies to carrier confinement energy of localized states and thermal escape energy for the carriers moving out of QWs, respectively.

4. 2. 3. Pump-probe differential PL experiment

After we determine the carriers inside have fast and slow decay, we want to measure the PL spectra at different delay times for the pump beam. When the pump is turned on, the intensity of P_L is reduced dramatically whereas that of P_H increases, see Fig. 4.6 (a). The intensity of P_L does not recover even if we increase the delay time to 3.725 ns, which suggests that P_L has a very long lifetime, i.e. slow decay. Using a fast oscilloscope, we have measured the slow decay time constant of 570 ns, corresponding to lifetime of the carriers occupying localized states. On the other hand, the intensity of P_H increases obviously when the delay time is increased, which implies that P_H has a fast decay. Fig. 4.6 (b) is a plot of the differential ratio vs. delay time. The differential ratio can be expressed by $= 1 - I(t)/I_0$, where I_0 is the integrated PL intensity induced by the probe without the pump and $I(t)$ stands for that of the probe with the pump at a certain delay instant t. Considering that the slow decay has a much longer lifetime compared with the fast decay, a single exponential decay function is used to obtain the fast decay time as a function of the temperature. As a result, the decay time constants are determined to be 1.41-2.22 ns. Obviously, the fast decay time constan is more or less independent of temperature, which indicates that nonradiative recombination plays a minor role.

In conclusion, the emissions peaks from localized states and extended states have been observed on the InGaN/GaN QWs. By analyzing the dependence of the PL spectra on the excitation power, a red shift has been observed, due to band-gap renormalization. Moreover, through pump probe differential PL measurements, we confirm that the fast

decay originates from the lifetime of the carriers in extended states whereas the slow decay is the manifestation of the recombination of the carriers at localized states.

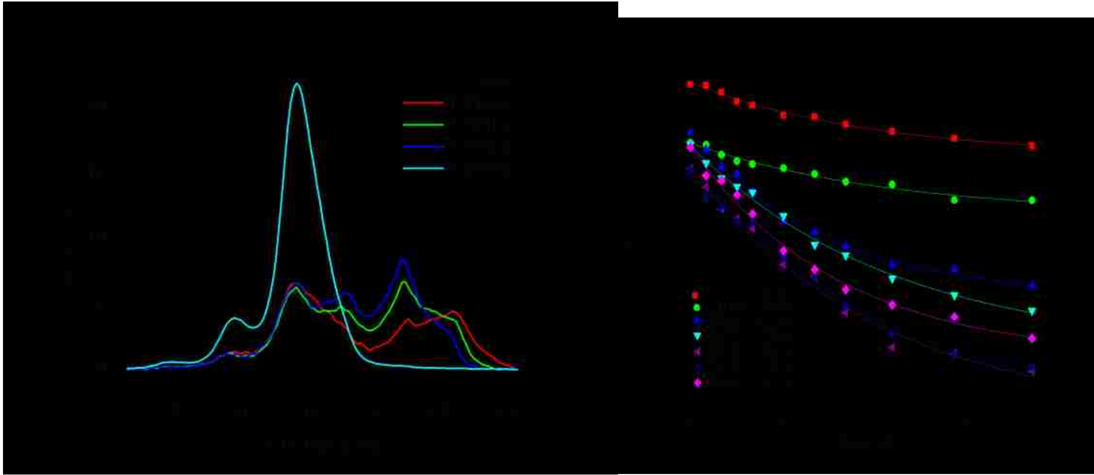

Fig. 4.6. (a) Pump-probe differential PL spectra at different delay times measured at 5 K. (b) Differential ratio vs. delay time measured at different temperatures. The solid curves are single exponential fits to experiment data.

4. 3. PL emission in deep ultraviolet region from GaN/AlN asymmetric-coupled QWs

GaN/AlN heterostructures have been widely studied for their promising applications in blue-violet light emitting diodes (LEDs) and laser diodes (LDs), due to the wide band gap of GaN (~3.5 eV) [4.29-4.32]. On the other hand, due to their large conduction band offset (~1.8 eV) and ultrafast intersubband relaxation time, GaN/AlN quantum wells

(QWs) and quantum dots (QDs) are also intensely explored to achieve high-speed intersubband (ISB) optoelectronic devices operating from 1.08 μm to 3 μm [4.33-4.36]. What makes GaN/AlN QWs unique is extremely high internal electric fields approaching 10 MV/cm due to spontaneous and piezoelectric polarizations when these structures are grown on (0001) substrate. Such large internal fields induce quantum confined Stark effect (QCSE) without applying an external electric field. Consequently, the overlap of electron and hole wave functions, transition energy and recombination rate of QWs are greatly reduced. Such strong internal fields can be exploited to enhance nonlinear-optical effects such as second-harmonic generation [4.37, 4.38] and quantum cascade detectors [4.39, 4.40], without applying any external field. However, when these QWs are grown on non-polar planes such as $(11\bar{2}0)$ instead of (0001) [4.41], the internal electric fields vanish.

In this subsection, we report our results on GaN/AlN asymmetric-coupled QWs. In the past, these heterostructures were primarily utilized in electroabsorption modulators and frequency doublers based on intersubband transitions [4.42]. However, band-to-band transitions in the GaN/AlN asymmetric-coupled QWs have not been investigated in details. As illustrated below, deep UV transition peaks with their photon energies up to 5.061 eV were observed. These transitions were caused by the recombination of electrons inside the AlN coupling barrier with the heavy holes in the GaN QWs. By using two wells to sandwich the coupling barrier, we have significantly increased the overlap between the wave functions of the electrons in the coupling barrier and heavy holes inside the two QWs. Besides, photoluminescence quenching has been observed when

increasing the temperature of these nanostructures. We believe such a behavior is caused by relocation of the photogenerated electrons from the AlN coupling barriers to GaN QWs under large built-in electric fields.

4. 3. 1. Sample description and experimental setups

Multiple GaN/AlN asymmetric-coupled QWs were grown in a low-pressure vertical VEECO P75 reactor with a high-speed rotation configuration. The reagents used during the growth were ammonia, trimethylgallium (TMGa), and trimethylaluminum (TMAl). High-purity hydrogen and nitrogen were used as the carrier gases. All the samples were grown on 2.5-μm-thick undoped (or n-) GaN templates being grown on c-plane sapphire substrates. Each GaN template was grown at 1070 ^{o}C, which employed a 30-nm-thick GaN nucleation layer deposited at 515 ^{o}C. The active layers of the AlN/GaN/AlN asymmetric-coupled QWs consist of 10 periods. For comparison, two additional samples were grown, each of which consists of multiple single GaN/AlN QWs. The structures of all four samples are summarized in Table 4-1. Both the AlN and GaN layers were grown at a temperature of 1070 ^{o}C, with growth rates being 3.6 nm/min and 4.5 nm/min, respectively. Each sample has a 10-nm-thick GaN layer as the cap on the top.

Photoluminescence (PL) spectra were measured by using a coherent UV beam at the wavelength tunable from 235 nm to 260 nm as the pump which is third harmonic output of a Ti: sapphire laser. Each pump beam consists of a train of pulses with the pulse width

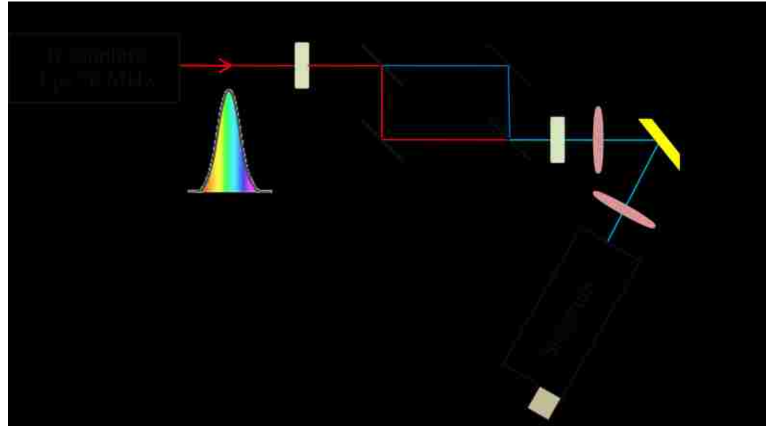

Fig. 4.7. The experiment setup for third harmonic output from Ti: sapphire oscillator.

of 3 ps. The highest average pump power used in our experiment is 20 mW. Each sample of multiple GaN/AlN asymmetric-coupled QWs was mounted on a cold finger of a cryostat with its temperature being stabilized and continuously varied in the range of 4.2-300 K.

4. 3. 2. Deep ultraviolet emission from GaN/AlN asymmetric QWs

For the asymmetric-coupled QWs, we have identified two apparent transition peaks in the PL spectrum, see Fig. 1. For sample #1, For example, the transition energies of the two peaks are deduced to be 3.938 eV (P_{low}) and 5.061 eV (P_{high}), respectively, see Table 4-1. When the widths of the two QWs are increased from 2 nm and 1.5 nm to 2.5 nm and 2 nm, respectively, the transition energies for the two peaks are reduced to 3.722 eV and 4.647 eV, respectively, due to the decreases inthe quantum-confinement energies. What

Table 4-1. Sample parameters. Here, dAlN, dGaN, stands for the thickness of AlN and GaN layer, respectively. E_{low}, stands for the lower-transition energy peak (or the only peak) of asymmetric-coupled (or single) QWs, while E_{high} stands for higher-transition energy peak of asymmetric-coupled QWs. I_{low}, I_{high} are relatively integration intensity of lower- and higher-transition energy peak, respectively. Label R stands for the ratio between the PL intensities of the higher- and lower-energy transition peaks.

Sample	d_{AlN} / d_{GaN} (nm)	E_{low} (eV)	E_{high} (eV)	I_{low} (a.u.)	I_{high} (a.u.)	R
1	4 / **2** / 1 / **1.5**	3.938	5.061	11.3	101	8.9
2	4 / **2.5** / 1 / **2**	3.722	4.647	7.3	121	16.6
3	4 / **1.5**	4.335	N/A	1	N/A	N/A
4	4 / **2**	4.145	N/A	1.9	N/A	N/A

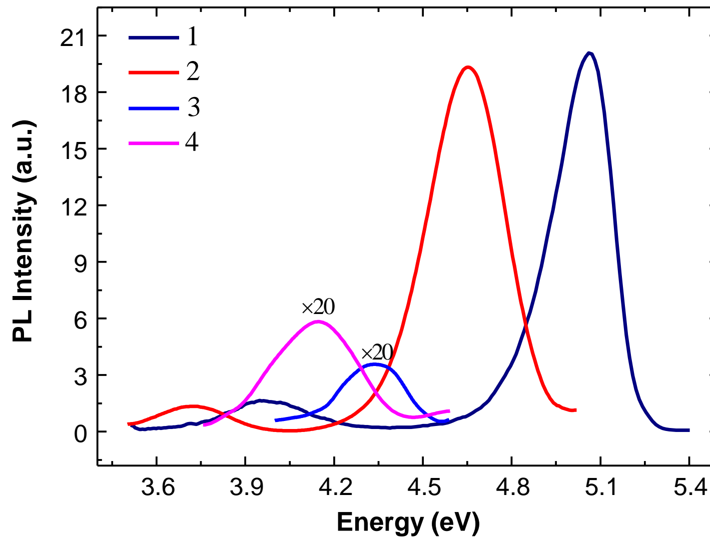

Fig. 4.8. PL spectra measured at 4.2 K on different samples at pump power of 6 mW at 235 nm. The signals of sample #3 and #4 are both multiplied by a factor of 20 for clarity.

is unique about the two PL spectra lies in transition peaks are much stronger than those for the lower-energy transitions. By decomposing each of the overall PL spectra into a

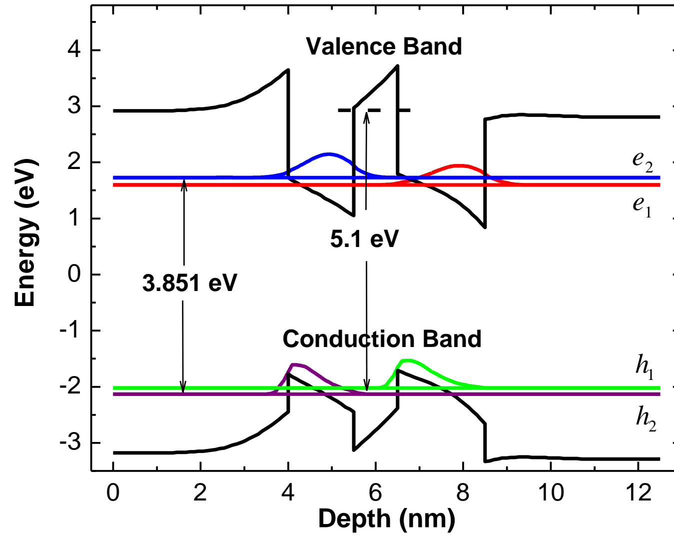

Fig. 4.9. Typical calculated band diagram of sample #1 using NEXTNANO3 8-band-k•p Schrödinger-Poisson solver.

linear superposition of the two transition peaks, we have deduced the ratio of the PL intensities for the higher- and lower-energy transition peaks to be 8.9 and 17 in Sample #1 and #2 respectively, which are anomalously large. Using nextnano3 8-band-**k·p** Schrödinger-Poisson solver [4.43, 4.44], we have plotted the energies of these states and their wave functions for Sample #1, see Fig. 4.8. One can see that the transition energies for e_1-hh_1 and e_2-hh_2 are both around 3.851 eV, which is very close to 3.938 eV deduced from Fig. 4.7. Taking into consideration that the full width at half maximum (FWHM) of peak at 3.938 eV is as high as 308 meV and the width of two quantum well are only 0.5 nm difference, we believe transitions for e_1-hh_1 and e_2-hh_2 merged into one peak at 3.938 eV. However, the confined energy states within the coupled QWs for both sample #1 and

#2 do not support the higher-energy transitions at 5.061 eV and 4.647 eV, deduced from our experiment. According to our calculations, these two energies are quite close to the transition energies for the electrons being localized inside the AlN coupling barrier and heavy holes at the two confined energy states in GaN QWs. Since the coupling barrier in the asymmetric-coupled QWs is rather thin, the overlap between the wave functions of the electrons inside the AlN coupling barrier and heavy holes inside the GaN QWs is large. Due to the presence of large built-in fields, the wave functions of the heavy holes have further penetrated into the AlN coupling barrier. As a result, the overlap between the wave functions of the electrons inside the AlN coupling barrier and heavy holes inside the GaN QWs has been further increased by the strong built-in fields. Thus, the signal of recombination of electrons inside AlN couple layer and holes in GaN wells could be stronger than that of electrons and holes in GaN QWs, which in fact is supported by our PL spectra. It is worth noting that the ratio of P_{high} over P_{low} is even larger for sample #2. Such a result is probably due to the fact that the wider QWs in sample #2 leads to a larger separation of electrons and holes inside the GaN QWs. This assumption is verified by our experimental result that the intensity of P_{low} in sample #2 is weaker than that for sample #1. Previously, recombination of the electrons inside an AlN wetting layer and heavy holes in the GaN quantum dot was used to explain the transition energy as high as 4.8 eV [4.45]. However, to the best of our knowledge, the transition energies of 5.061 eV and 4.647 eV have not been reported previously on GaN/AlN QWs. According to Fig. 4.7, each of the PL spectra for the single QWs consists of only a single peak at 4.335 eV and 4.145 eV for the two different well widths, respectively. These two energies are

significantly higher than those for the lower-energy transitions in the asymmetric-coupled QWs. The high energies are caused by the reduction in the quantum confinement by introducing the second QW in the asymmetric-coupled QWs and reduction of the coupling barrier width compared with the single QW. Moreover, based on Fig. 4.7, the PL intensities for the lower-energy transitions in the asymmetric-coupled QWs are stronger than those from the single QW by factors of 11 and 3.8, respectively. Furthermore, the PL intensities for the higher-energy transitions in the asymmetric-coupled QWs are higher than those from the single QW by factors as high as 101 and 63, respectively. Such huge enhancements are caused by the asymmetries of the coupled QWs, the presence of a thin isolating barrier, and large electric fields, which altogether result in significantly improved overlaps between the wave functions of the localized electrons and the heavy holes. Recently, type-II InGaN/GaNAs QWs were used to improve the overlap of wave function of electron and hole to achieve higher recombination efficiency comparing with conventional type-I InGaN/GaN [4.46]. For the higher-energy transition peak observed in our experiment, electrons are localized in the AlN barrier and holes are localized in the GaN wells. Our result illustrates that GaN/AlN coupled asymmetric QWs have a potential to realize high-efficiency deep UV optoelectronic devices.

As the sample temperature is increased from 4.2 K to 300 K, one can see from Fig. 4.9(a) that the integrated PL intensity for the 5.061-eV peak is decreased by a factor of 16 whereas that for the 3.938-eV peak is decreased only by a factor of 1.8. Using the relation of $I = I_0/[1+C\exp(-E_a/kT)]$ to fit the data for the 5.061-eV peak, the activation energy, E_a,

is obtained as 18 meV. Such a value implies that the 5.061-eV transition peak can only maintain a small amount of its original strength at room temperature, as illustrated by Fig. 4.9(a). However, within 4.2-100 K, the ratio of the PL intensities for the two peaks is slightly increased, see Fig. 4.9(b), which implies that most of the localized electrons inside the AlN coupling layer move back to the GaN QWs by thermal ionization when the temperature is higher than 100 K. Due to such a relocation, the PL intensity at 3.938 eV is expected to increase. In addition, the conduction band-edges for the GaN QWs become flattened since accumulated electron charges inside the QWs will screen the internal field. Therefore, the overlap of the wave functions of the electrons and heavy holes located inside the QWs is increased. These two factors have compensated for the significant decrease in the PL intensity typically expected for a PL peak. The flattened band-edges cause the transition peak at 3.938 eV to blue-shift, see Fig. 4.9(c), which is opposite to the reduction of the band-gaps through the temperature increase. Such blue-shift is consistent with the blue-shift of the 3.938-eV peak, as we increase the pump power (not shown here). In contrast, the transition peak at 5.061 eV is red-shifted, see Fig. 4.9(c), which is due to band gap reduction of AlN when increasing temperature. However, above 220 K and 280 K, the two transition peaks at 5.061 eV and 3.938 eV are blue- and red-shifted, respectively, which could be attributed to the increasing probability for the electrons to be scattered to the bound states inside each coupling barrier by the phonons following the absorption of the pump beam.

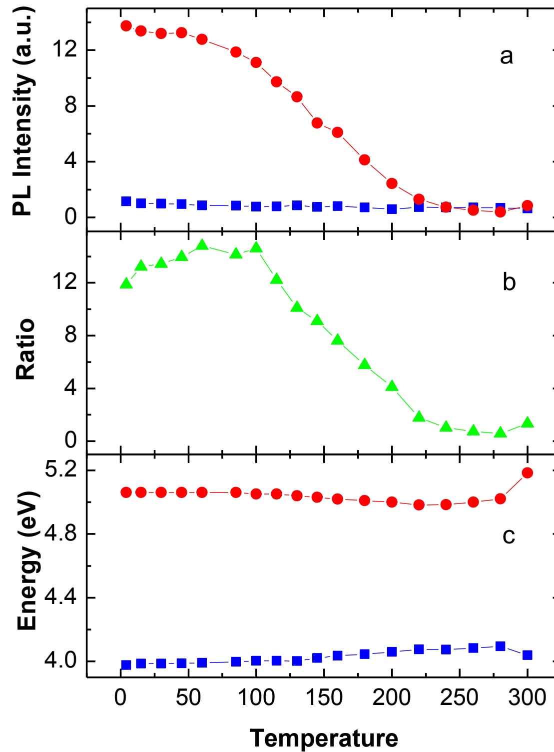

Fig. 4.10. (a) PL intensities vs. temperature. The dots correspond data of Phigh and the square correspond that of Plow. (b) Ratio of PL intensities determined from Fig. 4.8 vs. temperature; and (c) Transition energies of two PL peaks vs. temperature.

4. 4. PL induced by three-photon absorption in freestanding GaN

In this section, we will discuss some experiment results about anti-Stoke photoluminescence of GaN induced by three photon absorption. The sample is a 350-μm free-standing *n*-type GaN wafer was grown by MOCVD (sample sample we used for phonon-assisted anti-Stokes photoluminescence experiment). It was mounted on a cold

finger of a continuous-flow cryostat with its temperature being set anywhere from 4.2 K to 300 K. The sample was excited by 180-fs coherent pulses with their central wavelength being set to 782 nm and the repetition is 250 kHz.

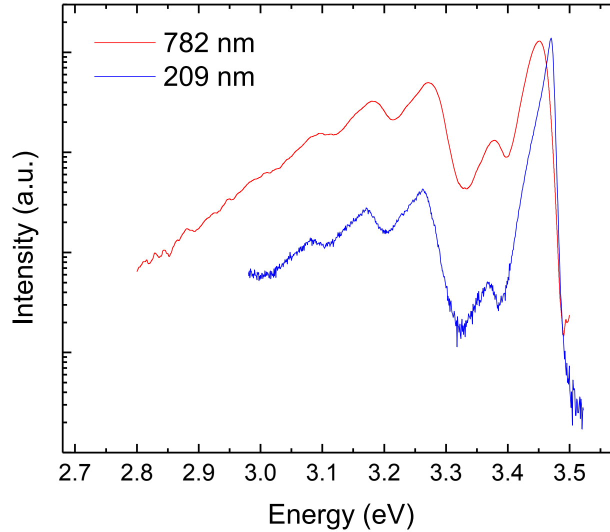

Fig. 4.11. Anti-Stokes and Stokes PL spectra measured at 4.2 K and under excitation wavelength of 782 nm and 209 nm.

We first measured the Stokes and anti-Stokes PL spectra at the excitation wavelength of 209 nm and 782 nm, respectively, see Fig.4.10. One can see one-to-one correspondence between each peak in the anti-Stokes PL spectrum and that in the Stokes PL spectrum except for the fact that the main peak of anti-Stokes PL peak is redshifted relative to the corresponding peak in the Stokes PL spectrum. Such redshift was estimated to be about 20 meV, based on the transition energies of the two respective I_2 peaks appearing in Fig. 4.10. It is caused by the higher reabsorption of PL on the high-

energy side than that on the low-energy side . The dominant peak in the anti-Stokes spectrum at 3.451 eV corresponds to the recombination of the excitons bound to neutral donors (D_0X or I_2). A small peak at 3.271 eV originates from the recombination of the donor–acceptor pairs (DAPs). whereas the two peaks at 3.180 eV and 3.096 eV is the 1LO-phonon and 2LO-phonon replica of the DAP peak at 3.271 eV. The small peaks near 3.370 eV are probably induced by the recombination between the electrons bound to the donors and free holes (D_0h).

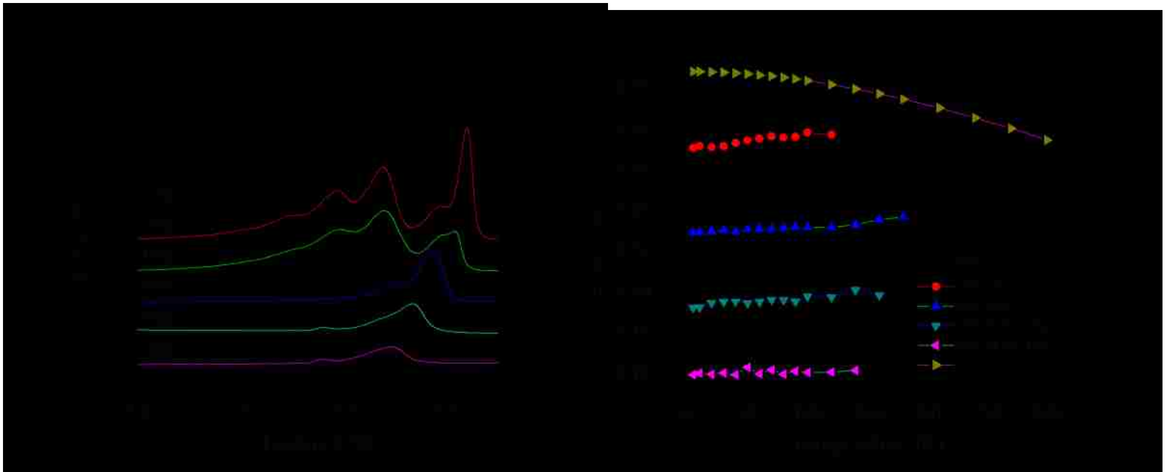

Fig. 4.12. (a) Anti-Stokes PL spectra at different temperature. (b) Photon energies of each peak at different temperature.

Fig. 4.11(a) shows anti-Stokes PL at different temperature. As we can observe, at room temperature, the exciton peak and DAP peak significantly overlap. Fig. 4.11(b) shows the peak energies as function of temperature after we decompose the peaks. The peak of I_2 significantly redshifts with temperature increases. However, the peak energy cannot be fitted by Varshini fitting due to the increase of redshift with temperature compared to stokes PL. Unlike peak of I_2, the other four peaks show the blueshift with

temperature. Such behavior confirms that the electrons or holes involved in these peaks are bounded to donor or acceptor. With temperature increases, the electron and hole will be excited to conduction and valence band by absorption of thermal energy. Thus these peaks gradually evolve to free electron and hole pairs of which the emission overlaps with main peak.

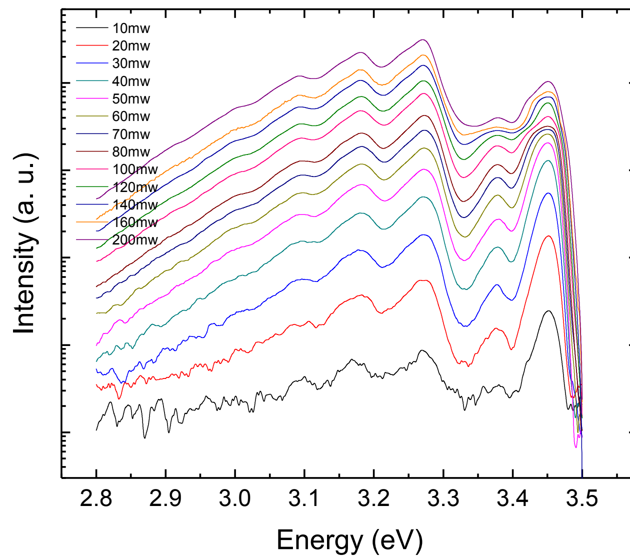

Fig. 4.13. Anti-Stokes PL spectra at different pump power measured at 4.2 K.

We also measure the anti-Stokes PL spectra as function of pump power. As is shown in Fig. 4.12, the intensity of DAP peak increases relative fast than that of I_2. Fig. 4.13(a) illustrates the dependence of the integrated PL intensity for the DAP peak at 3.271 eV on the pump power at 4.2 K. The dependence exhibits a cubic power law except for slight saturation at the higher pump powers. Therefore, the anti-Stokes DAP emission is

induced by three-photon absorption. The dominant three-photon absorption takes place when the electrons in the valence band are excited to the conduction band. Since the exciton transition energy is 3.472 eV, there is an extra energy of 1.285 eV, which is carried by the electrons in the conduction band and holes in the valence band as their kinetic energies. The photogenerated electrons and holes at these kinetic energies relax down to the bottom of the conduction band and the top of the valance band, respectively, primarily by emitting LO phonons. These electrons and holes then form excitons. Some of these excitons can be bound to the neutral donors. The electrons bound to acceptors can also relax down to the valence band by emitting LO phonons. Some of the photogenerated electrons can be also trapped at the donors, and subsequently jump down to the acceptors by losing photons, producing the DAP transition peak. The power dependence for the bound exciton transition significantly deviates from the cubic power law. Such strong saturation is caused by the limited density of the neutral donors. As the pump power becomes sufficiently high, almost all the neutral donors are used up for binding the excitons. Consequently, the density of the bound excitons approaches strong saturation. At room temperature, however, the dominant transition originates from the DAP recombination. The corresponding power dependence can be fitted by a cubic power law below the pump power of 158 mW, see Fig. 4.13(b). Above such a pump power, however, the power dependence severely deviates from the cubic power law. The electrons bound to donors and the holes bound to the acceptors take longer times to recombine as the separation between the corresponding donors and acceptors is increased. At room temperature, on average neutral donors and neutral acceptors are further

separated due to the thermal redistribution of the electrons and holes among the donors and acceptors since they have much higher kinetic energies. Therefore, due to the increase in the DAP recombination time, the saturation for the DAP transition peak can be much more severe. In comparison, at very low temperatures, the thermal redistribution of the electrons and holes among the donors and acceptors are minimized. Therefore, the saturation of the DAP emission rate is less affected, as shown by Fig. 4.13(a).

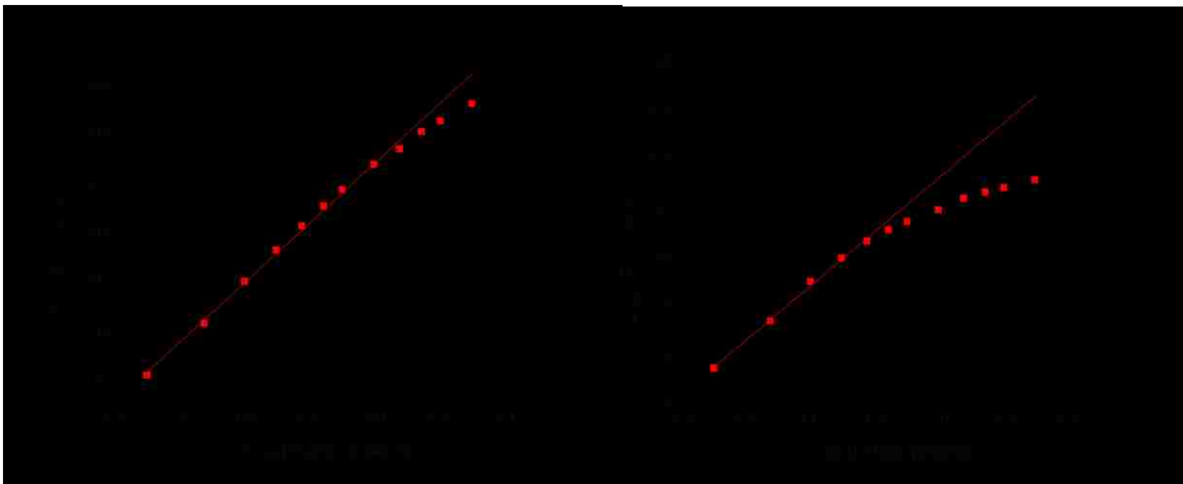

Fig. 4.14. (a) Intensity of DAP peak plotted vs. pump power in log scale at 4.2 K. Straight line corresponds to linear fit to data, resulting in a slope of 3.03. (b) Intensity of I2 peak plotted vs. pump power in log scale at 4.2 K. Straight line corresponds to linear fit to data, resulting in a slope of 2.75.

4. 5. PL induced by two-photon absorption in BN powder

To Hexagonal boron nitride (hBN) has been widely used as an electrical insulator and heat resistant material for several decades because it is chemically inert and

thermally stable. Recently the interest of hBN is renewed since the first observation of an intense deep ultraviolet exciton emission [4.47], which makes such material a potential candidate for optoelectronics devices. However, despite of many efforts in both experimental and theoretical studies, the optical property of hBN remains unclear.

Here, we report our results on investigating PL study of hBN powders using two-photon excitation. By energy-resolved excitation, we conclude that the impurity or defect energy level inside band gap of hBN plays an important role in such two-photon excited photoluminescence.

The sample studied by us was prepared from commercial hBN powders compact in a thin cylinder at a hydrostatic pressure of 8×10^{7} Pa. The purity of powders is high than 99.9% and particle size is in the range of 2 to 3 μm. The fourth or second harmonic output of a Ti: sapphire laser was used as pumps for one photon or two-photon excitation respectively, of which the pulse duration is around 150 fs and the repetition frequency is 76 MHz. The beam was focused on sample with a radius of 100 μm. The photoluminescence was collected to a single channel spectrometer and then detected by a photomultiplier.

The PL spectra of sample excited by 206.88 and 412.51 nm are presented in Fig. 4.14 as red and blue curves respectively. As we can see, the spectra are composed of two luminescence bands. Basically, one narrow band centered at 225 nm and one broad band between 250 to 400 nm are distinguished. The narrow peak was attributed to recombination of exciton bound to stack faults [4.48]. However, the peak position here is

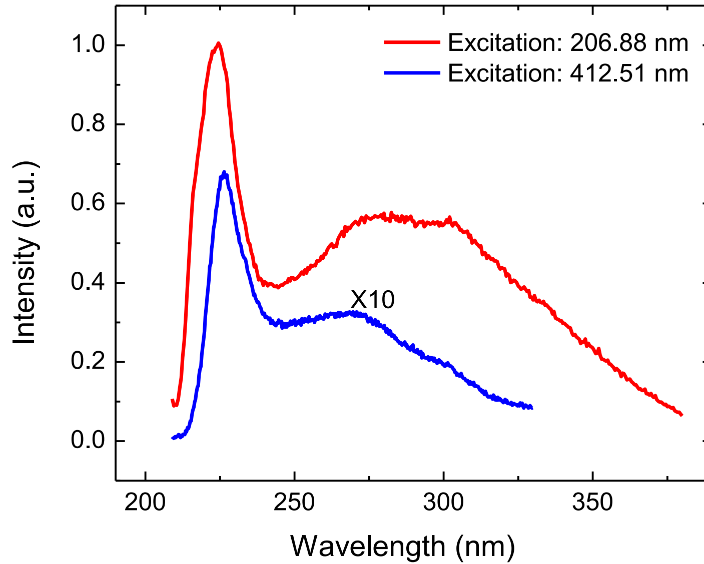

Fig. 4.15. PL spectra measured at room temperature. The pump power for 206.88 and 412.51 nm is 26 mW and 250 mW respectively.

not exactly located at 227 nm as published in other literatures. Such difference could be induced by superposition of multiple peaks in narrow band. A slight shoulder at 215 nm can be observed in our spectrum which is due to free exciton recombination, see red curve. Recently, the split of recombination energy of bound exciton or free exciton states was observed in pure hBN crystals which were explained by Jahn-Teller effect [4.49]. Thus, we claim that the narrow observed in our powder sample is mainly due to recombination of bound exciton. The broad peak, as pointed out in Ref. [4.50], was combination of deep donor-acceptor pairs (DAP) and impurity related transition. By controlling sampling quality and impurity level, such broad peak can be suppressed in pure hBN crystals.

When hBN powders are illuminated at 412.51 nm, both two bands were still observed. The narrow peak was located at same position compared with one photon excitation. However, the broad peak shifted to higher energy which could be induced by inefficient excitation of DAP with lower transition energy. To further investigate luminescence mechanism, we measured PL with photon energy range from 2.94 eV to 3.18 eV. As shown in Fig. 4.15(a), the integrated intensity of PL as a function of excitation photon energy exhibits a resonance peak at ~ 3 eV, Such resonance could be an indication that the midgap states play an important role in two-photon induced PL. Namely, when the excitation photon energy is resonant with the energy difference between midgap states with valence band or conduction band, the absorption will be increased dramatically. Similar phenomenon has been observed in multiple-photon absorption experiment in GaN [4.51]. These midgap states in BN could be originated from carbon or oxygen contents which commonly exist in hBN powders. Nitrogen or boron vacancy could also result in such energy states. Recent calculation using many-body perturbation theory points out that the substitution carbon impurity on the nitrogen sublattice, or the boron and nitrogen vacancy could induce midgap states [4.52], although the exact energy level is not consistent with our experiment.

We have studied pump power dependence of two-photon excited PL intensity, as shown in Fig. 4.15(b). For pump power below 250 mW, the data can be well fitted by square law which is consistent with two photon absorption. However, the deviation is observed when the pump power is further increased up to 470 mW. Such saturation effect

can be expected if midgap states play a role in the process of two-photon absorption since the concentration of purity or defect is limited in hBN.

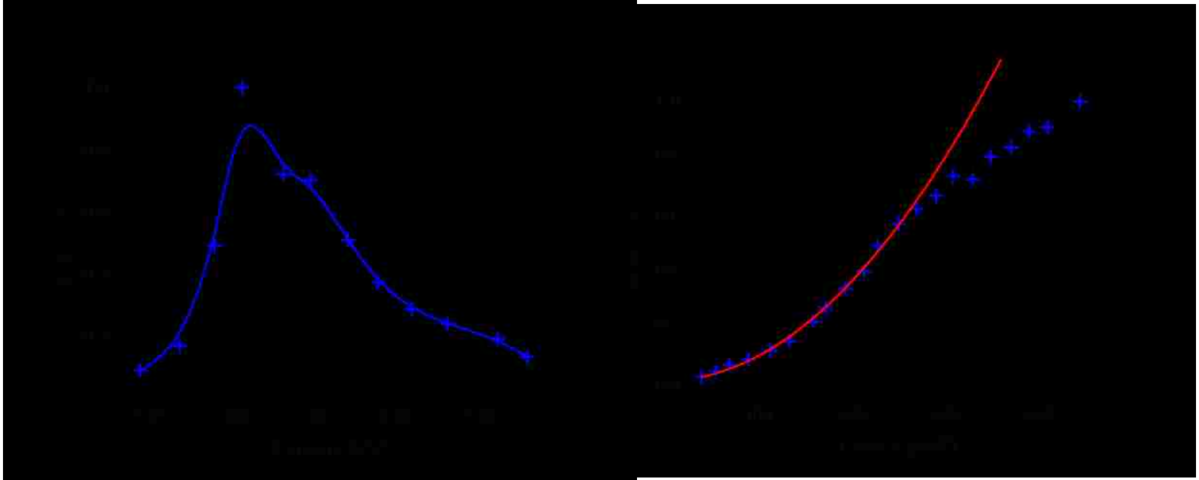

Fig. 4.16. (a) PL intensity as a function of excitation photon energy. The blue line is guide for eye. (b) PL intensity as a function of pump power. The cross corresponds to experiment data. The red curve is quadratic fit for first 12 points.

In conclusion of this section, we have measured two-photon excited photoluminescence in commercial hexagonal boron nitride powders. Through photon-energy resolved excitation, we find that the midgap states will enhance such two-photon absorption.

4. 6. Summary

To give a short summary for this chapter, we measure the PL signal from several InGaN/GaN and GaN/AlN QWs. For InGaN/GaN QWs, we have determined the emissions peaks from localized states and extended states have been observed on the InGaN/GaN QWs. Through pump probe differential PL measurements, we confirm that the fast decay originates from the lifetime of the carriers in extended states whereas the slow decay is the manifestation of the recombination of the carriers at localized states. For GaN/AlN asymmetric coupled QWs, we report the observation of deep ultraviolet photoluminescence peaks with their energies as high as 5.061 eV, which is attributed to the recombination of electrons in the AlN coupling barrier with heavy holes in the GaN QWs. Compared with the single QW, the PL intensity is significantly enhanced by as much as two orders of magnitude. When the sample temperature is increased, PL quenching is observed due to the relocation of electrons from the AlN coupling layer to the GaN quantum well. We also observed the multi-photon absorption induced photoluminescence in GaN thin film and BN powder.

Chapter 5. Transverse Nonlinear Generation in GaN/AlGaN Waveguide

5. 1. Introduction

Semiconductor materials, due to their large nonlinear coefficient, have been investigated for nonlinear generation for various applications including second harmonic generation [5.1], terahertz generation [5.2] and etc. Previously, semiconductor materials such as GaAs [5.1], GaSe [5.2], GaP [5.3], have been studied. On the contrary, the nonlinear behavior of GaN has not been well studied due to the fact that material's growth technology of GaN has only been mature less than twenty years. Although, compared to GaAs or $LiNbO_3$, the second order nonlinear coefficient of GaN is smaller, it is still much larger than some basic nonlinear optical crystals such as KDP, BBO, see Table 5-1. Moreover, GaN holds its special advantage compared to GaAs or $LiNbO_3$ due to its wider transparency window. Futhermore, due to recent progress of GaN based laser source, nonlinear device based on GaN can be easily integrated on single chip.

In the past, parametric conversion in transverse geometry has been studied in theory [5.4-5.6] and experiment [5.7-5.10] for its potential application as a source of entangle twin photons. The quasi-phase matching (QPM) is typically achieved by the use of alternating $Al_xGa_{1-x}As/Al_yGa_{1-y}As$ layers of which the preiod is well designed to compensate the wavevector of pump beam. Based on such structure, the conversion

efficiency of 10^{-11} and around 12000 generated pairs/second has been achieved [5.7], which is well suited for current standards in quantum-key distribution protocols.

It has been pointed out the signal-to-noise ratio (SNR) in these structures has been influenced by GaAs substrate [5.7]. Indeed, in order to generate twin photon pairs source around 1.55 um, the wavelength for pump laser should be around 775 nm. The photon energy of such pump is already larger than the bandgap of GaAs substrate which will result in spurious deep level emission, increasing the background noise. In this chapter we design a GaN/AlGaN based waveguide for transverse nonlinear generation to suppress interband direct absorption by utilizing its large bandgap.

Table 5-1. Second order nonlinear susceptibility and transparency window of several semiconductor and basic nonlinear optical materials.

Materials	d (pm/V)	λ (μm)
GaN	d_{33}= -16.7±1.3, d_{31}= 8.2±0.7	0.37-13.6
GaAs	d_{14}= 72	0.87-13
GaSe	d_{22}= 54±10.8	0.62-20
$LiNbO_3$	d_{33}= -27.2±1.3 d_{31}= -4.35±0.44	0.4-5.5
KDP	d_{36}= 0.39	0.174-1.57
BBO	d_{22}= 2.3, d_{31}= 0.16	0.189-3.5

5. 2. Design of GaN/AlGaN waveguide

Fig. 5.1 shows the geometry of GaN/AlGaN for transverse nonlinear generation. The pump laser will be illuminated on waveguide nearly along z-axis and its generated signal and idler will be propagated along y-axis. The wavelength of pump laser is set as 410 nm. In such case, the wavelength of counter propagated photon pair will be around 820 nm. The sample structure from top to bottom consists of: 30 × [$Al_{0.144}GaN$ (41.8 nm) / $Al_{0.593}GaN$ (45.1 nm)] / 3 × [GaN (81.1 nm) / $Al_{0.593}GaN$ (90.2 nm)] + GaN (81.1 nm) / 40 × [$Al_{0.593}GaN$ (45.1 nm) / $Al_{0.144}GaN$ (41.8 nm)] / GaN substrate, see Fig. 5.1 for sample scheme profile. The width and length for the waveguide are 6 um and 2 mm respectively. The top 30 and bottom 40 periods of $Al_{0.144}GaN$ (41.8 nm) / $Al_{0.593}GaN$ (45.1 nm) works as distributed Bragg reflector (DBR) mirrors, of which the thickness of each layer should be quarter of pump wavelength inside material. The 3.5-period GaN (81.1 nm) / $Al_{0.593}GaN$ (90.2 nm) performs as nonlinear generation layer which will meet the condition of quasi-phase match. The thickness of each layer should be half of the wavelength inside the multilayer structure. The ordinary and extraordinary refractive index of $Al_xGa_{1-x}N$ can be found elsewhere [5.11], which is shown in Fig. 5.2. Thus, the thickness of each layer can be determined.

The reflection of top 30 and bottom 40 periods of $Al_{0.144}GaN$ / $Al_{0.593}GaN$ DBR have been simulated by Rsoft. The dispersion of the material has been considered. As is illustrated in Fig 5.3, the refection of top and bottom DBR are 92% and 99%, respectively. The reflection window is around 20 nm and centered at 410 nm.

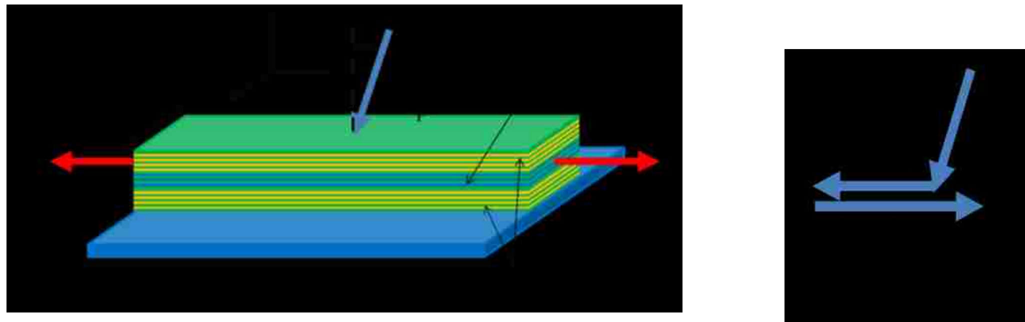

Fig. 5.1. (a) Scheme of GaN/AlGaN waveguide. QPM stands for quasi-phase match and DBR stands for distributed Bragg reflector. (b) Scheme of momentum conservation.

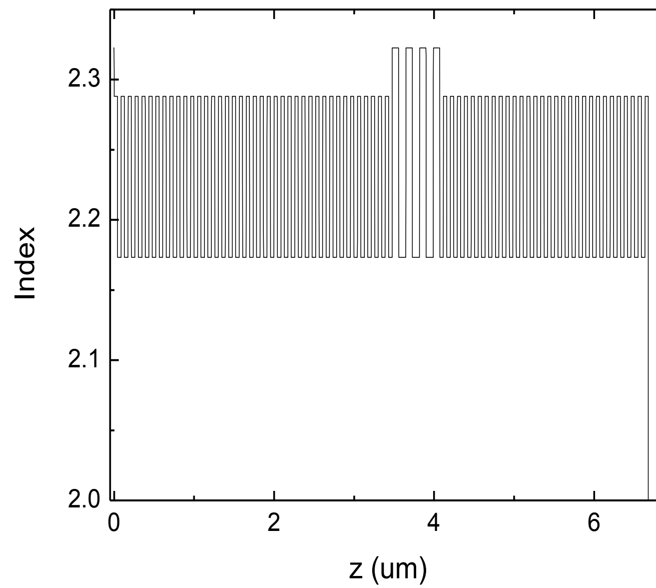

Fig. 5.2. Ordinary refractive index problem along z direction. The wavelength is chosen as 820 nm and polarization is along x direction.

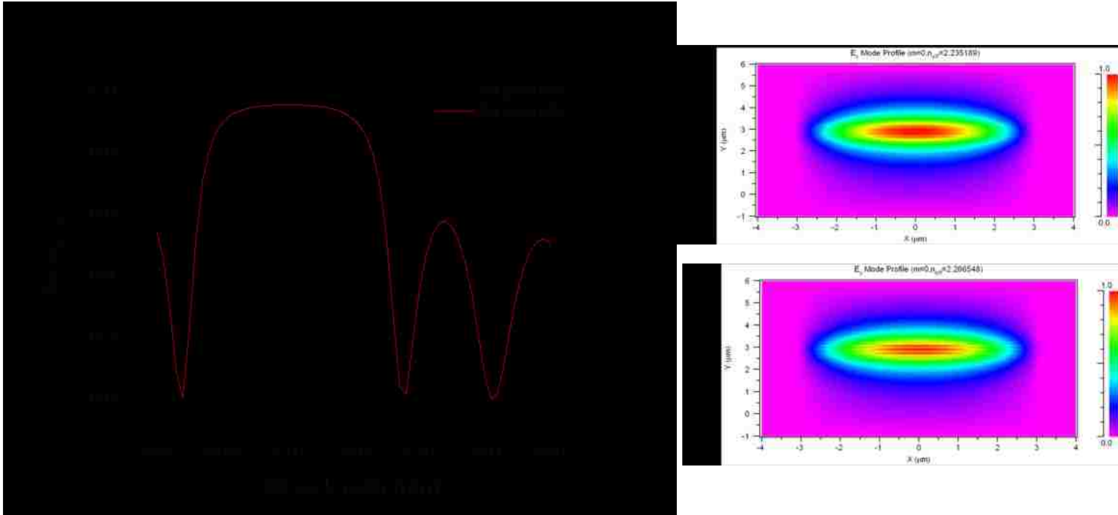

Fig. 5.3. (a) Reflection of top and bottom DBR. (b) Electric field amplitude profile of first TE mode. (c) Electric field amplitude profile of first TM mode.

Since the average index of QPM core layer is larger than the top and bottom DBR layer, guided mode of two counter propagated beam exits in such AlGaN waveguild which will effective confine the downconverted beams. Fig. 5.3(a) and (b) is a simulation using Rsoft. The polarization of TE mode is along x axis while that of TM mode is along z axis. The wavelength is chosen as 820 nm for both TE and TM mode.

Two phase-matched processes occur simultaneously in our sample: one where the signal is TE polarized and the idler is TM, and the other where the signal is TM and the idler is TE. In these two processes, the output spectra will be different mainly induced by birefringence of the wurtzite $Al_xGa_{1-x}N$. Considering the energy and momentum conservation, the center wavelength for signal and idler of such two processes can be determined by the following to equation set:

$$1/\lambda_p = 1/\lambda_s + 1/\lambda_i \quad (5\text{-}1)$$

$$\sin\theta/\lambda_p = n_{TM}(\lambda_i)/\lambda_i - n_{TE}(\lambda_s)/\lambda_s$$

or:

$$1/\lambda_p = 1/\lambda_s + 1/\lambda_i \quad (5\text{-}2)$$

$$\sin\theta/\lambda_p = n_{TE}(\lambda_i)/\lambda_i - n_{TM}(\lambda_s)/\lambda_s$$

where n_{TM} and n_{TE} are effective indices for guided mode, which can be calculated by numerical simulation, see Fig. 5.4. The first equation of each set is required by energy conservation and the second is required by momentum conservation in y direction. The momentum of pump beam in z direction is compensated by QPM layer. Substituting the value of n_{TM} and n_{TE} into equation set (5-1) and (5-2) respectively, we can calculate the wavelengths of emitting photon pairs as function pump incident angle which are shown in Fig. 5.5.

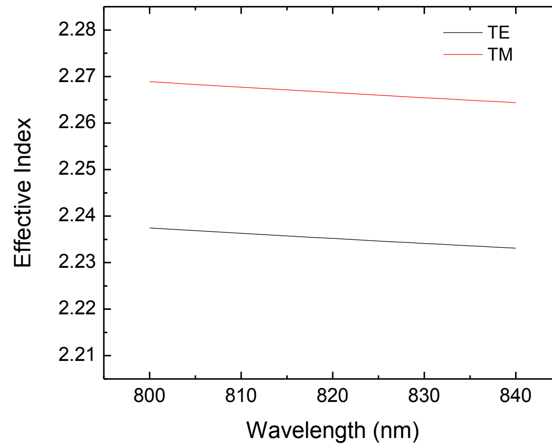

Fig. 5.4. Effective index of TE and TM mode in GaN/AlGaN waveguide from 800-840 nm.

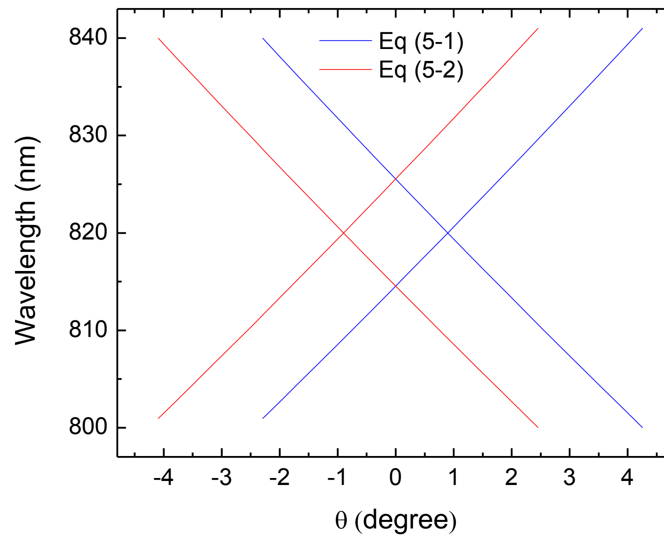

Fig. 5.5. Wavelength of generated photon pairs as function of pump laser angle. The angle is defined in Fig. 5.1 (a).

The designed structure of GaN/AlGaN waveguide can be used for nonlinear generation for different situation such as second harmonic generation [5.8], backward difference frequency generation or optical parametric amplification [5.4, 5.10], optical parametric oscillation [5.4] and optical parametric fluorescence [5.7].

5. 3. Surface emitting second harmonic generation

The first or easiest step to characterize the structure and see the enhancement induced by the cavity is to measure the surface emitting second harmonic generation, which is the reverse process of optical parametric fluorescence. In such condition, two

fundamental laser beams will be coupled into waveguide in counterpropagate direction. Very detailed calculation about such condition has been present already elsewhere [5.5]. Here we just simple use the equation in such reference to calculate the conversion efficiency in our experiment setups.

According to Ref. [5.5], the conversion efficiency for surface emitting second harmonic generation in such structure is determined by

$$\eta = \frac{2R_r}{1+R_r}[1-\exp(-a)][1-R_l R_r \exp(-a)] \tag{5-3}$$

Where, R_r and R_l are Fresnel reflection of right and left facets of waveguide. The parameter a is related to normalized pump power,

$$P_n = \frac{P}{P_s} \tag{5-4}$$

through following equation:

$$P_n = \frac{a[1-R_l R_r \exp(-a)]}{1+R_r \exp(-a)} \tag{5-5}$$

and the saturation power is given by

$$P_s = \frac{\lambda^2 n_\omega^{TE} n_\omega^{TM} n_{2\omega}(1-R_t R_b) W t_{eff}}{8\pi^2 \eta_0 (\Delta d)^2 L t} \tag{5-6}$$

where, λ is the laser of fundamental wave, n_{ω} and $n_{2\omega}$ is the refractive index of fundamental wave and second harmonic output. W, t, L are the width and thickness of the waveguide within which the two fundamental beams counter-propagate. η_0 is the vacuum impedance. t_{eff} is the spatial overlap (in the unit of length) among the spatially-modulated second-order nonlinear coefficient, the mode profiles for the two counterpropagate beams and spatial component of the second harmonic output electric field, which is defined by following equation:

$$t_{eff}{}^2 = \Delta d^2 / [\int d(z)\varphi_{TE}(z)\varphi_{TM}(z)\varphi_{SH}(z)dz]^2 \quad (5\text{-}7)$$

Obviously, the lower is the saturation power the more efficient is the frequency doubler. According to equation (5-6), P_s depends on the mirror reflectivity, R_t and R_b. Let us consider the generation of the 410 nm UV beam from the 820 nm Ti:sapphire laser. Based on our simulation, the value of R_t and R_b are 0.92 and 0.99 respectively. The second-order optical susceptibility element d_{xzx} provides the nonlinear coefficient for frequency doubling. This coefficient requires that the two pump and UV beams have the polarizations parallel to z, x, and x. According to Ref. [5.12], the difference between the nonlinear coefficients of the $Al_{0.593}GaN$ and GaN is calculated to be Δd = 3.3 pm/V. Substitute W = 6 um, L = 2mm, t_{eff}/t = 10, $R_r = R_l$ = 0.15, the saturation power is determined to be P_s = 68 kW.

Now, considering the laser used in this experiment is a Ti: sapphire laser of which, the average total power is up to 1 W. Thus, the average of each beam is around 500 mW. Assuming the pulse width is 10 ps and repetition frequency is 80 MHz, the peak power is

1.25 kW. In such case, the parameter *a* calculated by equation (5-4) and (5-5) is determined to be around 0.0217. Thus, the conversion efficiency can be determined through equation (5-3) to be 0.6%. The average output thus is around 3 mW which can be very easy to be observed.

5. 4. Summary and future outlook

In this chapter, we have designed a GaN/AlGaN multilayer waveguide for nonlinear generation, which can be used for surface emitting second harmonic generation, backward difference frequency generation, and parametric fluorescence down conversion. The conversion efficiency for surface emitting second harmonic generation has been calculated as an example. The future work should be focused on fabricating a real sample for various experiments.

Chapter 6. Summary and Future Outlook

In this chapter, we will briefly summarize the results achieved in this thesis and recommend several directions to continue the research on novel optical study and application on III-Nitride materials.

We first present how we can utilize the broadband THz generation in InGaN/GaN heterostructures in chapter 2. In experiments we have observed submicrowatt THz emitting from an 8-period $In_{0.25}GaN$/GaN QWs. If considering the thickness of sample and the power of laser we used, the generation efficiency of InGaN/GaN QWs is one of the highest. Through study THz output as a function of incident angle, polarization angle of laser and azimuthal angle of sample, the generation is attributed to diople radiation induced by internal field of InGaN/GaN heterostructure. The correlation behavior between THz and PL is also consistent with dipole ridation as generation mechanism. The calculated power of 8-period $In_{0.25}GaN$/GaN QWs based on diople is higher than we get from the experiment for around 60 times. The reason could be collection and coupling loss. In principle, we could further increase the THz output power for 100 times by narrowing the laser pulse width, increase the period number of InGaN QWs until the laser is fully absorbed, and increase the pump power. The saturation of the THz output power is expected and observed in experiment due to the screening effect of photogenerated carriers. By using a capacity model, we can estimate the total power per

area stored inside InGaN/GaN QWs. Such model also reveals the high THz generation efficiency is attributed to the extreme high electric field which is up to MV/cm. In the end of chapter 2, we study the THz generation in InGaN/GaN dot-in-a-wire nanostructures. By adding external reverse field on InGaN/GaN dot-in-a-wire LED structure, the THz output power is increased more than 4 times.

If the project is continued in future, we should optimize the structure of InGaN/GaN QWs to scale up absolute THz output power. Due to its unique 3D nanostructures, the novel application of THz generation on InGaN/GaN dot-in-a-wire is also worthwhile to be further studied. For example, we should explore could we only use several or even on nanowire to generate THz beyond noise level of best THz detector. At last, we should never forget the THz is generated by the power stored inside InGaN/GaN heterostructures due to its extreme large built-in electric field. Other applications based on such capacitor model should be further explored.

In chapter 3, we present some primary results of phonon assisted anti-Stokes PL on freestanding GaN. Such experiment phenomena could be utilized for laser cooling. In experiment, we demonstrate that our anti-Stokes PL of GaN is due to phonon assisted absorption by measuring the power dependent and temperature dependent PL. For power dependence, unlike pump below 400 nm that PL qudratically depends on laser power, when pump 1-LO phonon energy below PL peak, the intensity is proportion to laser power. For temperature dependence, the phonon assisted anti-Stokes intensity is increased with temperature.

If this project is continued in future, we should not only focus on finding high quality GaN to pursue laser cooling effect but also provide detail theory study what is the limitation of laser cooling on GaN.

In chapter 4, we have outlined the PL experiment results on different III-Nitride materials. PL is a very powerful experimental method to study semiconductor materials from fundamental physical properties and novel applications. Indeed, although, III-Nitride already has wide application, there are still a lot of fundamental issues waiting to be clarified. For example, in such chapter, we have observed to slow and fast channel decay in InGaN/GaN QWs. In future, also we do not know what kind of project of III-Nitride will be studied, but we should keep in mind that PL is a powerful experiment method which could be used to clarify the mechanism.

In chapter 5, we have explored the nonlinear generation in III-Nitrides. Considering its larger transparency window and relative larger nonlinear coefficient, we believe nonlinear generation based on III-Nitrides is definitely worthwhile be investigated. Here, we designed a GaN/AlGaN multiple layer waveguide for transverse nonlinear generation. As an example, the conversion efficiency and output power of surface emitting second harmonic generation has been calculated. Such structure has potential application for quantum information and phase conjugation. In future, designed structure should be fabricated for various experiments such as surface emitting second harmonic generation, backward difference frequency generation and optical parametric fluorescence. The nonlinear generation on GaN is definitely worthwhile to be intensively further explored

At last, we want to emphasize that this thesis is based on an idea that since III-Nitrides have been and will be continuously intensively studied for application of light emitting devices and high electron mobility transistors, we should seek various novel applications by taking advantage of the foresee mature III-Nitrides technology.

Reference

[1.1] J. Wu, "When group-III nitrides go infrared: New properties and perspectives", J. Appl. Phys. **106**, 011101 (2009).

[1.2] S. Nakamura, M. Senoh, and T. Mukai, "P-GaN/N-InGaN/N-GaN Double-Heterostructure Blue-Light-Emitting Diodes", Jpn. J. Appl. Phys. **32**, L8 (1993).

[1.3] S. Nakamura, M. Senoh, and T. Mukai, "High power InGaN/GaN double‐heterostructure violet light emitting diodes", Appl. Phys. Lett. **62**, 2390 (1993).

[1.4] S. Nakamura, T. Mukai, and M. Senoh, "Candela-class high‐brightness InGaN/AlGaN double-heterostructure blue-light-emitting diodes", Appl. Phys. Lett. **64**, 1687 (1994).

[1.5] S. Nakamura, M. Senoh, S. Nagahama, N. Iwasa, T. Yamada, T. Matsushita, Y. Sugimoto, and H. Kiyoku, "Room temperature continuous wave operation of InGaN multi-quantum-well structure laser diodes", Appl. Phys. Lett. **69**, 4056 (1996).

[1.6] P. Lefebvre, A. Norel, N. Gallart, T. Taliercio, J. Allegre, B. Gil, H. Mathieu, B. Damilano, N. Grandjean and J. Massies, "High internal electric field in a graded-

width InGaN/GaN quantum well: Accurate determination by time-resolved photoluminescence spectroscopy", Appl. Phys. Lett. **78,** 1252 (2001).

[1.7] F. Bernardini and V. Fiorentini, "Macroscopic polarization and band offsets at nitride heterojunctions", Phys. Rev. B 57, R9427 (1998).

[1.8] U. Mishra, P. Parikh and Y. F. Wu, "AlGaN/GaN HEMTs-an overview of device operation and applications", Proceeding of The IEEE **90**, 1022 (2002)

[1.9] K. Wang, J. Simon, N. Goel and D. Jena, "Optical study of hot electron transport in GaN: Signatures of the hot-phonon effectr", Appl. Phys. Lett. **88,** 022103 (2006).

[1.10] G. Xu, S. K. Tripathy, X. Mu, Y. J. Ding, K. Wang, Y. Cao, D. Jena and J. B. Khurgin, "Stokes and anti-Stokes resonant Raman scatterings from biased GaN/AlN heterostructure" , Appl. Phys. Lett. 93, 051912 (2008).

[2.1] M. Tonouchi, "Cutting-edge terahertz technology", Nature Photon. **1**, 97-105 (2007).

[2.2] B. Ferguson and X. -C. Zhang, "Materials for terahertz science and technology", Nature Mater. **1**, 26-33 (2002).

[2.3] R. Ascazubi, I, Wilke, K. Denniston, H. Lu and W. J. Schaff, "Terahertz emission by InN", Appl. Phys. Lett. **84,** 4810 (2004).

[2.4] X. Mu, Y. J. Ding, K. Wang, D. Jena and Y. B. Zotova, "Resonant terahertz generation from InN thin films", Opt. Lett. **32,** 1423 (2007).

[2.5] O. Imafuji, B. P. Singh, Y. Hirose, Y. Fukushima and S. Takigawa, "High power subterahertz electromagnetic wave radiation from GaN photoconductive switch", Appl. Phys. Lett. **91,** 071112 (2007).

[2.6] G. D. Metcalfe, H. Shen, M. Wraback, A. Hirai, F. Wu and J. S. Speck. "Enhanced terahertz radiation from high stacking fault density nonpolar GaN", Appl. Phys. Lett. **92,** 241106 (2008).

[2.7] A. E. Fatimy, N. Dyakonova, Y. Meziani, T, Otsuji, W. Knap, S. Vandenbrouk, K. madjour, D.Theron, C. Gaquiere, M. A. Poisson, S. Delage, P. Prystawko and C. Skierbiszewski, "AlGaN/GaN high electron mobility transistors as a voltage-tunable room temperature terahertz sources", J. Appl. Phys. **107,** 024504 (2010).

[2.8] T. Onishi, T. Tanigawa and S. Takigawa, "High power terahertz emission from a single gate AlGaN/GaN field effect transistor with periodic Ohmic contacts for plasmon coupling", Appl. Phys. Lett. **97,** 092117 (2010).

[2.9] V. D. Jovanović, D. Indjin, Z. Ikonic and P. Harrison, "Simulation and design of GaN/AlGaN far-infrared (λ~34μm) quantum-cascade laser", Appl. Phys. Lett. **84,** 2995 (2004).

[2.10] G. Sun, R. A. Soref and J. B. Khurgin, "Active region design of a terahertz GaN/$Al_{0.15}Ga_{0.85}N$ quantum cascade laser", Superlattices Microstruct. **37,** 107 (2005).

[2.11] J. T. Lu and J. C. Cao, "Terahertz generation and chaotic dynamics in GaN NDR diode", Semicond. Sci. Technol. **19,** 451 (2004).

[2.12] E. Alekseev and D. Pavlidis, "Large-signal microwave performance of GaN-based NDR diode oscillators", Solid-State Electron. **44,** 941 (2000).

[2.13] A. Hangleiter, F. Hitzel, S. Lahmann and U. Rossow, "Composition dependence of polarization fields in GaInN/GaN quantum wells", Appl. Phys. Lett. **83,** 1169 (2003).

[2.14] S. F. Chichibu, A. C. Abare, M. S. Minsky, S. Keller, S. B. Fleischer, J. E. Bowers, E. Hu, U. K. Mishra, L. A. Coldren, S. P. DenBaars and T. Sota, "Effective band gap inhomogeneity and piezoelectric field in InGaN/GaN multiquantum well structures", Appl. Phys. Lett. **73**, 2006(1998).

[2.15] P. Perlin, C. Kisielowski, V. Iota, B. A. Weinstein, L. Mattos, N. A. Shapiro1, J. Kruger, E. R. Weber and J. Yang, "InGaN/GaN quantum wells studied by high pressure, variable temperature, and excitation power spectroscopy", Appl. Phys. Lett. **73,** 2778 (1998).

[2.16] T. Wang, J. Bai, S. Sakai and J. K. Ho, "Investigation of the emission mechanism in InGaN/GaN-based light-emitting diodes", Appl. Phys. Lett. **78,** 2617 (2001).

[2.17] R. A. Arif, H. P. Zhao, Y. K. Ee and N. Tansu, "Spontaneous emission and characteristics of staggered InGaN quantum wells light emitting diodes", IEEE J. Quantum Electron. **44,** 573 (2008).

[2.18] H. Zhao, R. A. Arif and N. Tansu, "Design analysis of staggered InGaN quantum wells light-emitting diodes at 500-540 nm", IEEE J. Sel. Topics Quantum Electron. **15**, 1104 (2009).

[2.19] Website: http://www.ece.lehigh.edu/~tansu/

[2.20] H. Ahn, Y. P. Ku, C. H. Chuang, C. L. Pan, H. W. Lin, Y. L. Hong and S. Gwo, "Intense terahertz emission from a-plane InN surface", Appl. Phys. Lett. **92**, 102103 (2008).

[2.21] G. Xu, Y. J. Ding, H. Zhao, G. Liu, M. Jamil, N. Tansu, I. B. Zotova, C. E. Stutz, D. E. Diggs, N. Fernelius, F. K. Hopkins, C. S. Gallinat, G. Koblmüller and J. S. Speck, "THz generation from InN films due to destructive interference between optical rectification and photocurrent surge", Semicond. Sci. Technol. **25**, 015004 (2010).

[2.22] D. Turchinovich, P. U. Jepsen, B. S. Monozon, M. Koch, S. Lahmann, U. Rossow, A. Hangleite, "Ultrafast polarization dynamics in biased quantum wells under strong femtosecond optical excitation", Phys. Rev. B **68**, 241307 (2003).

[2.23] D. A. B. Miller, D. S. Chemla, T. C. Damen, A. C. Gossard, W. Wiegmann, T. H. Wood and C. A. Burrus, "Band-Edge Electroabsorption in Quantum Well

Structures: The Quantum-Confined Stark Effect", Phys. Rev. Lett. **53**, 2173 (1984).

[2.24] D. Turchinovich, B. S. Monozon, P. U. Jepsen, "Role of dynamical screening in excitation kinetics of biased quantum wells: Nonlinear absorption and ultrabroadband terahertz emission", J. Appl. Phys. **99,** 013510 (2006).

[2.25] P. J. S. van Capel, D. Turchinovich, H. P. Porte, S. Lahmann, U. Rossow, A. Hangleiter, and J. I. Dijkhuis, "Correlated terahertz acoustic and electromagnetic emission in dynamically screened InGaN/GaN quantum wells", Phys. Rev. B. **84,** 085371 (2011).

[2.26] S. Chichibu, T. Azuhata, T. Sota, and S. Nakamura, "Spontaneous emission of localized excitons in InGaN single and multiquantum well structures", Appl. Phys. Lett. **69,** 4188 (1996).

[2.27] Yong-Hoon Cho, G. H. Gainer, A. J. Fischer, J. J. Song, S. Keller, U. K. Mishra, and S. P. DenBaars, "S-shaped Temperature-dependent emission shift and carrier dynamics in InGaN/GaN multiple quantum wells", Appl. Phys. Lett. **73,** 1370 (1998).

[2.28] H. Schömig, S. Halm, A. Forchel, and G. Bacher, J. Off and F. Scholz, "Probing individual localization centers in an InGaN/GaN quantum well", Phys. Rev. Lett. **92,** 106802 (2004).

[2.29] K. Kazlauskas, G. Tamulaitis, J. Mickevičius, E. Kuokštis, A. Žukauskas, Yung-Chen Cheng, Hsiang-Cheng Wang, Chi-Feng Huang, and C. C. Yang, "Excitation power dynamics of photoluminescence in InGaN/GaN quantum wells with enhanced carrier localization", J. Appl. Phys. **97,** 013525 (2004).

[2.30] G. Sun, G. Xu, Y. J. Ding, H. Zhao, G. Liu, J. Zhang, and N. Tansu, "Investigation of fast and slow decays in InGaN/GaN quantum wells," Appl. Phys. Lett. **99,** 081104 (2011).

[2.31] G. Xu, G. Sun, Y. J. Ding, I. B. Zotova, K. C. Mandal, A. Mertiri, G. Pabst, R. Roy and N. C. Fernelius, "Investigation of Terahertz Generation due to Unidirectional Diffusion of Carriers in Centrosymmetric GaTe Crystals," IEEE J. Sel. Topics Quantum Electron. **17,** 30 (2011).

[2.32] Y. Kawano and K. Ishibashi, "An on-chip near-field terahertz probe and detector", Nature Photon. **2,** 618 (2008).

[2.33] M. A. Seo, H. R. Park, M. Koo, S. D. J. Park, J. H. Kang, O. K. Suwal, S. S. Choi, P. C. M. Planken, G. S. Park, N. K. Park, Q. H. Park and D. S. Kim, "Terahertz field enhancement by a metallic nano slit operating beyond the skin-depth limit", Nature Photon. **3,** 152 (2009).

[2.34] H. Tanoto, J. H. Teng, Q. Y. Wu, M. Sun, Z. N. Chen, S. A. Maier, B. Wang, C. C. Chum, G. Y. Si, A. J. Danner and S. J. Chua, "Greatly enhanced continuous-

wave terahertz emission by nano-electrodes in a photoconductive photomixer", Nature. Photon. **6,** 121 (2012).

[2.35] B. Heshmat, H. Pahlevaninezhad, Y. Pang, M. Masnadi-Shirazi, R. B. Lewis, T. Tiedje, R. Gordon and T. E. Darcie, "Nanoplasmonic Terahertz Photoconductive Switch on GaAs", Nano. Lett. **12,** 6255 (2012).

[2.36] H. R. Park, Y. M. Bahk, Q. H. Park, D. S. Kim, M. M. Luis, F. J. Garc á-Vidal, J. Bravo-Abad, "Controlling Terahertz Radiation with Nanoscale Metal Barriers Embedded in Nano Slot Antennas", Acs Nano. 2011, **5,** 8340-8345.

[2.37] S. G. Park. K. H. Jin, M.Yi, J. C. Ye, J. Ahn and K. H. Jeong, "Enhancement of Terahertz Pulse Emission by Optical Nanoantenna", Acs Nano. **6,** 2026 (2012).

[2.38] S. J. Oh, J. Kang, I. Maeng, J. S. Suh, Y. M. Huh, S. Haam and J. H. Son, "Nanoparticle-enabled terahertz imaging for cancer diagnosis", Opt. Express **17,** 3469 (2009).

[2.39] L. Razzar, A. Toma, M. Shalaby, M. Clerici, R. P. Zaccaria, C. Liberale, S. Marras, I. A. I. Al-Naib, G. Das, F. De Angelis, M. Peccianti, A. Falqui, T. Ozaki, R. Morandotti and E. Di Fabrizo, "", Opt. Express **19,** 26088 (2011).

[2.40] S. A. Lo and T. E. Murphy, "Nanoporous silicon multilayers for terahertz filtering", Opt. Lett. **34,** 2921 (2009).

[2.41] E. A. Zibik, T. Grange, B. A. Carpenter, N. E. Porter, R. Ferreira, G. Bastard, D. Stehr, S. Winner, M. Helm, H. Y. Liu, M. S. Skolnick and L. R. Wilson, "Long lifetimes of quantum-dot intersublevel transitions in the terahertz range", Nature Mater. **8,** 803 (2009).

[2.42] J. F. Scott, H. J. Fan, S. Kawasaki, J. Banys, M. Ivanov, A. Krotkus, J. Macutkevic, R. Blinc, V. V. Laguta, P. Cevc, J. S. Liu and A. L. Kholkin, "Terahertz Emission from Tubular Pb(Zr,Ti)O_3 Nanostructures", Nano. Lett. **8,** 4404 (2008).

[2.43] D. K. Polyushkin, E. Hendry, E. K. Stone and W. L. Barne, "THz Generation from Plasmonic Nanoparticle Arrays", Nano. Lett. **11,** 4718 (2011).

[2.44] H. Ahn, Y. -P. Ku, Y. -C. Wang, C. -H. Chuang, S. Gwo and C. –L. Pang, "Terahertz emission from vertically aligned InN nanorod arrays", Appl. Phys. Lett. **91,** 132108 (2007).

[2.45] H. P. T. Nguyen, S. Zhang, K. Cui, X. Han, S. Fathololoumi, M. Couillard, G. A. Botton, Z. Mi, "p-Type Modulation Doped InGaN/GaN Dot-in-a-Wire White-Light-Emitting Diodes Monolithically Grown on Si(111)", Nano. Lett. **11,** 1919 (2010).

[2.46] S. Komiyama, "Single-Photon Detectors in the Terahertz Range", IEEE J. Sel. Topics. Quantum Electron. **17,** 54 (2011).

[2.47] L. Xu, X. -C. Zhang, D. H. Auston, B.Jalali, “Terahertz radiation from large aperture Si p-i-n diodes”, Appl. Phys. Lett. **59,** 3357 (1991).

[3.1] S. Chu, C. Cohen-Tannoudji and W. D. Philips, Nobel Prize in Physics 1997 for development of methods to cool and trap atoms with laser light.

[3.2] E. A. Cornell, W. Ketterle and C. E. Weiman, Nobel Prize in Physics 2001 for the achievement of Bose-Einstein condensation in dilute gases of alkali atoms, and for early fundamental studies of the properties of the condensates.

[3.3] P. Z. Pringsheim, “Zwei Bemerkungen über den Unterschied von Lumineszenz- und Temperaturstrahlung”, Z. Phys. A **57**, 739 (1929).

[3.4] M. Sheik-Bahae and R. I. Epstein, “Laser cooling of solids”, Laser & Photon. Rev. **3**, 67 (2009).

[3.5] S. Vavilov, “Some Remarks on the Stokes Law”, J. Phys. (Moscow), **9**, 68 (1945).

[3.6] S, Vavilov, “Photoluminescence and Thermodynamics,” J. Phys. (Moscow), **10**, 499 (1946).

[3.7] L. Landau, “On the Thermodynamics of Photoluminescence”, J. Phys. (Moscow), **10**, 503 (1946).

[3.8] T. Kushida and J. E. Geusic, “Optical refrigeration in Nddoped yttrium aluminum garnet”, Phys. Rev. Lett. **21**, 1172 (1968).

[3.9] R. I. Epstein, M. I. Buchwald, B. C. Edwards, T. R. Gosnell and C. E. Mungan, "Observation of Laser-Induced Fluorescent Cooling of a Solid", Nature **377**, 500 (1995).

[3.10] D. V. Seletskiy, S. D. Melgaard, S. Bigotta, A. Di Lieto, M.Tonelli and M. Sheik-Bahae, "Laser Cooling of Solids to Cryogenic Temperatures", Nature Photon. **4**, 161 (2010).

[3.11] M. Sheik-Bahae and R. I. Epstein, "Can laser light cool semiconductors", Phys. Rev. Lett. **92**, 247403 (2004).

[3.12] G. Rupper, N. H. Kwong, and R. Binder, "Large excitonic enhancement of optical refrigeration in semiconductors", Phys. Rev. Lett. **97**, 117401 (2006).

[3.13] G. Rupper, N. H. Kwong, and R. Binder, "Optical refrigeration of GaAs: theoretical study", Phys. Rev. B **76**, 245203 (2007).

[3.14] L. A. Rivlin and A. Zadernovsky, "Laser cooling of semiconductors", Opt. Commun. **139**, 219 (1997).

[3.15] J. B. Khurgin, "Surface plasmon-assisted laser cooling of solids", Phys. Rev. Lett. **98**, 177401 (2007).

[3.16] J. B. Khurgin, "Role of bandtail states in laser cooling of semiconductors", Phys. Rev. B **77**, 235206 (2008).

[3.17] J. B. Khurgin, “Band gap engineering for laser cooling of semiconductors”, J. Appl. Phys. **100**, 113116 (2006).

[3.18] S. Eshlaghi, W. Worthoff, A. D. Wieck and D. Suter, “Luminescence upconversion in GaAs quantum wells”, Phys. Rev. B **77**, 245317 (2008).

[3.19] B. Imangholi, M. P. Hasselbeck, M. Sheik-Bahae, R. I. Epstein and S. Kurtz, “Effects of epitaxial lift-off on interface recombination and laser cooling in GaInP/GaAs heterostructures”, Appl. Phys. Lett. **86**, 081104 (2005).

[3.20] H. Gauck, T. H. Gfroerer, M. J. Renn, E. A. Cornell and K. A. Bertness, “External radiative quantum efficiency of 96% from a GaAs/GaInP heterostructure”, Appl. Phys. A **64**, 143 (1997).

[3.21] J. Zhang, D. Li, R. Chen and Q. Xiong, “Laser cooling of a semiconductor by 40 kelvin”, Nature **493**, 504 (2013).

[3.22] Y. P. Rakovich, S. A. Filonovich, M. J. M. gomes, J. F. Donegan, D. V. Talapin, A. L. Rogach and A. Eychmuller, “Anti-Stokes Photoluminescence in II–VI Colloidal Nanocrystals”, Phys. Status Solidi B **229**, 449 (2002).

[3.23] M. J. Fernée, P. Jensen and H. Rubinszten-Dunlop, “Unconventional photoluminescence upconversion from PbS quantum dots”, Appl. Phys. Lett. **91**, 043112 (2007).

[3.24] J. M. Harbold and F. W. Wise, “Photoluminescence spectroscopy of PbSe nanocrystals”. Phys. Rev. B **76**, 125304 (2007).

[3.25] Wang, X. W. W. Yu, J. Zhang, J. Aldana, X. Peng and M. Xiao, “Photoluminescence upconversion in colloidal CdTe quantum dots”, Phys. Rev. B **68**, 125318 (2003).

[3.26] Y. P. Rakovich J. F. Donegan, M. I. Vasilevskiy and A. L. Rogach, Phys. Status Solidi A **206**, 2497 (2009).

[3.27] S. Adachi, P. Capper, S. Kasap and A. Willoughby, “Properties of Semiconductor Alloys: Group-IV, III-V and II-VI Semiconductors”, pp 130 (Wiley 2009).

[3.28] Y.-F. Wu, A. Saxler, M. Moore, R. P. Smith, S. T. Sheppard, P. M. Chavarkar, T. Wisleder, U. K. Mishra and P. Parikh, “30-W/mm GaN HEMTs by Field Plate Optimization”, IEEE Electron Device Lett. **25**, 117 (2004).

[3.29] F. A. Ponce and D. P. Bour, “Nitride-based semiconductors for blue and green light-emitting devices”, Nature **386**, 351 (1997).

[3.30] C. F. Li, Y. S. Huang, L. Malikova, and F. H. Pollak, “Temperature dependence of the energies and broadening parameters of the interband excitonic transitions in wurtzite GaN”, Phys. Rev. B **55**, 9521 (1997).

[3.31] Urbach, F. “The Long-Wavelength Edge of Photographic Sensitivity and of the Electronic Absorption of Solids”, Phy. Rev **92**, 1324 (1953).

[3.32] P. P. Paskov, P. O. Holtz, B. Monemar, J. M. Garcia, W. V. Schoenfeld and P. M. Petroff, “Photoluminescence up-conversion in InAs/GaAs self-assembled quantum dots”, Appl. Phys. Lett. **77**, 812 (2000).

[3.33] C. K. Sun, J. C. Liang, J. C. Wang, F. J. Kao, S. Keller, M. P. Mack, U. Mishra and S. P. DenBaars, “Two-photon absorption study of GaN”, Appl. Phys. Lett. **76**, 439 (2000).

[4.1] S. Nakamura, M. Senoh and T. Mukai, “High-power InGaN/GaN double-heterostructure violet light-emitting diodes”, Appl. Phys. Lett. **62**, 2390 (1993).

[4.2] A. Khan, K. Balakrishnan and T. Katona, “Ultraviolet light-emitting diodes based on group three nitrides”, Nature Photon. **2**, 77 (2008).

[4.3] M. Tchernycheva, L. Nevou, L. Doyennette, F. H. Julien, E. Warde, F. Guillot, E. Monroy, E. Bellet-Amalric, T. Remmele and M. Albrecht, “Systematic experimental and theoretical investigation of intersubband absorption in GaN／AlN quantum wells”Phys. Rev. B **73**. 125347 (2006).

[4.4] S. Nakamura, T. Mukai, and M. Senoh, “Candela-class high-brightness InGaN/AlGaN double-heterostructure blue-light-emitting diodes”, Appl. Phys. Lett. **64**, 1687 (1994).

[4.5] S. Nakamura, M. Senoh, S.-I. Nagahama, N. Iwasa, T. Yamada, T. Matsushita, Y. Sugimoto, and H. Kiyoku, “Room temperature continuous - wave operation of

InGaN multi‐quantum‐well structure laser diodes", Appl. Phys. Lett. **69**, 4056 (1996).

[4.6] T. M. Smeeton, M. J. Kappers, J. S. Barnard, M. E. Vickers and C. J. Humphreys, "Electron-beam-induced strain within InGaN quantum wells: False indium "cluster" detection in the transmission electron microscope", Appl. Phys. Lett. **83**, 5419 (2003).

[4.7] A. Hangleiter, F. Hitzel, C. Netzel, D. Fuhrmann, U. Rossow, G. Ade, and P. Hinze, "Suppression of Nonradiative Recombination by V-Shaped Pits in GaInN/GaN Quantum Wells Produces a Large Increase in the Light Emission Efficiency", Phys. Rev. Lett. **95**, 127402 (2005).

[4.8] Z. H. Wu, A. M. Fischer, F. A. Ponce, W. Lee, J. H. Ryou, J. Limb, D. Yoo, and R. D. Dupuis, "Effect of internal electrostatic fields in InGaN quantum wells on the properties of green light emitting diodes", Appl. Phys. Lett. **91**, 041915 (2007).

[4.9] H. P. Zhao, G. Y. Liu, X. H. Li, R. A. Arif, G. S. Huang, J. D. Poplawsky, S. Tafon Penn, V. Dierolf, and N. Tansu, IET Optoelectron. **3**, 283 (2009).

[4.10] H. Zhao, R. A. Arif, and N. Tansu, "Design Analysis of Staggered InGaN Quantum Wells Light-Emitting Diodes at 500–540 nm", IEEE J. Sel. Top. Quantum Electron. **15**, 1104 (2009).

[4.11] S. H. Park, J. Park, and E. Yoon, "Optical gain in InGaN/GaN quantum well structures with embedded AlGaN δ layer", Appl. Phys. Lett. 90, 023508 (2007).

[4.12] U. T. Schwarz, H. Braun, K. Kojima, Y. Kawakami, S. Nagahama, and T. Mukai, "interplay of built-in potential and piezoelectric field on carrier recombination in green light emitting InGaN quantum wells", Appl. Phys. Lett. **91**, 123503 (2007).

[4.13] M. S. Minsky, S. B. Fleischer, A. C. Abare, J. E. Bowers, E. L. Hu, S. Keller, and S. P. Denbaars, "Characterization of high-quality InGaN/GaN multiquantum wells with time-resolved photoluminescence", Appl. Phys. Lett. **72**, 1066 (1998).

[4.14] P. Lefebvre, A. Morel, M. Gallart, T. Taliercio, J. Allègre, B. Gil, H. Mathieu, B. Damilano, N. Grandjean, and J. Massies, "High internal electric field in a graded-width InGaN/GaN quantum well: Accurate determination by time-resolved photoluminescence spectroscopy", Appl. Phys. Lett. **78**, 1252 (2001).

[4.15] S. W. Feng, Y. C. Cheng, Y. Y. Chung, C. C. Yang, M. H. Mao, Y. S. Lin, K. J. Ma, and J. I. Chyi, "Multiple-component photoluminescence decay caused by carrier transport in InGaN/GaN multiple quantum wells with indium aggregation structures", Appl. Phys. Lett. **80**, 4375 (2002).

[4.16] X. Mu, Y. J. Ding, B. S. Ooi, and M. Hopkinson, "Investigation of carrier dynamics on InAs quantum dots embedded in InGaAs/GaAs quantum wells based on time-resolved pump and probe differential photoluminescence", Appl. Phys. Lett. **89**, 181924 (2006).

[4.17] H. Zhao, G. S. Huang, G. Liu, X. H. Li, J. D. Poplawsky, S. Tafon Penn, V. Dierolf, and N. Tansu, "Growths of staggered InGaN quantum wells light-emitting diodes emitting at 520–525 nm employing graded growth-temperature profile", Appl. Phys. Lett. 95, 061104 (2009).

[4.18] X. A. Cao, S. F. Leboeuf, L. B. Rowland, C. H. Yan, and H. Liu, "Temperature-dependent emission intensity and energy shift in InGaN/GaN multiple-quantum-well light-emitting diodes", Appl. Phys. Lett. **82**, 3614 (2003).

[4.19] Y. Song, D. Chen, L. Wang, H. Li, G. Xi, and Y. Jiang, "Splitting of valance subbands in the wurtzite c-plane InGaN/GaN quantum well structure", Appl. Phys. Lett. **93**, 161910 (2008).

[4.20] J. Li, S. Li, and J. Kang, "Quantized level transitions and modification in InGaN/GaN multiple quantum wells", Appl. Phys. Lett. **92**, 101929 (2008).

[4.21] Y. Sun, Y. H. Cho, E.-K. Suh, H. J. Lee, R. J. Choi, and Y. B. Hahn, "Carrier dynamics of high-efficiency green light emission in graded-indium-content InGaN/GaN quantum wells: An important role of effective carrier transfer", Appl. Phys. Lett. **84**, 49 (2004).

[4.22] G. Pozina, J. P. Bergman, B. Monemar, T. Takechi, H. Amano, and I. Akasaki, "Origin of multiple peak photoluminescence in InGaN/GaN multiple quantum wells", J. Appl. Phys. **88**, 2677 (2000).

[4.23] S. Chichibu, T. Azuhata, T. Sota, and S. Nakamura, "Spontaneous emission of localized excitons in InGaN single and multiquantum well structures", Appl. Phys. Lett. **69**, 4188 (1996).

[4.24] K. Kazlauskas, G. Tamulaitis, J. Mickevicius, E. Kuokstis, A. Zukauskas, Y. C. Cheng, H. C. Wang, C. F. Huang, and C. C. Yang, "Excitation power dynamics of photoluminescence in InGaN/GaN quantum wells with enhanced carrier localization", J. Appl. Phys. **97**, 013525 (2005).

[4.25] E. Kuokstis, J. W. Yang, G. Simin, M. Asif Khan, R. Gaska, and M. S. Shur, "Two mechanisms of blueshift of edge emission in InGaN-based epilayers and multiple quantum wells", Appl. Phys. Lett. **80**, 977 (2002).

[4.26] P. G. Eliseev, P. Perlin, J. Lee, and M. Osinski, " "Blue" temperature-induced shift and band-tail emission in InGaN-based light sources", Appl. Phys. Lett. **71**, 569 (1997).

[4.27] J. Bai, T. Wang, and S. Sakai, "Influence of the quantum-well thickness on the radiative recombination of InGaN/GaN quantum well structures", J. Appl. Phys. **88**, 4729 (2000).

[4.28] A. Yasan, R. McClintock, K. Mayes, D. H. Kim, P. Kung and M. Razeghi, "Photoluminescence study of AlGaN-based 280 nm ultraviolet light-emitting diodes", Appl. Phys. Lett. **83**, 4083 (2003).

[4.29] S. Nakamura, M. Senoh, S. Nagahama, N. Iwasa, T. Yamada, T. Matsushita, H. Kiyoku, and Y. Sugimoto, “InGaN-based multi-quantum-well-structure laser diodes”, Jpn. J. Appl. Phys., Suppl. **35**, L74 (1996).

[4.30] I. Akasaki, S. Sota, H. Sakai, T. Tanaka, M. Koike, and H. Amano, “Shortest wavelength semiconductor laser diode”, Electron. Lett. **32**, 1105 (1996).

[4.31] C. Adelmann, E. Sarigiannidou, D. Jalabert, Y. Hori, J.-L. Rouvière, B. Daudin, S. Fanget , C. Bru-Chevallier, T. Shibata and M. Tanaka, “Growth and optical properties of GaN/AlN quantum wells”, Appl. Phys. Lett. **82**, 4154 (2003).

[4.32] M. Furis, A. N. Cartwright, H. Wu, W. J. Schaff, “Room-temperature ultraviolet emission from GaN/AlN multiple-quantum-well heterostructures”, Appl. Phys. Lett. 83, 3486 (2003).

[4.33] C. Gmachl, H. M. Ng, S. N. G. Chu, and A. Y. Cho, “Intersubband absorption at $\lambda \sim 1.55 \mu m$ in well- and modulation-doped GaN/AlGaN multiple quantum wells with superlattice barriers”, Appl. Phys. Lett. **77**, 3722 (2000).

[4.34] K. Kishino, A. Kikuchi, H. Kanazava, and T. Tachibana, “Intersubband transition in (GaN)m/(AlN)n superlattices in the wavelength range from 1.08 to 1.61 μm”, Appl. Phys. Lett. **81**, 1234 (2002).

[4.35] N. Iizuka, K. Kaneko, and N. Suzuki, “Near-infrared intersubband absorption in GaN/AlN quantum wells grown by molecular beam epitaxy”, Appl. Phys. Lett. **81**, 1803 (2002).

[4.36] D. Hofstetter, S.-S. Schad, H. Wu, W. J. Schaff, and L. F. Eastman, “GaN/AlN-based quantum-well infrared photodetector for 1.55 μm”, Appl. Phys. Lett. **83**, 572 (2003).

[4.37] L. Nevou, M. Tchernycheva, F. Julien, M. Raybaut, A. Godard, E. Rosencher, F. Guillot and E. Monroy, “Intersubband resonant enhancement of second-harmonic generation in GaN/AlN quantum wells”, Appl. Phys. Lett. **89**, 151101 (2006).

[4.38] D. Hofstetter, E. Baumann, F. R. Giorgetta, F. Guillot, S. Leconte, and E. Monroy, “Optically nonlinear effects in intersubband transitions of GaN/AlN-based superlattice structures”, Appl. Phys. Lett. **91**, 131115 (2007).

[4.39] A. Vardi, G. Bahir, F. Guillot, C. Bougerol, E. Monroy, S. E. Schacham, M. Tchernycheva and F. H. Julien, “Near infrared quantum cascade detector in GaN/AlGaN/AlN heterostructures”, Appl. Phys. Lett. **92**, 011112 (2008).

[4.40] A. Vardi, N. Kheirodin, L. Nevou, H. Machhadani, L. Vivien, P. Crozat, M. Tchernycheva, R. Colombelli, F. H. Julien, F. Guillot, C. Bougerol, E. Monroy, S. Schacham and G. Bahir, “High-speed operation of GaN/AlGaN quantum cascade detectors at $\lambda \approx 1.55$ μm”, Appl. Phys. Lett. **93**, 193509 (2008).

[4.41] L. Zhou, R. Chandrasekaran, T. D. Moustakas, and D. J. Smith, “Structural characterization of non-polar (1120) and semi-polar (1126) GaN films grown on r-plane sapphire”, J. Cryst. Growth **310**, 2981 (2008).

[4.42] L. Nevou, N. Kheirodin, M. Tchernycheva, L. Meignien, P. Crozat, A. Lupu, E. Warde, F. H. Julien, G. Pozzovivo, S. Golka, G. Strasser, F. Guillot, E. Monroy, T. Remmele and M. Albrecht, "Short-wavelength intersubband electroabsorption modulation based on electron tunneling between GaN/AlN coupled quantum wells", Appl. Phys. Lett. **90**, 223511 (2007).

[4.43] Available on-line http://www.nextnano.de

[4.44] P. K. Kandaswamy, F. Guillot, E. Bellet-Amalric, E. Monroy, L. Nevou, M. Tchernycheva, A. Michon, F. H. Julien, E. Baumann, F. R. Giorgetta, D. Hofstetter, T. Remmele, M. Albrecht, S. Birner, and Le Si Dang, "GaN/AlN short-period superlattices for intersubband optoelectronics: A systematic study of their epitaxial growth, design, and performance", J. Appl. Phys. **104**, 093501 (2008).

[4.45] A. Vardi, N. Akopian, G. Bahir, L. Doyennette, M. Tchernycheva, L. Nevou, F. H. Julien, F. Guillot and E. Monroy, "Room temperature demonstration of GaN/AlN quantum dot intraband infrared photodetector at fiber-optics communication wavelength", Appl. Phys. Lett. **88**, 143101 (2006).

[4.46] R. A. Arif, H. Zhao, and N. Tansu, "Type-II InGaN-GaNAs quantum wells for lasers applications", Appl. Phys. Lett. **92**, 011104 (2008).

[4.47] K. Watanabe, T. Taniguchi, and H. Kanda, "Direct-bandgap properties and evidence for ultraviolet lasing of hexagonal boron nitride single crystal", Nat. Mater. **3**, 404 (2004).

[4.48] K. Watanabe, T. Taniguchi, T. Kuroda, and H. Kanda, "Effects of deformation on band-edge luminescence of hexagonal boron nitride single crystals", Appl.Phys. Lett. **89**, 141902 (2006).

[4.49] K. Watanabe and T. Taniguchi, "Jahn-Teller effect on exciton states in hexagonal boron nitride single crystal", Phys. Rev. B **79**, 193104 (2009).

[4.50] L. Museur, E. Feldbach, and A. Kanaev, "Defect-related photoluminescence of hexagonal boron nitride", Phys. Rev. B **78**, 155204 (2008).

[4.51] D. Kim, I. H. Libon, C. Voelkmann, Y. R. Shen and V. Petrova-Koch, "Multiphoton photoluminescence from GaN with tunable picosecond pulses", Phys. Rev. B **55** 4907 (1997).

[4.52] C. Attaccalite, N. Bockstedte, A. Marini, A. Rubio, and L. Wirtz, "Coupling of excitons and defect states in boron-nitride nanostructures", Phys. Rev. B **83** 144115 (2011).

[5.1] L. Gordon, G. L. Woods, R. C. Eckardt, R. R. Route, R.S. Feigelson, M. M. Fejer and R. Byer, "Diffusion-bonded stacked GaAs for quasiphase-matched second-harmonic generation of a carbon dioxide laser", Eletron. Lett. **29**, 1942 (1993).

[5.2] W. Shi, Y. J. Ding, N. Fernelius and K. Vodopyanov, “Efficient, tunable, and coherent 0.18–5.27-THz source based on GaSe crystal”, Opt. Lett. **27**, 1454 (2002).

[5.3] W. Shi and Y. J. Ding, “Tunable terahertz waves generated by mixing two copropagating infrared beams in GaP”, Opt. Lett. **30**, 1030 (2005).

[5.4] Y. J. Ding, S. J. Lee and J. B. Khurgin, “Transversely pumped counterpropagating optical parametric oscillation and amplification”, Phys. Rev. Lett. **75**, 429 (1995).

[5.5] Y. J. Ding, J. B. Khurgin, and S.-J. Lee, “Transversely-pumped counter-propagating optical parametric oscillators and amplifiers: conversion efficiencies and tuning ranges”, IEEE J. Quantum Electron. **31**, 1648 (1995).

[5.6] G. Beadie, W. S. Rabinovich, and Y. J. Ding, “Transversely pumped nonlinear conversion structure which generates counterpropagating guided waves: theory and numerical modeling”, IEEE J. Quantum Electron. **37**, 863 (2001).

[5.7] L. Lanco, S. Ducci, J.-P. Likforman, X. Marcadet, J. A. W. van Houwelingen, H. Zbinden, G. Leo, and V. Berger, “Semiconductor waveguide source of counterpropagating twin photons”, Phys. Rev. Lett. **97**, 173901 (2006).

[5.8] A. Orieux, X. Caillet, A. Lemaitre, P. Filloux, I. Favero, G. Leo and S. Ducci1, “Efficient parametric generation of counterpropagating two-photon states”, J. Opt. Soc. Am. B, **28**, 45 (2011).

[5.9] X. Caillet, A. Orieux, A. Lemaitre, P. Filloux, I. Favero, G. Leo and S. Ducci, "Two-photon interference with a semiconductor integrated source at room temperature", Opt. Express **18**, 9967 (2010).

[5.10] L. Lanco, S. Ducci, J.-P. Likforman, M. Ravaro, P. Filloux, X. Marcadet, G. Leo and V. Berger, "Backward difference frequency generation in an AlGaAs waveguide", Appl. Phys. Lett. **89**, 031106 (2006).

[5.11] N. A. Sanford, L. H. Robins, A. V. Davydov, A. Shapiro, D. V. Tsvetkov, A. V. Dmitriev, S. Keller, U. K. Mishra, and S. P. DenBaars, "Refractive index study of AlxGa1ÀxN films grown on sapphire substrates", J. Appl. Phys. **94**, 2980 (2003).

[5.12] V. I. Gavrilenko and R. Q. Wu, "Linear and nonlinear optical properties of III-Nitride materials ", Phy. Rev. B **61**, 2632 (2000).

Vita

Guan Sun was born on September 10th, 1986 in Shanghai, China. He received his Bachelor of Science as top 1 student of 35 in major of Materials Physics of Fudan University (Shanghai, China). After he graduated from Fudan University, he joined Lehigh University, Department of Electrical and Computer Engineering on September 2008. During his Ph. D study, his research has been focused photonics and semiconductor optics, especially, terahertz generation and photoluminescence study on GaN based heterostures, Raman scattering on GaN/AlN high electron mobility transistor, novel application of nonlinear generation, etc. To date, he has authored and coauthored more than 30 journal and conference publications. Apart from his academic study, he was also actively involved in student chapters' activities such as SPIE and IEEE Photonics Society. He was the President of IEEE Photonics Society of Lehigh University Student Chapter in 2012.

GUAN SUN

11 Duh Drive Apt 223 · Bethlehem · PA 18015 · (484)767-0758 ·
sunguan.lehigh@gmail.com

Education

- **Lehigh University**, Bethlehem, PA, USA 09. 2008 – 01. 2014

Ph. D Candidate in Electrical Engineering, Department of Electrical and Computer Engineering *Cumulative GPA:* ***3.91/4.0***

- **Fudan University**, Shanghai, China 09. 2004 – 07. 2008

B.S. in Materials Physics, Department of Materials Science

Cumulative GPA: ***3.70/4.0*** *(2nd of 103 students)*

Research Projects

Lehigh University, Bethlehem, PA, USA 09. 2008 – 01.2014

Research Assistant *in Electrical Engineering, Department of Electrical and Computer Engineering (ECE)*

- **Photoluminescence study on III-N bulk materials and nanostructures**

❖ Designed III-Nitrides materials (AlN, GaN, InN, BN) based devices (LED, LD) and nanostructures.
❖ Studied photoluminescence mechanism of aforementioned materials by using various laser systems including Ti: Sapphire Oscillator, Ti: sapphire REGA, Verdi (532 nm), CO_2 laser, OPO *etc.*
❖ Calculated and set up laser source by nonlinear generation process, such as SHG, SFG, DFG, OPA, OPO by commercial available nonlinear crystals, including BBO, KTP, $LiNbO_3$.

- **Raman study on GaN based materials and devices**

❖ Determined hot phonon temperature of GaN high electron mobility transistotr (HEMT) by comparing stokes and anti-stokes intensity of Raman signal.
❖ Tried to reduce hot phonon temperature of by using isotope GaN to fabricate HEMT.
❖ Explored cooling possibility of hot phonon by up-conversion (optical refrigerator).

- **Terahertz generation on InGaN nanostructures, InN bulk and nanomaterials, Gase, GaTe, $LiNbO_3$, Si.**

❖ Prepared InGaN/GaN nanostructures for Terahertz generation, including calculation of band structures, simple mask design (by LayoutEditor) and wire bonding.
❖ Generated Terahertz wave by ultrafast laser (Ti: Sapphire REGA) on InGaN/GaN quantum wells, dots-in-a-wire, InN thin film and quantum dots, GaTe and PP-$LiNbO_3$.
❖ Classified the generation mechanism of InGaN nanostructures and demonstrated its high efficiency.

- **Backward and phase-conjugated nonlinear generation on PP-KTP/RTP**

❖ Achieved enhanced nonlinear generation by using periodic waveguides.
❖ Observed backward second harmonic generation from ultrashort PP-KTP
❖ Explored phase-conjugated backward generation on PP-KTP.

- **Other Projects**

❖ Simulated and designed optical devices, nanostructures and metamaterials by using FDTD, BeamPrp *etc*.
❖ Measured transmission and reflection of semiconductor thin film by FTIR, explained results by calculation.
❖ Up-conversion using PP-$LiNbO_3$ waveguide for CO_2 detection.
❖ Designed optic parametric down-conversion in transverse geometry based GaN/AlGaN waveguide.

Awards & Honors

- Lehigh University Research Assistantship, Lehigh University (2008 – present)
- Sherman Fairchild Fellowship (for outstanding students in solid state area), Lehigh University (2011, 2012)
- Department Fellowship, Department of ECE (for outstanding students in university), Lehigh University (2008)
- National Scholarship, 1st class (for outstanding students in university) , Fudan University (2007)
- People's Scholarship, 1st class (for top1 student in department), Fudan University (2004, 2005)
- Toshiba Scholarship (for outstanding students in semiconductor area), Fudan University (2006)

Professional Affiliations

- Chair, Student Society of IEEE Photonics in Lehigh University 2011 – 2012
- Member, Institute of Electrical and Electronics Engineers (IEEE) 2008 – present
- Member, IEEE Photonics Society 2008 – present

Journal Reviewer

- Applied Physics Letter
- IEEE Journal of Selected Topics in Quantum Electronics
- Applied Optics
- Optical and Quantum Electronics
- Micro and Nano Letter

Referred Journal Pulications

1. **G. Sun**, R. Chen, Y. J. Ding, H. Nguyen, and Z. Mi, "InGaN/GaN Dot-in-a-Wire: Ultimate Terahertz Nanoemitters", submitted.
2. **G. Sun,** R. Chen, Y. J. Ding, and J. B. Khurgin, "Potential for Laser Refrigeration via Optical-phonon-assisted Anti-Stokes Photoluminescence in Bulk GaN", submitted.
3. **G. Sun**, R. Chen, Y. J. Ding, H. Zhao, G. Liu, J. Zhang, and N. Tansu, "Strikingly Different Behaviors of Photoluminescence and Terahertz Generation in InGaN/GaN Quantum Wells", *IEEE J. Selected Topics in Quantum Electronics.*, **19** 8400106 (2013).
4. **G. Sun**, G. Xu, Y. J. Ding, H. Zhao, G. Liu, J. Zhang, and N. Tansu, "Investigation of Fast and Slow Decays in InGaN/GaN Quantum Wells", *Appl. Phys. Lett.*, **99** 081104 (2011).
5. **G. Sun**, G. Xu, Y. J. Ding, H. Zhao, G. Liu, J. Zhang and N. Tansu, "Efficient Terahertz Generation from Multiple InGaN/GaN Quantum Wells", *IEEE J. Selected Topics in Quantum Electronics*., **17** 48 (2011).
6. **G. Sun**, Y. J. Ding, G. Y. Liu, G. S. Huang, H. Zhao, N. Tansu, and J. B. Khurgin, "Photoluminescence Emission in Deep Ultraviolet Region from GaN/AlN Asymmetric-Coupled Quantum Wells", *Appl. Phys. Lett.*, **97** 021904 (2010).
7. G. Chen, **G. Sun**, Y. J. Ding, P. Prete, I. Miccoli, N. Lovergine, H. Shtrikman, P. Kung, T. Livneh and J. E. Spanier, "Direct Measurement of Band Edge Discontinuity in Individual Core-Shell Nanowires by Photocurrent Spectroscopy", *Nano Lett*., **13** 4152 (2013).
8. G. Xu, **G. Sun**, Y. J. Ding, H. Zhao, G. Liu, J. Zhang, and N. Tansu, "Investigation of large Stark shifts in InGaN/GaN multiple quantum wells", *J. Appl. Phys.,* **113** 033104 (2013).

9. R. Chen, **G. Sun**, G. Xu. Y. J. Ding, I. B. Zotova, "Generation of high-frequency terahertz waves in periodically poled $LiNbO_3$ based on backward parametric interaction", *Appl. Phys. Lett.,* **101** 111101 (2012).
10. G. Xu, **G. Sun**, Y. J. Ding, I. B. Zotova, M. Jamil, I. T. Ferguson, "Mechanism for THz generation from InN micropyramid emitters", *J. Appl. Phys.,* **109** 093111 (2011).
11. G. Xu, **G. Sun**, Y. J. Ding, I.B. Zotova, K.C. Mandal, A. Mertiri, G. Pabst, N. Fernelius, "Investigation of symmetries of second-order nonlinear susceptibility tensor of GaSe crystals in THz domain", *Opt. Commun.*, **284** 2027 (2011).
12. G. Xu, **G. Sun**, Y. J. Ding, I. B. Zotova, K. C. Mandal, A. Mertiri, G. Pabst, R. Roy, and N. C. Fernelius, "Investigation of Terahertz Generation due to Unidirectional Diffusion of Carriers in Centrosymmetric GaTe Crystals", *IEEE J. Selected Topics in Quantum Electronics.*, **17** 30 (2011).

Conference Publications/Proceedings

1. **G. Sun**, R. Chen, Y. J. Ding, **Invite Talk**, IPC, MH1.2 (2013).
2. **G. Sun**, R. Chen, P. Zhao, Y. J. Ding, H. Nguyen, and Z. Mi, CLEO, JTh2A. 57 (2013).
3. **G. Sun**, R. Chen, Y. J. Ding, H. Zhao, G. Liu, J. Zhang and N. Tansu, CLEO, JW2A. 50 (2013).
4. **G. Sun**, R. Chen, and Y. J. Ding, CLEO, QTu1E. 2 (2013).
5. **G. Sun**, R. Chen, P. Zhao, Y. J. Ding, H. Nguyen, and Z. Mi, CLEO, CM2L.2 (2012).
6. **G. Sun**, R. Chen, Y. J. Ding, H. Zhao, G. Liu, J. Zhang, and N. Tansu, CLEO, CTu2J.3 (2012).
7. **G. Sun**, G. Xu, Y. J. Ding, H. Zhao, G. Liu, J. Zhang, N. Tansu, CLEO, CMM.4 (2011).
8. **G. Sun**, Y. J. Ding, CLEO, JThB.54 (2011).
9. **G. Sun**, S. K. Tripathy, Y. Ding, G. Liu, G. S. Huang, H. Zhao, N. Tansu, and J. B. Khurgin, CLEO, CThL.6 (2010).
10. **G. Sun**, S. K. Tripathy, Y. Ding, G. Liu, H. Zhao, G. S. Huang, N. Tansu, and J. B. Khurgin, CLEO, QThC.2 (2010).
11. **G. Sun**, S. K. Tripathy, Y. J. Ding, G. Liu, G. S. Huang, H. Zhao, N. Tansu, and J. B. Khurgin, CLEO, CTuF.6 (2009).
12. R. Chen, G. Xu, **G. Sun** and Y. J. Ding, CLEO, QF2D. 6 (2013).
13. D. Li, **G. Sun**, Y. J. Ding and N. S. Prasad, CLEO, CM4D.2 (2013).
14. G. Chen, **G. Sun**, Y. J. Ding, I. Miccoli, N. Lovergine, H. Shtrikman, P. Kung, and J. E. Spanier, APS March, Y6. 003 (2013).
15. Y. J. Ding, **G. Sun**, R. Chen, G. Xu, I. Zotova, CLEO, CTu1B.4 (2012).

16. Z. Li, **G. Sun**, P. Zhao, Y. J. Ding, Q. Gan, CLEO, CTh1D.2 (2012).
17. G. Xu, **G. Sun**, Y. J. Ding H. Zhao, G. Liu, J. Zhang, N. Tansu, CLEO, JWA70 (2011).
18. G. Xu, **G. Sun**, Y. J. Ding, I. B. Zotova, K. C. Mandal, A. Mertiri, G. Pabst and N. C. Fernelius, CLEO, CMJJ1 (2010).
19. G. Xu, **G. Sun**, Y. J. Ding, I. B. Zotova, M. Jamil, I. T. Ferguson, CLEO, CMJJ3 (2010).
20. G. Xu, **G. Sun**, Y. J. Ding, I. B. Zotova, K. C. Mandal, A. Mertiri, G. Pabst and N. C. Fernelius, CLEO, QFG2, (2010).